10-7-2019 10:00 AM

Analysis of Roofs of Wooden Houses Under Uplift Wind loads- Analytical Solution, Retrofit, and Reliability Analysis

Adnan Farouk Enajar, *The University of Western Ontario*

Supervisor: El Damatty, Ashraf, *The University of Western Ontario*
A thesis submitted in partial fulfillment of the requirements for the Doctor of Philosophy degree
in Civil and Environmental Engineering
© Adnan Farouk Enajar 2019

Recommended Citation

Abstract

Observations of post-hurricane events indicate that light-frame wood houses are vulnerable to failure due to the inability of their connections to provide sufficient transfer of uplift wind loads from the roof of the house to the foundation. One of these connections is the roof-to-wall connection (RTWC), which connects roof trusses to the top plate members of the walls. This issue has been investigated through full-scale testing at the Insurance Research Lab for Better Homes. This thesis describes the detailed finite element modelling performed for this full-scale testing and provides a comparison of the numerical predictions with the experimental results. The comparison revealed the ability of the sophisticated finite element modelling to predict the nonlinear response of the roof under uplift wind loads that vary both in time and space. A semi-analytical solution for analyzing the full-scale test is also introduced. With the use of statically indeterminate slope deflection equations that include shear deformation, the new model simulates an entire roof truss as a beam on an elastic foundation. The solution model was validated first against a finite element model with respect to the RTWC reactions and then by comparison with the experimental results. A further component of the study was an evaluation of the reliability of the roof system using Monte Carlo simulations and appropriate probabilistic models. Beta and normal distributions were designed for generating both RTWC stiffness values and uplift wind loads, respectively. It was found that beyond a mean wind velocity of 30 m/sec, the probability of roof failure increases rapidly. The study proceeds by considering a previously prepared external retrofitting that can reduce possible toe-nail failure and create an additional load path. For use only in the case of warnings of highly intense winds, the external retrofitting consists of bearing cables, external cables, and rigid bars. A small-scale house was previously tested at the Wind Engineering, Energy and Environment Research Institute (WindEEE) facility in order to assess the performance of the retrofitting system. In the current study, the semi-analytical solution model was extended to analyze the retrofitting system. The results reveal that the retrofitting system increases the possible wind velocity threshold prior to failure by 36.4%.

KEYWORDS:

Finite element analysis, semi-analytical solution model, roof-to-wall connections, Monte Carlo simulations, retrofitting system.

Summary for Lay Audience

Observations of post-hurricane events indicate that light-frame wood houses are vulnerable to failure due to the inability of their connections to provide sufficient transfer of uplift wind loads from the roof of the house to the foundation. One of these connections is the roof-to-wall connection (RTWC), which connects roof trusses to the top plate members of the walls. This thesis describes a detailed analysis of this problem. A simplified solution for analyzing this problem is also introduced. A further component of the study was evaluating the probability of failure for these connections using Monte Carlo simulations. It was found that beyond a mean wind velocity of 30 m/sec, the probability of roof failure increases rapidly. The study proceeds by considering a previously prepared external retrofitting that can reduce possible connections failure and create an additional load path. For use only in the case of warnings of highly intense winds, the external retrofitting consists of bearing cables, external cables, and rigid bars. The bearing cables are installed on the roof and attached to rigid bars in the roof edge, which are, in turn, connected to external cables supported by micropiles permanently embedded in the ground. The retrofit system would be designed so that the cables could be kept folded during normal wind conditions, thus avoiding distortion of the style and aesthetics of the house. The installation of the retrofit system would take place when advance hurricane warnings are issued. In the current study, the simplified model was extended to analyze the retrofitting system. The results reveal that the retrofitting system increases the possible wind velocity threshold prior to failure by 36.4%.

Co-Authorship Statement

This thesis has been prepared in accordance to the regulations for an Integrated Article layout thesis designated by the School of Graduate and Postdoctoral Studies at the University of Western Ontario. Statements regarding the co-authorship of individual chapters are as follows:

Chapter 2 - Nonlinear Modelling of Roof-to-Wall Connections in a Gable Roof Structure under Uplift Wind Loads

The initial numerical model was developed by R. Jacklin. Modifications to the numerical model and the numerical analysis were completed by A. Enajar under the supervision of Dr. A. A. El Damatty. A paper co-authored by A. Enajar, R. Jacklin and A. A. El Damatty published in the Journal of Wind and Structures, Vol. 28, No. 3 (2019) 181-190.

Chapter 3 - Semi-Analytical Solution for a Light-Frame Wood Structure under Uplift Wind Loads

All the numerical work was conducted by A. Enajar under supervision of Dr. A. A. El Damatty. Drafts of Chapter 3 were written by A. Enajar and modifications were done under supervision of Dr. A. A. El Damatty. This chapter will be submitted to Journal of Engineering Structures.

Chapter 4 - Reliability of Roof-to-Wall Connections in a Gable Roof Structure under Uplift Wind Loads

The numerical work was conducted by A. Enajar under supervision of Dr. A. A. El Damatty and Dr. A. Nassef. Drafts of Chapter 4 were written by A. Enajar and modifications were done under supervision of Dr. A. A. El Damatty. This chapter will be submitted to Journal of Engineering Structures.

Chapter 5 - Nonlinear Modelling of a Retrofitted Light-Frame Wood Structure

The experimental testing at WindEEE was completed by J. Rosenkrantz, and A. Enajar under supervision of Dr. A. A. El Damatty. Drafts of Chapter 4 were written by A. Enajar and modifications were done under supervision of Dr. A. A. El Damatty. This chapter will be submitted to Journal of Engineering Structures.

Acknowledgments

Table of Contents

List of Tables

List of Figures

List of Appendices

List of Abbreviations

FEM   Finite element modelling

FEMA   Federal emergency management agency

IRLBH   Insurance research lab for better homes

NBCC   National building code of Canada

RTWC   Roof-to-wall connection

STTC   Sheathing-to-truss connection

TAM   Tributary area method

UWO   University of Western Ontario

WDM   Wood design manual

WindEEE   Wind engineering, energy and environment

WTFC   Wall-to-foundation connection

WOW   Wall of wind

List of Symbols

A_S	Shear area
E	Modulus of elasticity
$[F_{\theta 1}],[F_{\theta 2}]$	Coefficients matrices of angular rotations
$[F_{r1}],[F_{r2}]$	Coefficients matrices of spring reactions
G	Shear modulus
I	Moment of inertia
$k_{elastic}$	Elastic stiffness matrix
$k_{geometric}$	Geometric stiffness matrix
$L_{1,2}$	Horizontal distance between truss 1 and truss 2
M_s	Moment at the south overhang
M_n	Moment at the north overhang
$\{Mf_1\},\{Mf_2\}$	Fixed end moment vectors
$Mf_{1,2}$	Fixed end moment between truss 1 and truss 2
$N_{n,p}$	B-spline basis function with curve degree p and control point n
R_T	Tributary area load applied to each truss
x_m	Measured deflection data
y_m	Measured force data
ϕ	Shearing deformation factor
θ	Angular rotation
Δ	Relative settlement between supports
ω	Random variables generated between a range of 0 to 1 from standard beta distributions

Chapter 1

1   Introduction

1.1   General

Light-frame wood houses constitute the majority of North American residences, representing up to 90% of dwellings in the United States alone (Dao et al., 2012). The percentage of wood houses is that large because, compared with other materials, wood is considered a renewable and environmentally friendly resource. It is also deemed to be durable if appropriate maintenance is performed during the lifespan of the structure. With respect to cost, wood construction offers an effective, economical solution because it is less expensive than either steel or concrete. Wood is an anisotropic material, which means that its mechanical properties differ directionally. The mechanical strength of wood members is dependent on a number of parameters, such as the specific gravity, the type of wood, the direction of the grain, and the water content.

On the downside, light-frame wood houses are more susceptible to damage caused by extreme weather conditions such as wind loads. A wind load can involve four distinct forces that affect such houses: uplifting, racking, sliding, and overturning (Taraschuk, 2011). A major effect of a wind load on the roofs of light-frame wood houses is uplift pressure (i.e., suction pressure). This type of pressure can damage wooden roofs due to a deficiency in the load path that prevents this suction pressure from being transferred to the ground. Keith and Rose (1994) investigated the failure of residential houses in Florida following Hurricane Andrew. They concluded that the failure of light-frame wood houses was due to the inability of the wood connections to sustain the applied uplift forces. They also observed that failure occurred more often at the ends and corners of gable roofs due to the high uplift wind force generated at those locations.

Light-frame wood houses are characterized by their ability to carry gravity loads during the lifespan of the structure. As mentioned above, their poor performance during severe wind storms indicates weakness with respect to their ability to resist uplift wind loads exerted on their roofs. This failure has been observed at two critical connections in the

roof system: sheathing-to-truss connections (STTCs) and roof-to-wall connections (RTWCs) (Jacklin et al., 2014). Prior to Hurricane Andrew in Florida, RTWCs were toe-nailed (Datin et al., 2010). The withdrawal capacity of toe-nail connections enables them to withstand suction pressure. This capacity varies for each connection according to the type of nails used as shown in Figure 1.1, such as common, box, or sinker nails (NDS, 2015). Current new RTWC versions, such as metal straps, provide higher levels of withdrawal capacity than traditional toe-nailing (Reed et al., 1997). Figures 1.2 and 1.3 show examples of roof damage due to STTC and RTWC failure, respectively.

The significance of the research presented in this thesis is that it offers a valuable solution for utilizing retrofit systems in existing light-frame wood houses located in hurricane regions. In such regions, most existing light-frame wood houses are at risk of damage, especially houses in which toe-nails were employed as RTWCs. For this reason, a number of retrofit techniques have been developed with the goal of increasing RTWC capacity. These techniques are implemented either internally, through the replacement of the toe-nails with metal straps, or externally, with the houses being supported by cables anchored to the foundation.
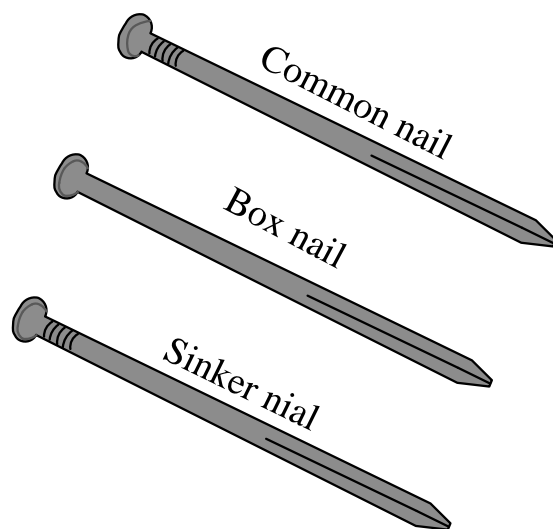
Figure 1.1: Common, box, and sinker nails.

Figure 1.2: Failure of roof sheathing near the end gable truss.

Source: www.floridadisaster.org/ hrg/content/risks/risks_index.asp

Figure 1.3: Failure of roof truss connections.

Source: www.apawood.org/wind-weather-seismic.

1.2   Background

Previous research focussed on examining the behaviour of light-frame wood houses based on evaluations of RTWC performance, which was assessed experimentally by testing individual or multiple connections under simulated uplift wind loads. Rosowsky et al., (1998), for example, used the ASTM D 1761 test procedure to conduct tests on a

variety of types of RTWCs, such as toe-nails and metal straps. Their experimental program included two testing configurations: individual connections and connections in a series. To account for load sharing among connections, the second set of configuration tests was conducted using a segment of a roof structure that contained seven connections, including roof sheathing, wall sheathing with studs, rafters, and top plates. Based on the results for the toe-nail connections, the authors concluded that, due to the load sharing, the average uplift capacity of the connections in the roof segment was about 50 % greater than the average capacity of any individual connection. This finding was attributed to the wide variability inherent in toe-nail connections compared with metal strap connections.

Reed et al., (1997) conducted experimental testing under static loads to the point of failure with respect to multiple types of connections between a rafter and a top plate. The connections included toe-nails, metal straps, epoxy coating, and the addition of an extra piece of wood glued with epoxy. To simulate the as-built shape, the rafter of the testing specimen was aligned to have a 1:4 slope. The experiment was divided into two parts: testing of individual connections and of a system of connections in a segment of the roof structure. The results of the study demonstrated that, due to the load sharing among the connections, the system of connections in the roof segment provided better withdrawal capacity than those tested individually, especially the toe-nail version. Less variation was evident in the results for the metal straps, however, because, when tested individually, their coefficient of variation is lower than that of toe-nails. Cheng (2004) conducted another study in order to evaluate the uplift capacity of toe-nailed RTWCs with respect to ASTM D 1761 limitations. Their study entailed the application of a monotonic load to a variety of RTWC configurations. The tests were conducted on a total of 300 samples using different types of wood, such as spruce-pine-fir (SPF), Douglas fir (DF), and southern pine (SP), with 3-8D and 2-16D common or box nails. In this experiment, the specific gravity and the water content were measured in order to provide controlled results based on ASTM D 1761. The researchers concluded that toe-nail connections are unsuitable for house roofs subjected to severe hurricanes.

Shanmugam et al., (2009) tested 25 specimens in order to evaluate the load-deflection curves of 2-16D and 3-16D toe-nail connections. To include consideration of the load

sharing between adjacent connections, each specimen consisted of four connections. A cyclic load was applied to the specimens up to the point of failure. It was concluded that most connections failed in withdrawal mode; however, some exhibited failure as a splitting of the wood fibres in the bottom rafter. Based on the data observed for 100 connections, a trilinear statistical probabilistic RTWC model was designed based on a combination of normal, lognormal, and Weibull distributions. Morrison and Kopp (2011) compared the uplift capacity of toe-nailed RTWCs (3-12D shank nails) under ramp load and realistic wind load generated from the pressure in airbags connected to the RTWCs. The results showed that the withdrawal capacities of the connections were similar for both ramp and realistic load. With ramp load, the failure mode was observed as a constant incremental withdrawal until failure while the failure mode under realistic wind load was dependent on the peaks in the applied load-time trace.

Other research has involved evaluating RTWC performance through the construction of full-scale or small-scale light-frame wood houses under simulated wind loads. These scale models were utilized to extract details about the load sharing between the connections and the vertical load paths (Henderson et al., 2013; Datin and Prevatt, 2013). Other researchers have monitored the wind responses of existing houses over time (Doudak et al., 2005). Based on previously published studies, wind loads were simulated by applying pressure boxes on the roofs of the houses in order to replicate random wind responses (Kopp et al., 2010; Henderson et al., 2013).

Henderson et al., (2013) conducted a full-scale experiment on hip roof house with the goal of determining the load sharing among the RTWCs (5-12D shank nails). To simulate the spatial and temporal uplift wind pressure, 58 pressure boxes were installed on the roof. Load cells and displacement transducers were used for measuring the reaction and displacement at the RTWC, respectively. Influence coefficients for each RTWC were calculated based both on the application of each pressure box alone and on the application of all 58 pressure boxes at the same time. A significant change in the influence functions was found when permanent withdrawal occurred at the RTWCs. Datin et al., (2010) evaluated the influence coefficients experimentally for a small-scale house by applying concentrated uplift loads on point grids at the sheathings in order to

measure the reactions of the load cells located at 11 RTWCs and at 9 WTFCs. It was found that the influence of the loading could also be observed one or two trusses away from the loaded truss.

Other researchers have employed finite element modelling or simplified modelling for assessing RTWCs numerically. Finite element modelling is a sophisticated numerical tool that can be used for modelling two-dimensional wood connections or three-dimensional light-frame wood houses. Foschi (2000), for example, established a finite element technique for modelling a nail connection according to the elastoplastic behaviour of the nail in combination with the nonlinear wood medium. Foschi's (2000) element was then utilized for 3D light-frame structures (He et al., 2001). Thampi et al., (2011) implemented 3D finite element modelling of a light-frame wood house that had been damaged by a tornado. They used ANSYS commercial software for their analysis, evaluating the pressure based on the scaled model. The damage predicted by the finite element model agreed well with that observed in the affected house.

Shivarudrappa and Nielson (2013) employed the finite element package in ANSYS commercial software in order to conduct a sensitivity analysis of a gable roof house under gravity and uplift loads. The parameters of their sensitivity analysis were based on the thickness of the sheathing and on a variety of stiffness values for both RTWCs and STTCs. Influence coefficient contours were plotted for each RTWC in order to examine the load path in the gable roof house. The authors also defined the influence coefficient at a specific position as the reaction of the RTWC when the unit load was applied at that position. Their study revealed that the load distribution was affected by the stiffness of the connections, with a higher stiffness connection observed for greater loads.

Dessouki (2010) and Jacklin (2013) performed numerical finite element analysis using SAP2000 commercial software for experimental testing previously conducted at the Insurance Research Lab for Better Homes (IRLBH), located at the University of Western Ontario (Morrison et al., 2012). In Dessouki's (2010) numerical model, the frame element was used for modelling the truss members and stud walls, while the shell element was used for modelling the plywood sheathings. Dessouki (2010) concluded that

good agreement was achieved between the numerical prediction and the experimental results with respect to deflection at the RTWCs, with a maximum difference of 20 %. Jacklin (2013) employed a similar numerical model but without modelling the walls; however, these researchers each proposed a different retrofitting system for overcoming the weakness of the toe-nail connections. Dessouki (2010) suggested a system of two-dimensional steel wire net installed on the top of the house and anchored to carbon fibre rods on four sides. The carbon fibre rods were connected to a number of external pretension cables, which were anchored to the foundation. Jacklin (2013) proposed a simple retrofitting system consisting of bearing cables installed on the roof of the house and anchored to rigid aluminum side bars. The function of the rigid bars was to create a uniform load at the bearing cables and to reduce the number of external cables that were connected between the bars and the foundation.

Guha and Kopp (2014) implemented a simplified numerical model based on analytical slope deflection equations in order to evaluate the responses of a series of toe-nail RTWCs. The experimental testing conducted by Khan (2012) was used for validating the simplified model performed by Guha and Kopp (2014). In Khan's (2012) experiment, seven RTWCs were connected between plate members in the bottom and two steel beams in the top. To evaluate the effect of wind duration on RTWC failure, a Monte Carlo simulation was employed in conjunction with a simplified model and random connection stiffness values. It was concluded that the probability of RTWC failure was elevated by up to 15 % if the wind duration increased from 1 h to 5 h due to increasing the damaging peaks (Guha and Kopp, 2014).

1.3   Objectives

Previous studies indicated that RTWCs, especially toe-nail connections, are insufficient with respect to transferring tension forces from the roofs to the walls of houses. The stiffness of these connections also varies depending on the nature of the wood material. The objectives of this research can be summarized as follows:

1. Develop and run linear and nonlinear simplified solution models for predicting RTWC responses in gable roof houses.

2. Validate the output of the simplified solution model against that of the nonlinear finite element model and against the experimental test results.

3. Assess the reliability of roof trusses subjected to uplift wind load using the simplified solution model in order to evaluate the probability of RTWC failure relative to wind speed.

4. Extend the simplified solution model to include an external retrofitting system in order to validate the solution produced by the model against the experimental test results.

1.4   Scope of the Thesis

This thesis has been prepared in an integrated-article format. The current chapter presents general background and the main research objectives related to the failure of roof connections in houses, along with possible mitigation strategies. The four subsequent chapters address these objectives in detail. The last chapter provides an overall conclusion for the thesis and suggests corresponding possible future work. The scope of the four chapters following this one is summarized below.

1.4.1   Chapter 2 - Nonlinear Modelling of Roof-to-Wall Connections in a Gable Roof Structure under Uplift Wind Loads

This chapter introduces the use of previously prepared nonlinear finite element modelling using SAP2000 commercial software in order to simulate a gable roof house. This numerical model was validated against the experimental testing conducted on a gable roof house at the Insurance Research Lab for Better Homes for a range of wind speeds. The testing was associated with the occurrence of permanent withdrawal at the RTWCs. The numerical model provided values representing load sharing among the trusses for the pressures associated with maximum global uplift loads for a variety of wind speeds. A comparison of the realistic pressure and the code pressure was also included in the calculation of the load sharing among the trusses. The chapter presents an additional comparison of the load sharing calculations produced by finite element modelling and those obtained using the tributary area method.

1.4.2 Chapter 3 – Semi-Analytical Solution for a Light-Frame Wood Structure under Uplift Wind Loads

This chapter describes the development and analysis of a semi-analytical solution model based on the assumption that the entire roof can be modelled as a beam with an elastic foundation. The cross section of the beam is represented by the cross members between the trusses, the fascia, and the sheathing, all lumped together, assuming that the spacing between the trusses is small compared with the depth of the truss. Each individual truss is treated as a supporting spring with its stiffness being evaluated according to the ratio of the unit load to the deflection of the top truss. A comparison of the results obtained from this solution model with those produced by finite element modelling and with the experimental results is also included. The basis of the comparison was an examination of both the RTWC responses and the load sharing among the trusses.

1.4.3 Chapter 4 - Reliability of Roof-to-Wall Connections in a Gable Roof Structure under Uplift Wind Loads

This chapter is focussed on the use of Monte Carlo simulations for estimating the probability of toe-nail failure as a function of wind speed. In each simulation, 10,000 scenarios were implemented in a simplified model of a full-scale house. Each scenario was analyzed randomly with a different load-deflection curve for each RTWC and random uplift wind loads. Based on these scenarios, a range of wind speeds leading to failure was obtained. At each wind speed in the range, other simulations were conducted in order to evaluate the probability of roof failure.

1.4.4 Chapter 5 - Nonlinear Modelling of a Retrofitted Light-Frame Wood Structure

This chapter employs the previous retrofitting technique proposed by Jacklin (2013) for mitigating house roof failure through the installation of external rooftop cables that are anchored to the foundation. The chapter also explains the extension of the simplified model presented in Chapter 3 to include the new retrofitting system. The extended model was then applied to enable a comparison of the results of experiments conducted on a

small-scale house at WindEEE and the findings from tests conducted on a roof segment at the structural laboratory at University of Western Ontario.

1.5   The contributions

This thesis focuses on the uplift response of existing houses located in the hurricane-prone areas. In these houses, the old weak toe-nail detailing is used to connect the roof to walls. The main contributions of this thesis are:

1. The development and validation using finite element analysis and experimental results of computational efficient semi-analytical model that can predict the nonlinear behaviour of roof houses under uplift wind load.
2. The extension of this semi-analytical solution to model the behaviour of houses with a previously developed retrofit system.
3. The use of the semi-analytical model to conduct reliability analysis of gable roofs under uplift pressure taking into account the randomness of the stiffness of each RTWC and the randomness of wind load.

1.6   References

Cheng, J. (2004), "Testing and analysis of the toe-nailed connection in the residential roof-to-wall system", *Forest Products Journal*, **54**(4), 58-65.

Dao, T. N., van de Lindt, John W, Prevatt, D. O., and Gupta, R. (2012), "Probabilistic procedure for wood-frame roof sheathing panel debris impact to windows in hurricanes", *Engineering Structures*, **35**,178-187.

Datin, P. L., Mensah, A. F. and Prevatt, D. O. (2010), "Experimentally Determined Structural Load Paths in a 1/3-Scale Model of Light-Framed Wood, Rectangular Building", *2010 ASCE Structures Congress*, Orlando, Florida, United States, May.

Datin, P. L., and Prevatt, D. O. (2013), "Using instrumented small-scale models to study structural load paths in wood-framed buildings", *Engineering Structures*, **54**, 47-56.

Dessouki, A. A. (2010), "Analysis and retrofitting of low rise houses under wind loading", Master Thesis, University of Western Ontario, London, ON, Canada.

Doudak, G., McClure, G., Smith, I., Hu, L., and Stathopoulos, T. (2005), "Monitoring structural response of a wooden light-frame industrial shed building to environmental loads", *Journal of Structural Engineering*, **131**(5), 794-805.

Foschi, R. O., (2000), "Modeling the Hysteretic Response of Mechanical Connections for Wood Structures", 6th World Conf. on Timber Engineering, Whistler, Canada, July.

Guha, T.K. and Kopp, G.A. (2014), "Storm duration effects on roof-to-wall-connection failures of a residential, wood-frame, gable roof", *Journal of Wind Engineering and Industrial Aerodynamics*, **133**, 101-109.

Henderson, D. J., Morrison, M. J., and Kopp, G. A. (2013), "Response of toe-nailed, roof-to-wall connections to extreme wind loads in a full-scale, timber-framed, hip roof", *Engineering Structures*, **56**, 1474-1483.

He, M., Lam, F., and Foschi, R. O., (2001), "Modeling three-dimensional timber light-frame buildings", *Journal of Structural Engineering*, **127**(8), 901-913.

Jacklin, R. B. (2013), "Numerical and experimental analysis of retrofit system for light-framed wood structures under wind loading", Master Thesis, University of Western Ontario, London, ON, Canada.

Jacklin, R.B., El Damatty, A.A. and Dessouki, A.A. (2014), "Finite-element modeling of a light-framed wood roof structure", *Wind and Structures*, **19**(6), 603-621.

Keith, E. L., and Rose, J. D. (1994), "Hurricane Andrew-structural performance of buildings in south Florida", *Journal of Performance of Constructed Facilities*, **8**(3), 178-191.

Khan, MAA. (2012), "Load-sharing of toe-nailed roof-to-wall connections under extreme wind loads in wood-frame houses", Master Thesis, University of Western Ontario, London, ON, Canada.

Kopp, G. A., Morrison, M. J., Gavanski, E., Henderson, D. J., and Hong, H. P. (2010). "'Three little pigs' project: hurricane risk mitigation by integrated wind tunnel and full-scale laboratory tests", *Natural Hazards Review*, **11**(4), 151-161.

Morrison, M. J., and Kopp, G. A. (2011), "Performance of toe-nail connections under realistic wind loading", *Engineering Structures*, **33**(1), 69-76.

Morrison, M. J., Henderson, D. J. and Kopp, G. A. (2012), "The response of a wood-frame, gable roof to fluctuating wind loads", *Engineering Structures*, **41**, 498-509.

NDS (2015), *National Design Specification for Wood Construction*, American Wood Council, Leesburg, Virginia, USA.

Reed, T. D., Rosowsky, D. V. and Schiff, S. D. (1997), "Uplift capacity of light-frame rafter to top plate connections", *Journal of Architectural Engineering*, **3**(4), 156-163.

Rosowsky, D., Reed, T., and Tyner, K. (1998), "Establishing uplift design values for metal connectors in light-frame construction", *Journal of Testing Evaluation*, **26**(5), 426-433.

Shanmugam, B., Nielson, B. G., and Prevatt, D. O. (2009), "Statistical and analytical models for roof components in existing light-framed wood structures", *Engineering Structures*, **31**(11), 2607-2616.

Shivarudrappa, R. and Nielson, B. G. (2013), "Sensitivity of load distribution in light-framed wood roof systems due to typical modeling parameters", *Journal of Performance of Constructed Facilities*, **27**(3), 222-234.

Taraschuk, C. (2011), "Lateral Load Resistance–NBC Part 9", NRC Canadian Codes Centre.

Thampi, H., Dayal, V. and Sarkar, P. P. (2011), "Finite element analysis of interaction of tornados with a low-rise timber building", *Journal of Wind Engineering and Industrial Aerodynamics*, **99**(4), 369-377.

Chapter 2

2 Nonlinear Modelling of Roof-to-Wall Connections in a Gable-Roof Structure under Uplift Wind Loads*

2.1 Introduction

Since wood is a renewable and environmentally friendly resource, the majority of North American residences are wood structures. Severe hurricanes have seriously damaged a number of these wood houses. The Federal Emergency Management Agency (FEMA) has presented assessment reports of building performance under a series of hurricanes, such as Hurricane Andrew in 1992 and Hurricane Sandy in 2013. One of their findings is that the damage to light-frame wood structures observed in Florida following Hurricane Andrew was caused primarily by suction pressure on the roofs (FEMA 1992). Suction pressure causes damage to wood structures due to the inability of the wood connections to transfer this type of force to the ground (Morrison et al., 2014, Van de Lindt et al., 2007, Prevatt et al., 2012). Two critical connections have been observed in roof trusses: sheathing-to-truss connections (STTCs) and roof-to-wall connections (RTWCs) (Jacklin et al., 2014).

The withdrawal capacity of wood connections is dependent on the penetration depth of the nails and on the individual properties of the wood that forms the connections, such as water content and specific gravity (Luszczki et al., 2013). As a result, some connections are characterized by a higher degree of stiffness than others, and a stiffer connection can absorb a greater load.

When a weak connection fails, the extra load is transferred to the adjacent connections, placing increased demands on the connections that have not yet failed (Guha and Kopp 2014). The consequence of any increases in the applied uplift load is that the remaining connections become unable to sustain that uplift load, resulting in additional connection failures.

---

*Part of this chapter published in Wind and Structures, Vol. 28, No. 3 (2019) 181-190.

The work presented in this chapter was based on the use of the finite element model created by Jacklin (2013) for predicting the results of testing conducted at the Insurance Research Lab for Better Homes (IRLBH) located at the University of Western Ontario (Morrison et al., 2012). Because of the reasonable predictions it provides, finite element analysis is considered as an alternative tool for modelling light-frame wood houses subjected to wind loads. Kasal et al., (2004) studied the distribution of a lateral load on the walls of light-frame wood houses. Eight avenues of investigation were discussed in their study, including the tributary area, the total shear, the relative stiffness, and three-dimensional finite element modelling (FEM). Those methods were then applied for a determination of the lateral load sharing for each wall of a full-scale L-shaped experimental test house, with FEM producing the most accurate results. Thampi et al., (2011) used ANSYS commercial software to create a three-dimensional finite element model for evaluating tornado damage to a light-frame wood house located in Parkersburg, USA. The damage predicted by their model agreed well with that observed in the affected house. Shivarudrappa and Nielson (2013) investigated the load paths in light-frame wood structures under a wind uplift load by plotting the influence coefficient contours for each RTWC. For their study which was targeted at determining how the loads transferred vertically, they used ANSYS commercial software to develop a finite element model based on the experimental testing conducted by Datin et al., (2010). Zisis and Stathopoulos (2012) conducted three-dimensional finite element model using SAP2000 commercial software under real wind pressure evaluated by monitoring as-built gable-roof house. This model was validated against the load cells at foundation level, and they found experimentally, that the foundation reaction was lower by 17 % to 28 % than predicted by the model. Satheeskumar et al., (2017) evaluated numerically the effect of roof-cladding and roof-ceiling on the reaction of RTWCs by using FEM. In their model, they used ABAQUS commercial software based on the experimental testing performed by Satheeskumar et al., (2016). It was concluded that there was a 25 % reduction in the RTWCs uplift reactions by presence of these roof elements. From another perspective, Foschi (2000) established nail-connection element based on the elasto-plastic behavior of the nail combined with nonlinear wood medium. This nail-connection element was

implemented in finite element models of various components such as in wood shear walls (Minghao et al., 2012), and in 3D light-frame structures (He et al., 2001).

2.2 Numerical Model

In the case of lightweight roof trusses, the connections between the trusses and the top plate have historically been toe-nailed, as shown in Figure 2.1. Such connections are weak with respect to resisting wind-generated uplift forces. The capacity of toe-nail connections under uplift loads has been examined through tests conducted on a full-scale two-story gable roof house at the IRLBH (Morrison et al., 2012). The plan of this experimental house was approximately 9 m by 9 m with a roof pitch of 1:3 (Figure 2.2). The roof of the house consisted of 16 trusses spaced 0.6 m apart, all having a roof overhang of 0.5 m in each direction. The middle 14 trusses were supported by two RTWCs on the north and south sides of the house while the remaining trusses were gable end trusses on the eastern and western sides, which were supported by walls as well as RTWCs on the north and south sides. On average, three twisted shank nails, either 12D or 16D, were used for each RTWC.
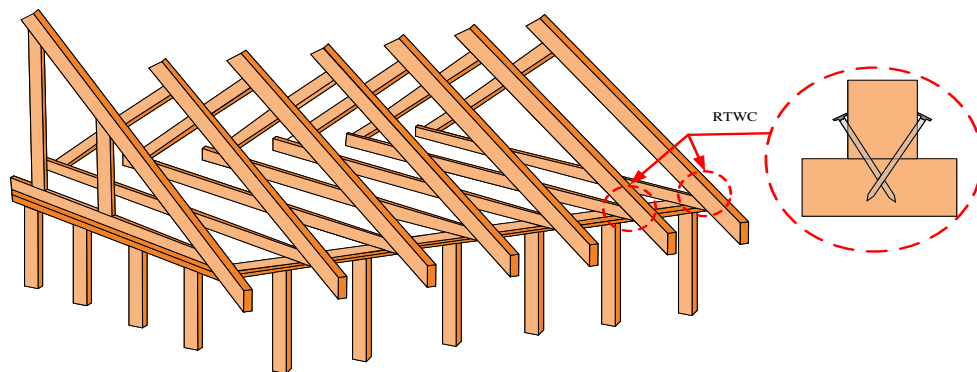
Figure 2.1: Segment of a light-frame wood structure, with an inset view of an RTWC.

The wind load was simulated with the use of 58 pressure boxes that created suction pressure on the roof of the test house (Figure 2.2). To determine the appropriate pressure, a wind tunnel test was conducted as a means of establishing realistic wind loads, for which a 1:50 scale model was designed in order to measure realistic loads under flows

from 18 wind directions across open terrain. Full-scale pressure was applied at a 40º angle because this pressure produces the greatest reaction generated on RTWCs. The experimental test was performed in six loading stages, ranging from wind speed of 20 m/sec up to complete failure of the roof at wind speed of 45 m/sec. All load steps were varied both spatially and temporally, with each load stage having a different loading period. Further details about the experimental test can be found in (Morrison et al., 2012).

At the wind speed of 45 m/sec, the roof failed at the RTWCs, and no failure occurred at the truss's members because the stresses induced in these members were significantly less than their capacities.

Dessouki (2010) introduced a sophisticated numerical simulation using SAP2000 commercial software, which was subsequently developed further by Jacklin (2013). The work presented in this chapter was based on this latter version of the model, but the investigation has been expanded to cover the examination of more realistic wind loads in a nonlinear range associated with the occurrence of permanent withdrawal in the RTWCs. The dimensions and loading included in the new numerical model are similar to those of the experimental gable roof house previously tested at the IRLBH (Morrison et al., 2012). As shown in Figure 2.2, the new numerical model incorporates 16 Howe trusses modelled as frame elements, each of which has two nodes, with six degrees of freedom at each node. To increase the stiffness of the end trusses, four extra webs have been added. The top and bottom chords of the trusses are 2 in. by 4 in. (50 mm. by 101 mm.), and the webs are 2 in. by 3 in. (50 mm. by 76 mm.). All of the middle trusses are supported by two RTWCs except for the gable end trusses, which are assumed to be backed by seven RTWCs in order to simulate the bearing behavior of the end walls. The 9 mm roof sheathing is modelled using 2112 shell elements, each of which connected with all top truss chords by body constraints. These shell elements that have four nodes, with six degrees of freedom at each node (three translations and three rotations), which can capture both membrane and bending forces. The nonlinearity portion of the finite element model represents the nonlinear stiffness of the RTWCs, which are therefore modelled as nonlinear spring elements. Besides, there was an overhang of sheathing about 0.5 m in all directions. A rigid diaphragm was assigned at the level of top plate

members. At that level, linear springs were allocated to account for the in-plane stiffness of the shear walls. This in-plane stiffness was estimated as linear approximation from the experimental testing conducted by Kasal et al., (1994).
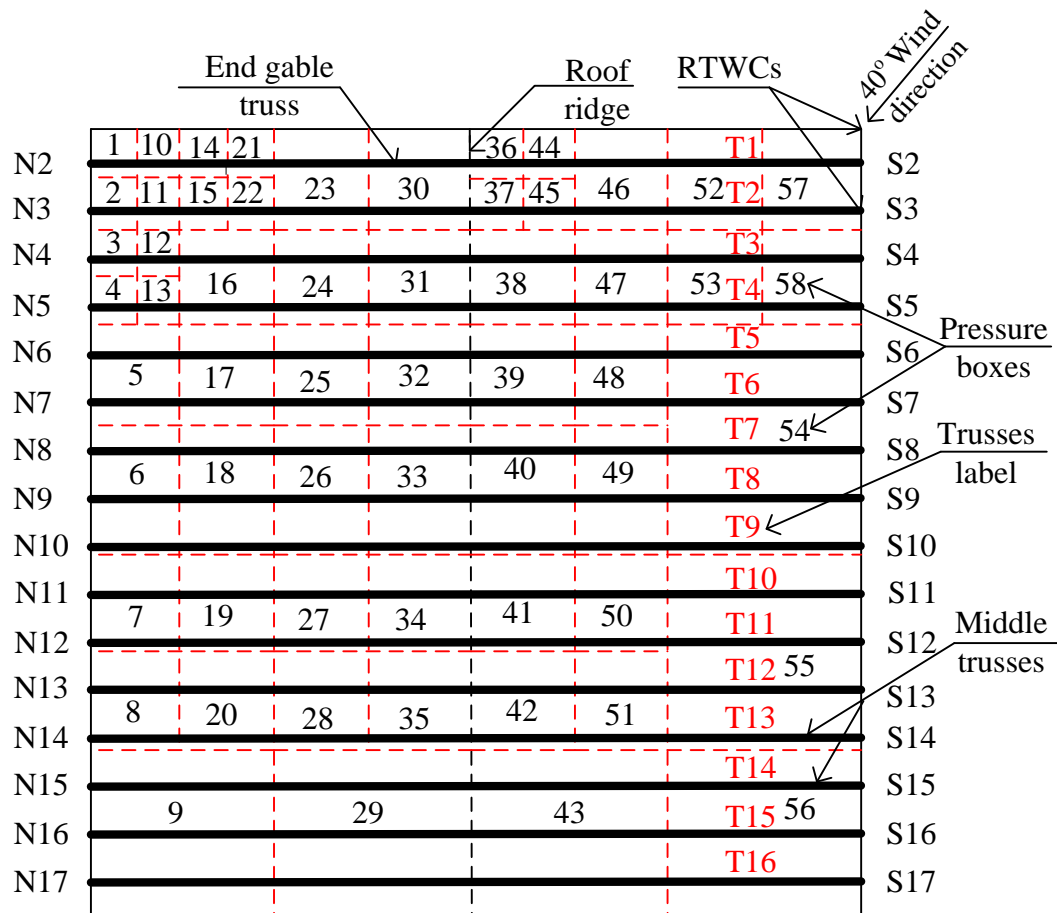
Figure 2.2: Layout of the numerical model proposed by Jacklin (2013).

As proposed by Morrison et al., (2012), when a connection exceeds the damage peaks evident in the displacement time history, that connection exhibits plastic behavior as a result of permanent withdrawal. For this reason, Jacklin (2013) used two types of nonlinear link elements for their RTWCs model: gap elements and multi-linear plastic elements. Gap elements carry only compression loads and were utilized in the model as a

means of reducing negative deflection through the setting of a high degree of stiffness in compression. The second type of element addresses the tension forces generated from the suction pressure. To model this kind of behavior, a multi-linear load deflection relation, as shown in Figure 2.3. This relationship was based on the nonlinear curve resulting from the experimental testing performed by Morrison and Kopp (2011). Experimentally, the load-deflection relation of toe-nailed RTWCs had high variability (Reed et al., 1997, Khan. 2012). However, the numerical model in this chapter was carried out using an identical load-deflection relation for all RTWCs. In the case of hurricane clips connections, Chowdhury et al., (2013) and Satheeskumar et al., (2017) showed that the withdrawal capacity of these connections could be reduced due to the combination of lateral and uplift load. However, the roof-to-wall connections used in this chapter were toe-nails under the effect of wind uplift loads only. Morrison and Kopp (2011) stated that in case of roof pitch 1 to 3, the toe-nail connections received approximately 5 % from the wind uplift loads as shear loads. The dominant failure of toe-nails is nail-withdrawal (Shanmugam et al., 2009; Guha and Kopp 2014). The roof-to-wall connections herein were modelled as nonlinear spring elements. These elements accounted for the relative deformation between the walls and the roof in the direction parallel to the toe-nails withdrawal. The other two directions were set to be rigid, so there was no relative deformation between the trusses and the walls in the directions perpendicular to the toe-nails withdrawal. The extra shear loads resulting from the resolution of the uplift loads will be resisted by the linear springs, which simulate the in-plane stiffness of the shear walls. Detailed information about the numerical model can be found in (Jacklin 2013).
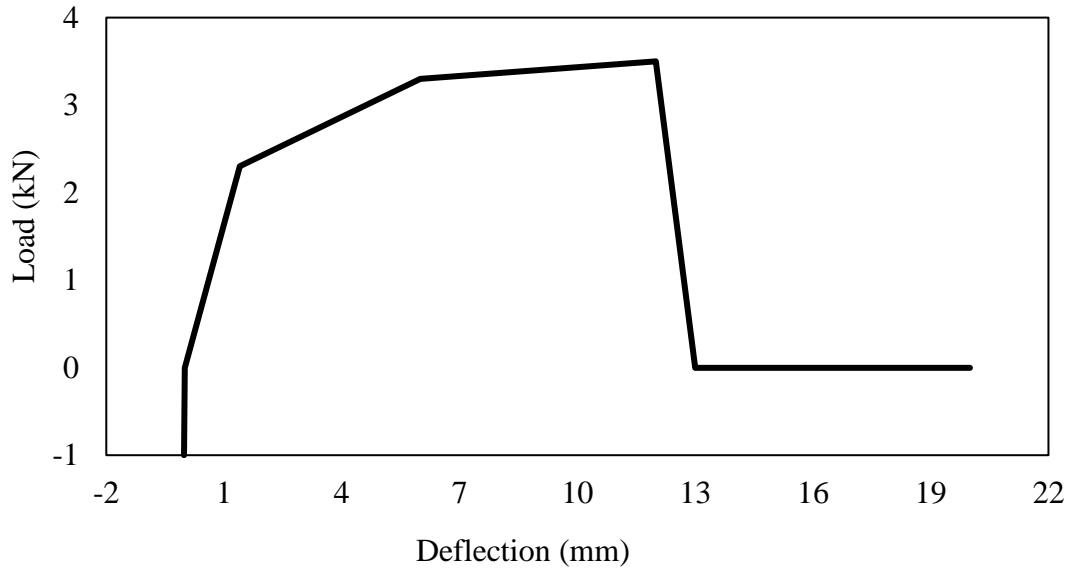
Figure 2.3: Load-deflection relation for all connections, as proposed by Jacklin (2013).

2.3 Validation of the Numerical Model

To evaluate the performance of the numerical model against the experimental testing, the predicted RTWCs deflections were compared with the experimental results. The experimental data was too large, in the order of 30,000 data points for the 30 m/sec wind speed and 20,000 data points for the 45 m/sec wind speed. It was not practical to analyze the model nonlinearly under such large number of data points. So performing a complete numerical analysis for the full loading time history is computationally expensive. As a solution, the analysis focussed on 1000 time steps within the range of maximum and minimum values of the loading at each speed as shown in Figure 2.4. In Figure 2.4 example, four data sets of realistic uplift wind load pressure values were applied in the numerical model. These demand data sets represent a variety of wind speeds, beginning with 30 m/sec and increasing in 5 m/sec increments up to complete roof failure at 45 m/sec, when permanent withdrawal occurs in the RTWCs. For example, data set one represents the lowest percentage of permanent withdrawal of the RTWCs at 30 m/sec, while data set four, at 45 m/sec, correlates with maximum RTWCs withdrawal. All of the

selected uplift wind load pressures thus produce plastic behavior in the connections. Based on the example shown in Figure 2.4, the RTWC responses exhibit erratic fluctuations that correspond to loading peaks and unloading troughs. Plastic RTWC withdrawal occurs primarily at peak uplift pressure (Morrison et al., 2012). During the experimental results, especially in the nonlinear range of wind speed between 30 m/sec and 45 m/sec, there was a permanent withdrawal in RTWCs (Morrison et al., 2012). And in order to compare the experimental results, the numerical prediction should be shifted up by the previous withdrawal in the whole time history, since the numerical analysis was based on initial zero deflection. The ability of the numerical model to predict accurately the incremental difference taking non-linear behavior into account is assessed.

The pressure applied on the roof of the house was varied both spatially and temporally so that the 58 pressure boxes created a different intensity at each time step. For example, the numerical model was analyzed with the 20 sec intervals divided into 1000 time steps, each of which was associated with the spatial pressure values shown in Figure 2.2. For the purposes of the nonlinear finite element analysis, the pressure is applied incrementally in a quasi-static time history manner under 1000 time steps. For example, step one includes the dead weight of the roof plus the spatial pressure associated with step one. Step two then begins with the initial step one condition plus the difference between the spatial pressure values associated with steps one and two, continuing in this manner until the analysis has been conducted for all of the time steps. This quasi-static analysis is also performed by Kumar et al., (2012) to assess the performance of gable roof house under tornado loading. In this chapter, the analysis strategy is based on the assumption of an initial zero withdrawal in the first time step and does not take into account any previous withdrawal. Jacklin (2013) therefore proposed an approximated assumption for modifying the numerical analysis output by taking the differences between the experimental results and the numerical predictions at each RTWC for the first time step and then adding these differences to all time steps. This approximation is a reasonable prediction since the analysis is based on neglecting any previous plastic damage that occurred at the previous peaks in the pressure time history. The numerical model accounted for the dead weight of the structural members such as truss members,

sheathings, and cross members between the trusses. However, the numerical model did not account for the weight of the non-structural elements such as roof-shingles since they were removed during the experimental testing as mentioned by Morrison et al., (2012).
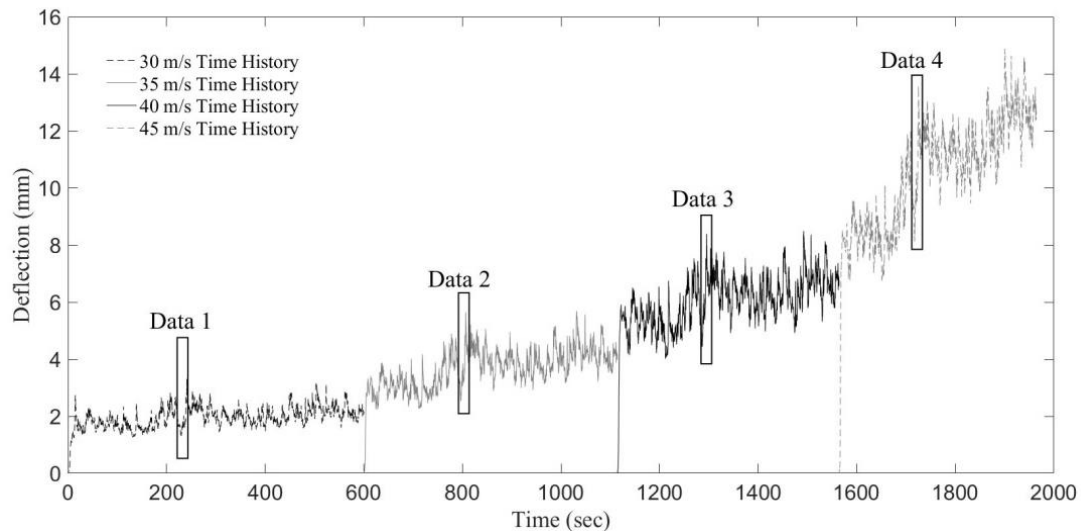
Figure 2.4: Time history displacement for RTWC S6 Morrison et al., (2012).

Figures 2.5 and 2.6 provide a comparison of the experimental results and the numerical deflection predictions with respect to the deflection of all of the RTWCs. The deflections were evaluated for four wind speeds: 30 m/sec and 35 m/sec (Figure 2.5), and 40 m/sec and 45 m/sec (Figure 2.6) under the effects of the ultimate applied pressure during the associated time history. As shown in Figure 2.5, good agreement exists between the experimental deflections and the predicted deflections on the north and south sides in terms of magnitude and trend. With reference to the mean numerical values for wind speeds of 30 m/sec and 35 m/sec, the maximum differences between the experimental and the numerical deflection values are 0.3 mm and 0.4 mm, respectively, resulting in percentages of difference between the mean numerical and mean experimental values of 7.1 % and 5.8 %, respectively.
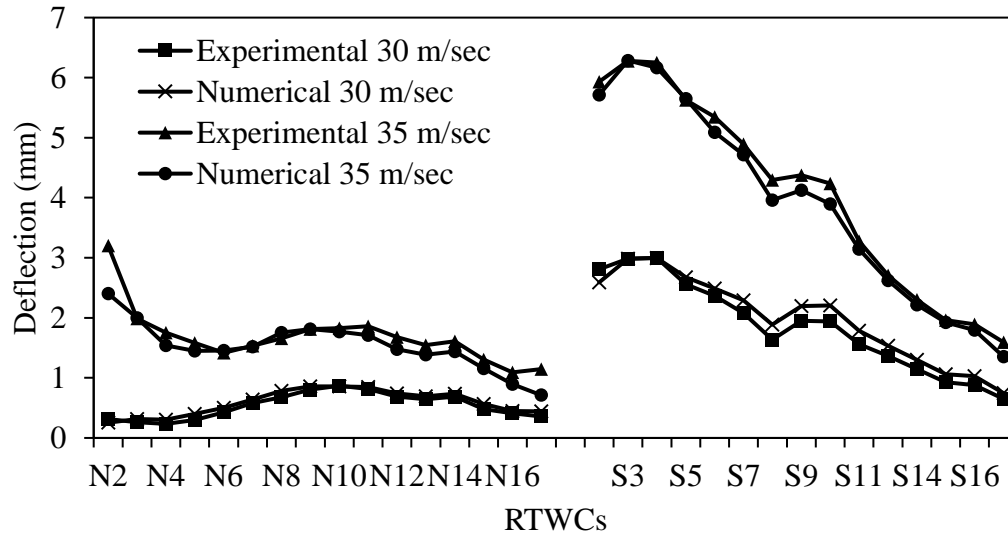
Figure 2.5: Experimental and numerical deflection values for all RTWCs on the north and south sides under the maximum global uplift pressure from wind speeds of 30 m/sec at time step 900 and of 35 m/sec at time step 633.

When the ultimate applied pressure increases with speeds above 35 m/sec, the differences between the predicted numerical deflections and the experimental deflections increase, primarily on the south side under the maximum global uplift that corresponds to the 45 m/sec failure speed. These differences resulted mainly because a complete full-time history analysis was not performed, with the focus being only on the maximum and minimum uplift pressure values in data set four, as illustrated in Figure 2.4. An additional factor was the fact that the analysis were based on a modification of the output numerical predictions assumed by Jacklin (2013). However, as evidenced by Figure 2.6, the output values are quite reasonable. For example, the maximum deflection differences between the experimental results and the finite element predictions are 3.8 mm and 5.8 mm for wind speeds of 40 m/sec and 45 m/sec, respectively. These differences result in percentage differences between the mean finite element predictions and the mean experimental results of 20.7 % and 23.6 % with reference to the mean numerical values for the 40 m/sec and 45 m/sec wind speeds, respectively.
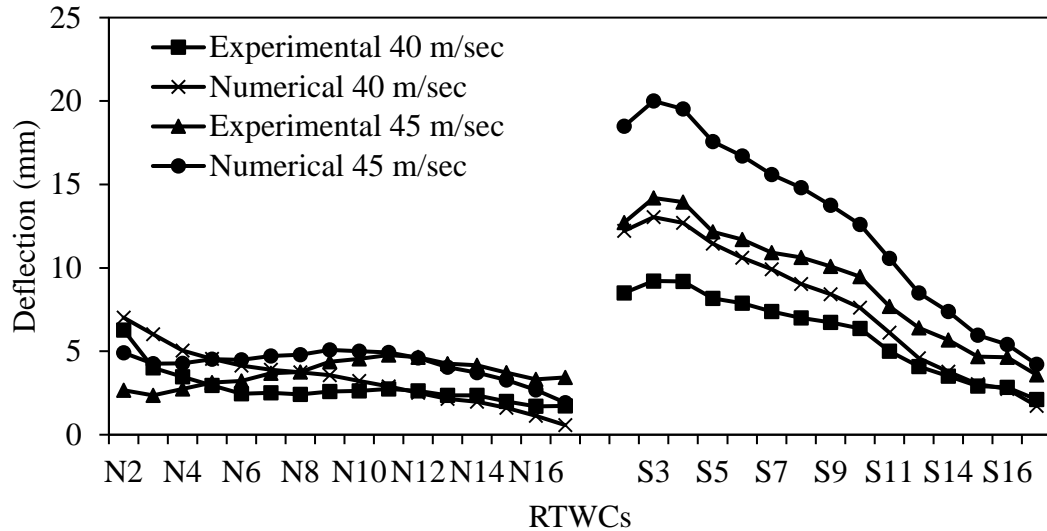
Figure 2.6: Experimental and numerical deflection values for all of the RTWCs on the north and south sides under the maximum global uplift pressure from wind speeds of 40 m/sec at time step 991 and of 45 m/sec at time step 210.

Figures 2.7 and 2.8 provide a comparison of the finite element predictions and the experimental test results for all RTWCs deflections on the north and south sides of the roof under the least amount of global uplift pressure for four wind speeds ranging from 30 m/s to 45 m/sec. As shown in Figure 2.7, the comparison reveals that both the numerical and the experiment curves exhibit the same trend. However, the deflection differences between the numerical predictions and the experimental results under the least uplift pressure are greater than the deflection differences under the maximum global uplift. With reference to the mean numerical values for pressures from wind speeds of 30 m/sec and 35 m/sec, these differences reach values of 0.6 mm and 0.5 mm, respectively, with percentages of difference between the mean numerical and the mean experimental deflection values of 17.7 % and 13.6 %, respectively. A comparison of Figures 2.5 and 2.7 reveals that both graphs indicate that the south side of the roof exhibits greater deflection than the north side due to the higher pressure intensity on the south side. Figure 2.7 also shows zero deflection values for RTWCs N2 to N6, especially under the minimum pressure exerted by a wind speed of 30 m/sec. This happened when the self-

weight of the roof was equal to the loads arising from the uplift pressure. As observed experimentally by Doudak et al., (2012), the tension and compression reactions were evaluated due to unsymmetrical gravity loads.
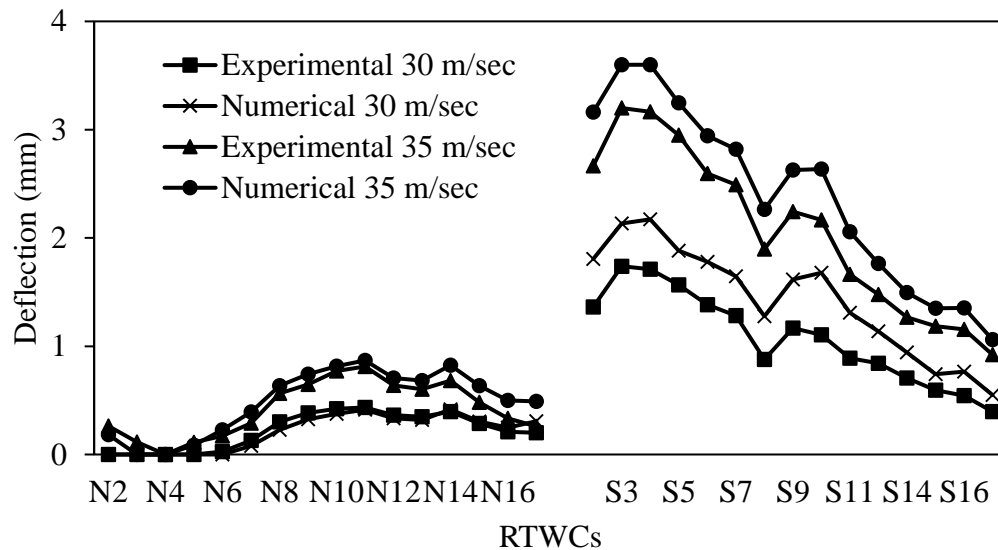
Figure 2.7: Experimental and numerical deflection values for all RTWCs on the north and south sides under the minimum global uplift pressure from wind speeds of 30 m/sec at time step 378 and of 35 m/sec at time step 116.

Figure 2.8 shows the greatest variation recorded between the numerical and experimental test deflection values under minimum applied uplift pressure. With reference to the mean numerical values under pressure from wind speeds of 40 m/sec and 45 m/sec, the maximum differences recorded were 3.3 mm and 9.6 mm, respectively, with percentages of difference between the mean numerical and the mean experimental deflection values of 31.9 % and 49 %, respectively. However, this variation occurred because the same load-deflection curve shown in Figure 2.3 was assumed in the numerical analysis, which does not represent the exact situation. Reed et al., (1997) conducted experimental testing on individual toe-nail connections and concluded that the coefficient of variation for the

ultimate uplift capacity reached about 25 %. As shown in Figures 2.6 and 2.8, these variations in results have a significant effect on high-speed loads such as those at 40 m/sec and 45 m/sec, particularly in the nonlinear range associated with permanent withdrawal, due to the variability of the connection stiffness.
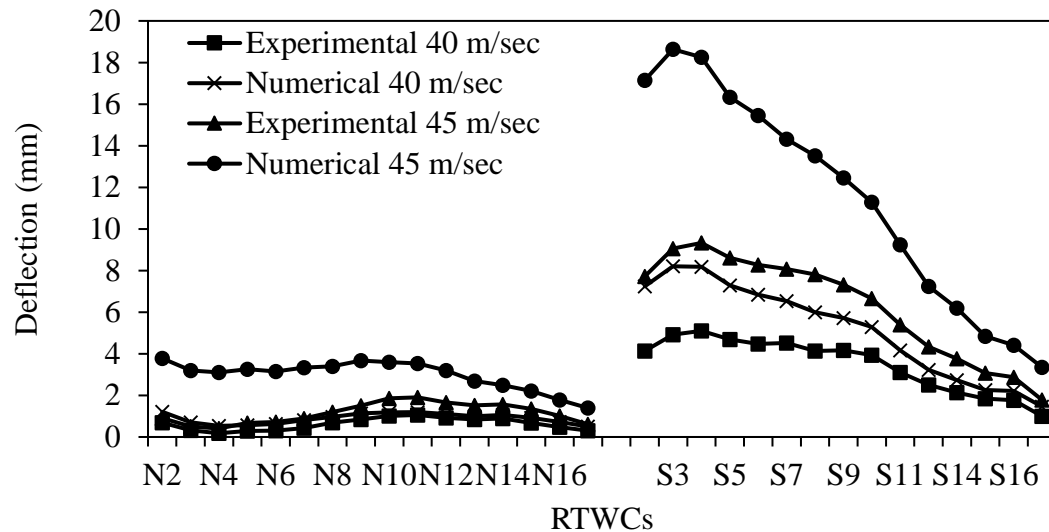
Figure 2.8: Experimental and numerical deflection values for all RTWCs on the north and south sides under the minimum global uplift pressure from wind speeds of 40 m/sec at time step 540 and of 45 m/sec at time step 593.

Figures 2.9 and 2.10 illustrate the deflection values for RTWC S3 through the time history associated with pressure from four wind speeds ranging from 30 m/sec to 45 m/sec. Of all the RTWCs, RTWC S3 was observed to exhibit the greatest deflection measurements (Morrison et al., 2012). As shown in Figure 2.9, good agreement exists between the numerical and the experimental deflection values with respect to the magnitude and shape of the curves. However, the maximum differences between the measured and expected deflections are 0.6 mm and 0.9 mm under the pressure of wind speeds of 30 m/sec and 35 m/sec, respectively.
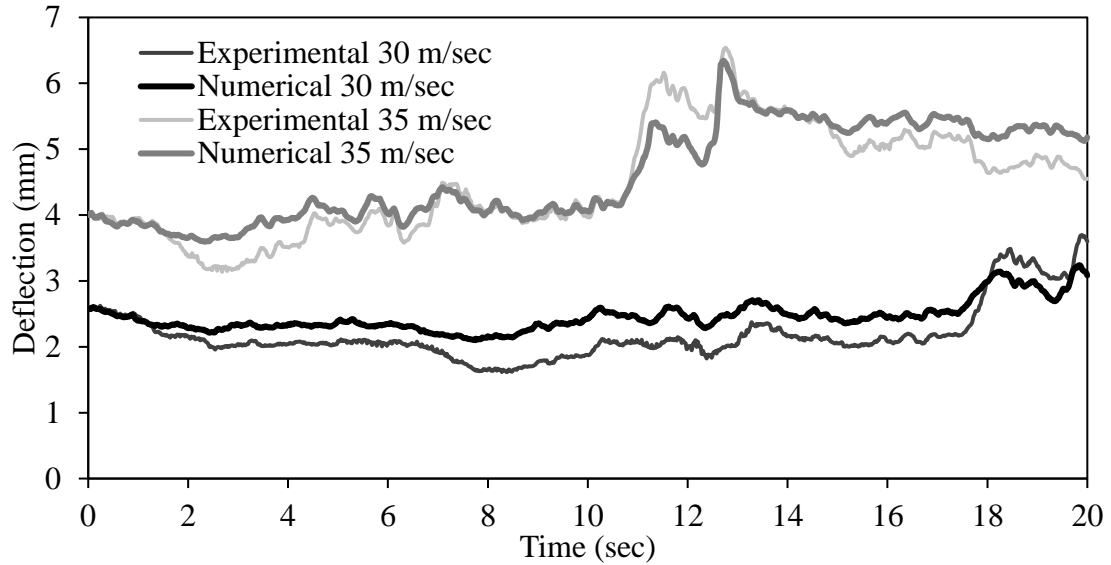
Figure 2.9: Experimental and numerical deflection values for RTWC S3 during the time history for wind speeds of 30 m/sec and 35 m/sec.

At higher applied uplift pressures (wind speeds of 40 m/sec and 45 m/sec), the difference between measured and expected deflection values increased because the ultimate capacity or the failure of the RTWCs was reached. Figure 2.10 indicates the differences between the experimental and numerical deflection values for RTWC S3 at the greater amounts of pressure from wind speeds of 40 m/sec and 45 m/sec. At the 40 m/sec loading stage, good agreement exists during the first 2 sec, following which, the difference between the deflections is a maximum of 4 mm. For the failure uplift speed of 45 m/sec, the deflections during the first 4 sec reflect only small differences, and then an almost consistently greater difference in deflection is apparent, with a maximum value of 9.6 mm. From Figure 2.10, it can be seen that the numerical model is able to capture the deflection that occurs between time step 1 and time step 938. The reason the analysis stops at time step 938 is that the total uplift predicted is greater than any of the RTWCs capacities. In summary, the output of the numerical model produces good prediction results following permanent withdrawal under speeds ranging from 30 m/sec to 40 m/sec. When the uplift load reaches failure, in this case, 45 m/sec, the numerical model tends to overestimate the actual deflections. This overestimation is attributable to the similar

stiffness values of the RTWCs used in the study, which, in reality, can vary depending on the nature of the wood connections.
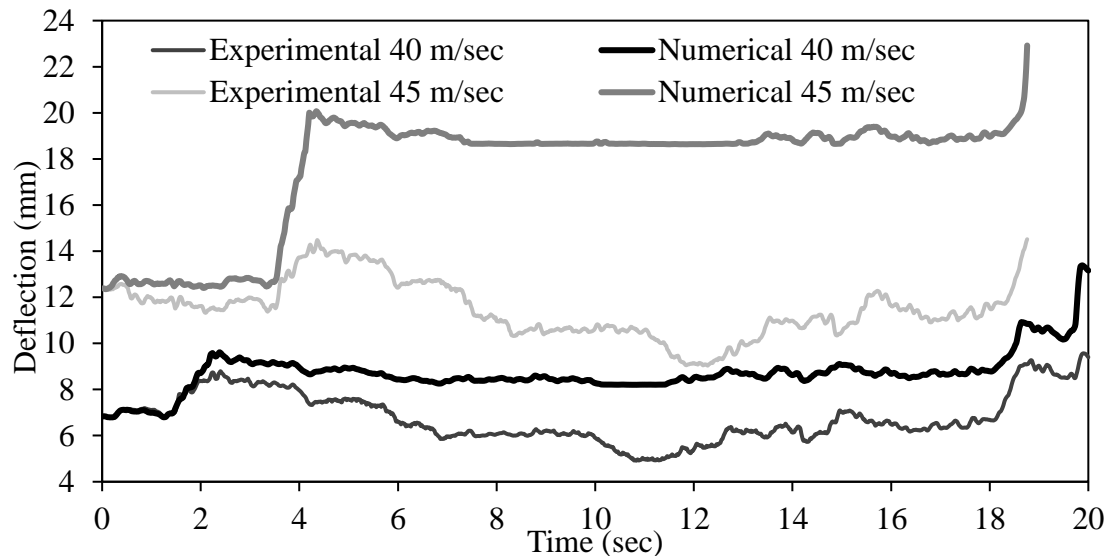
Figure 2.10: Experimental and numerical deflection values for RTWC S3 during the time history for wind speeds of 40 m/sec and 45 m/sec.

2.4 Load Sharing between Trusses

Once the results produced by the numerical model had been validated against the experimental findings, the load sharing among the trusses could be evaluated in order to determine how the uplift load is transferred among them. Several experimental studies have been undertaken aimed to determining the load sharing throughout wood houses components. For example, Doudak et al., (2012) investigated the internal load transfer through gable roof house due to lateral and gravity loads. Moreover, Henderson et al., (2013) evaluated the change of Influence coefficients for each RTWCs under simulated uplift wind loads for hip roof house during permanent withdrawal of RTWCs. Datin and Prevatt (2013) estimated the influence functions for a small-scale gable-house by applying concentrated uplift loads on different locations at the roof in order to measure

the reactions of the load cells located at RTWCs and at wall-to-foundation connections (WTFCs).The load share of each truss is defined herein as the ratio of the support reaction of each truss to the total uplift load. In this particular study, the self-weight of the roof is neglected so that the effects of the wind uplift loads could be compared separately. The load sharing was computed using both FEM (the numerical model) and the tributary area method (TAM) for three load cases: realistic pressure, code pressure, and uniform pressure.

Figure 2.11 illustrates the load sharing calculated by the numerical model for each truss under the realistic pressure derived from the experimental testing conducted by Morrison et al., (2012). Load sharing was also evaluated with respect to the maximum global uplift loads for a variety of wind speeds. It is clear from Figure 2.11 that the gable end trusses, T1 and T16, are subject to a greater load share than the middle trusses. End gable truss T1, which is connected between RTWC N2 and RTWC S2, has 23.8 % and 19.5 % of the load share for wind speeds of 30 m/sec and 45 m/sec, respectively. End gable truss T16 extracts a lesser load share of 6.6 % and 9.5 % for wind speeds of 30 m/sec and 45 m/sec, respectively. The average load sharing by both end gable trusses for speeds varying from 30 m/sec up to 45 m/sec is evaluated to be 29 %. This percentage is similar observation found by Zisis and Stathopoulos (2012). The reason that truss T1 is subjected to a greater load share than truss T16 can be attributed to the high degree of pressure intensity that occurs at truss T1 compared with that at truss T16, as shown in Figure 2.13.

Figure 2.13 indicates that the pressure distribution is more concentrated at truss T1 and that the pressure decreases gradually toward truss T16. In addition, the south side is subjected to greater pressure intensity than the north side. However, the north side also exhibits some peak pressure values that are concentrated on small box areas, such as boxes 10 and 14. For the maximum uplift wind load, Figure 2.12 illustrates the load shares of all of the trusses except the gable end trusses. As shown in Figure 2.12, the load sharing for all of the middle trusses under the pressure resulting from speeds of 30 m/sec to 40 m/sec follows the same trend, indicating that the RTWCs at these trusses do not reach their maximum capacity. However, at the failure wind speed of 45 m/sec, as given by Morrison et al., (2012), some of the middle trusses reach maximum capacity. The zero

slope of the load sharing under the highest pressure at 45 m/sec indicates that the RTWCs at trusses T2 to T8 reach their connection capacities and that roof failure is initiated in this zone.
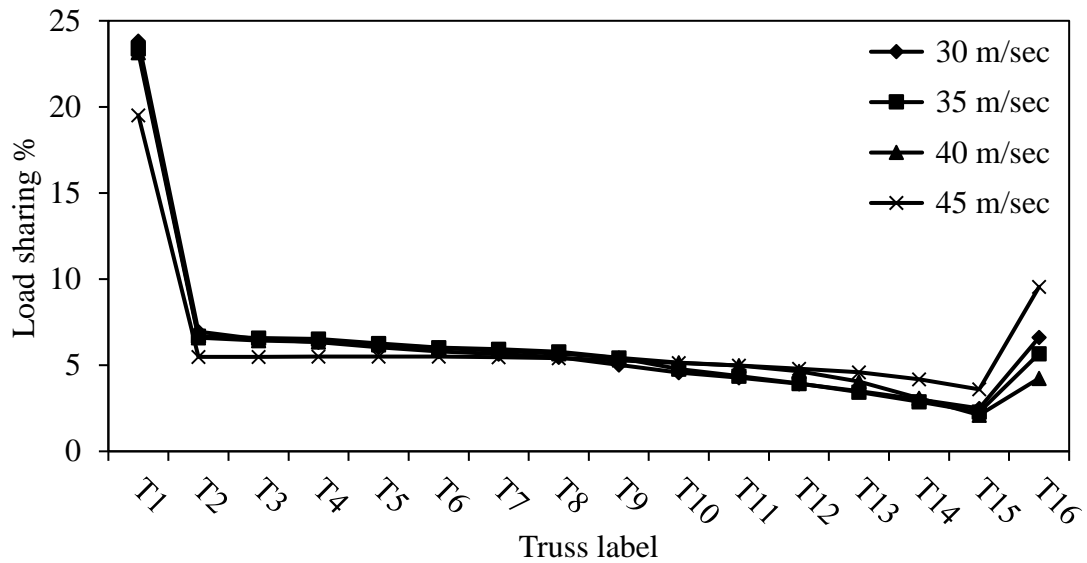
Figure 2.11: FEM results indicating load sharing for all trusses at the maximum global uplift load.
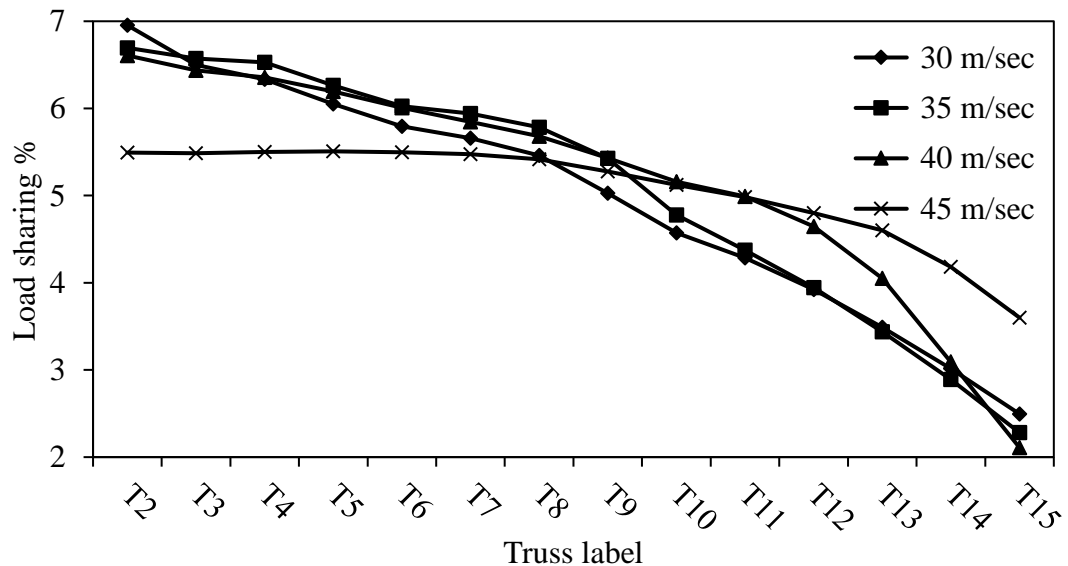
Figure 2.12: FEM results indicating load sharing for all of the middle trusses at the maximum global uplift load.
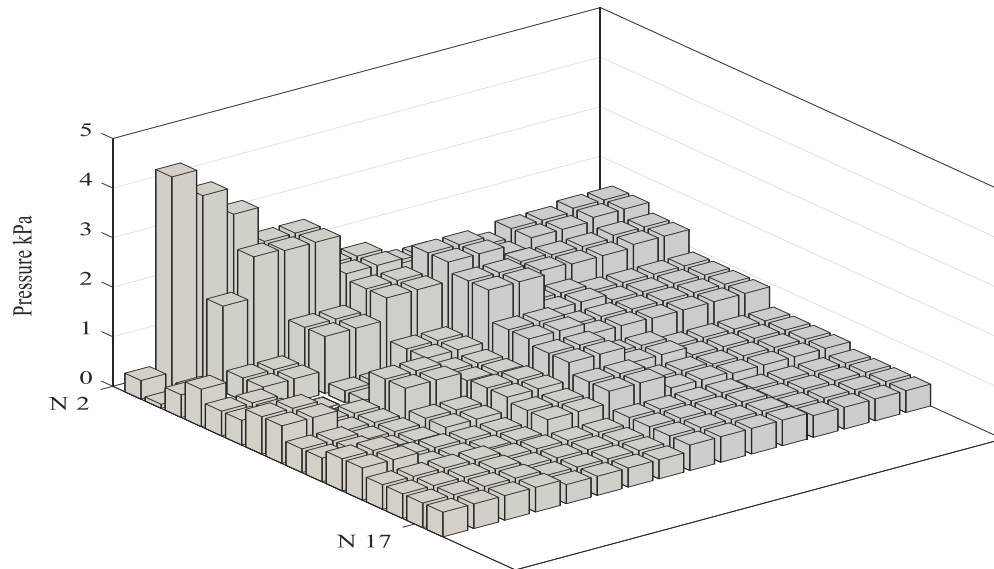
Figure 2.13: Distribution of pressure over the roof under the maximum global uplift at 35 m/sec (Morrison et al., 2012).

Instead of FEM, the tributary area method can be used for easily estimating approximate reactions at the RTWCs. With this approach, the pressure on the sheathing is distributed toward the nearest trusses based on the position of the trusses with respect to the pressure, rather than on the stiffness of the trusses. For example, if the pressure on the sheathing is supported by two trusses which have different degrees of stiffness, if the tributary area method is used, both trusses would share the same loading, which does not reflect the real situation. This method is thus reliant on the assumption that the horizontal diaphragm is flexible and that each truss works independently to transfer the loads towards the RTWC, as discussed by Kasal et al., (2004). In the study presented in this chapter, the realistic pressure, as defined according to the 58 pressure boxes, whose layout is shown in Figure 2.2, is distributed to all of the trusses. Each truss supports half of the pressure from the east and west sides as a line load, and this line load is then applied to the top chords of the trusses in order to obtain the reactions created in the RTWCs, which function as rigid supports.

Figure 2.14 enables a comparison of the calculations of the load share by the numerical model and the tributary area method for end gable truss T1 under the effects of a wind speed of 40 m/sec throughout the time history. As shown in Figure 2.14, both analysis methods exhibit the same trend, with a constant average difference of 8 %. The output from the tributary area method tends to represent an underestimation of the load sharing, a result that occurs for two reasons: first, the higher degree of stiffness in the gable end truss than in the middle trusses is not taken into account, and second, for the three-dimensional analysis, FEM includes consideration of the effects of outlying pressures on the reactions of all RTWCs. However, to sustain the equilibrium of the global uplift loads, the tributary area method provides greater estimated load shares in the middle trusses, such as truss T4, for example, where the average order of difference is 1.8 %, as shown in Figure 2.15. It should be noted that when the speed is increased, the average difference does not vary greatly between the numerical model and the tributary area method results with respect to the load sharing among the trusses. For example, the average differences between the results produced by the numerical model and those calculated using the tributary area method are in the range of 7.1 % and 9.0 %, respectively, for truss T1 and 1.3 % and 2.0 %, respectively, for truss T4.
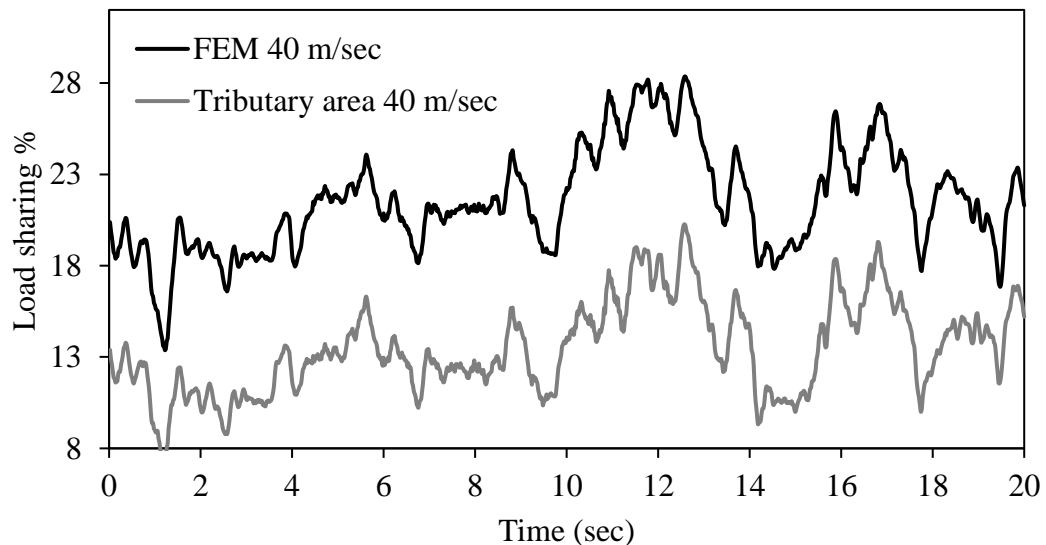
Figure 2.14: Comparison of load sharing computed using the tributary area method and FEM predictions for end gable truss T1.
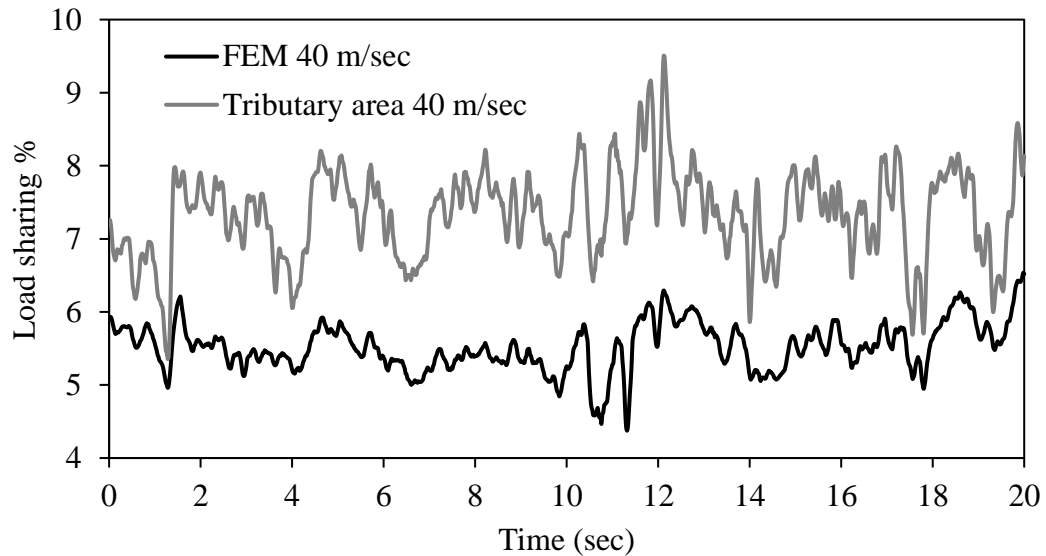
Figure 2.15: Comparison of load sharing computed using the tributary area method and FEM predictions for middle truss T4.

Figure 2.16 presents the results for the load sharing among the trusses under the pressure exerted by a wind speed of 35 m/sec, which represents the code pressure, as evaluated based on the National Building Code of Canada (2010). Four zones represent the uplift pressure: 2, 2E, 3, and 3E, with the greatest pressure at 2E in the southeast direction where the wind loads act on the structure as shown in Figure 2.2. Open terrain exposure has been selected in order to obtain the pressure on the roof. Figure 2.16 shows a comparison of the results using the numerical model and those computed using the tributary area method for evaluating the load sharing among the trusses. It can be seen that the tributary area method produces underestimates of the load shares at the gable end trusses by an average difference of 7.3 % and overestimates of the load shares for the middle trusses by an average difference of 1.0 %. These discrepancies arise with this method because the stiffness of the gable end trusses is not included in consideration. The load distribution evaluations produced by the tributary area method indicate a higher load share percentage allocated at trusses T2 to T9 than at the other middle trusses because the distribution is based on the intensity of the pressure. However, the load distribution determined using FEM shows less variation in the middle trusses than with the tributary

area method, which indicates that the FEM distribution is reliant mainly on the stiffness of the intermediate trusses.
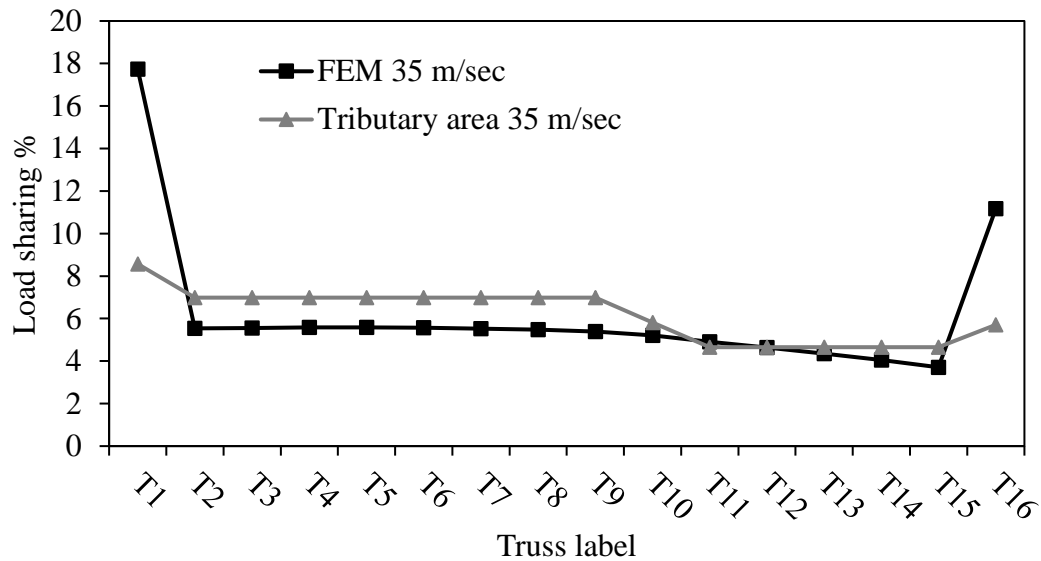
Figure 2.16: Comparison of load sharing computed using the tributary area method and the FEM results under code pressure.

Figure 2.17 shows the truss load shares calculated by the numerical model and the tributary area method under uniform pressure from a wind speed of 35 m/sec. The uniform pressure was evaluated as the weighted average of the 58 pressure boxes for the maximum global uplift at time step 633. The uniform pressure was utilized in order to identify the effect of truss stiffness on the load sharing when finite element analysis is used. As can be seen in Figure 2.17, the numerical model calculated identical load shares for the end gable trusses due to these trusses having the same stiffness. Middle trusses with the same stiffness have slightly different load shares with symmetric elliptic shapes because of the flexural stiffness of the sheathing between the trusses. Otherwise, the tributary area method tends to compute the same load sharing at the middle trusses under uniform pressure, a result that is attributable to the use of similar widths for the trusses, with the exception of the gable end trusses, whose extra width accommodates the overhang.
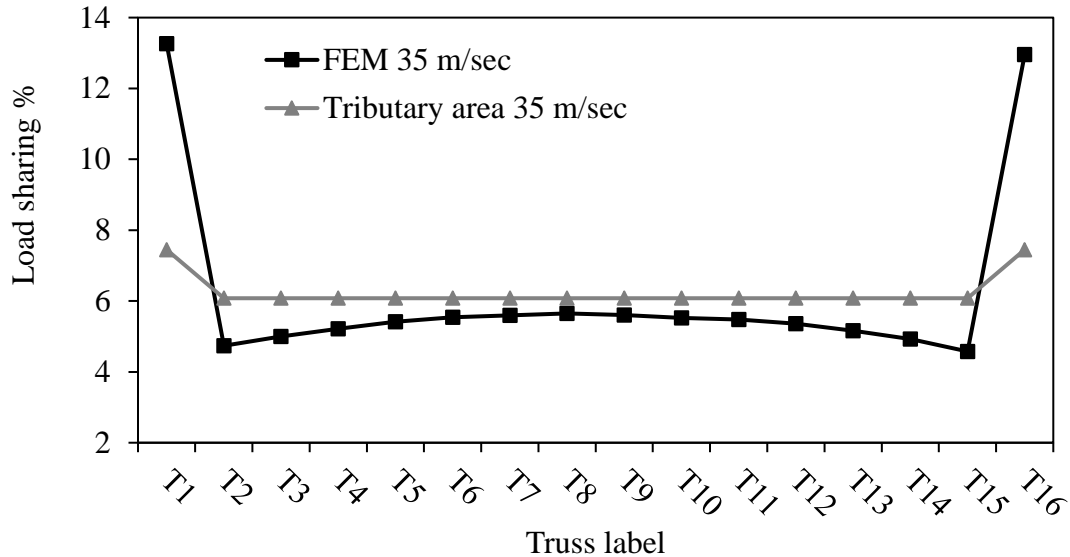
Figure 2.17: Comparison of load sharing computed using the tributary area method and the FEM results under uniform pressure.

Figure 2.18 presents the output of the numerical model for two load cases: loads created by the maximum realistic pressure at time step 633, and loads under the code pressure. It can be seen that the two cases are characterized by similar load sharing at the middle trusses because both cases involve a graduated pressure distribution over the roof. However, differences appear with respect to the gable end trusses, where truss T1 is subjected to a greater load sharing percentage than truss T16 when the maximum realistic pressure is applied. Figure 2.19 provides a comparison of the results from two methods of evaluating the load sharing of the trusses: the tributary area method with the code pressure and the numerical model analysis with the maximum global applied realistic pressure. This comparison was conducted in order to assess the differences between simple analysis and more complicated ones. Figure 2.19 reveals that the load sharing results obtained from both analyses are similar for all trusses but that the load share of end gable truss T1 is greater than that for truss T16 due to a combination of the greater pressure exerted at T1 and its higher degree of stiffness.
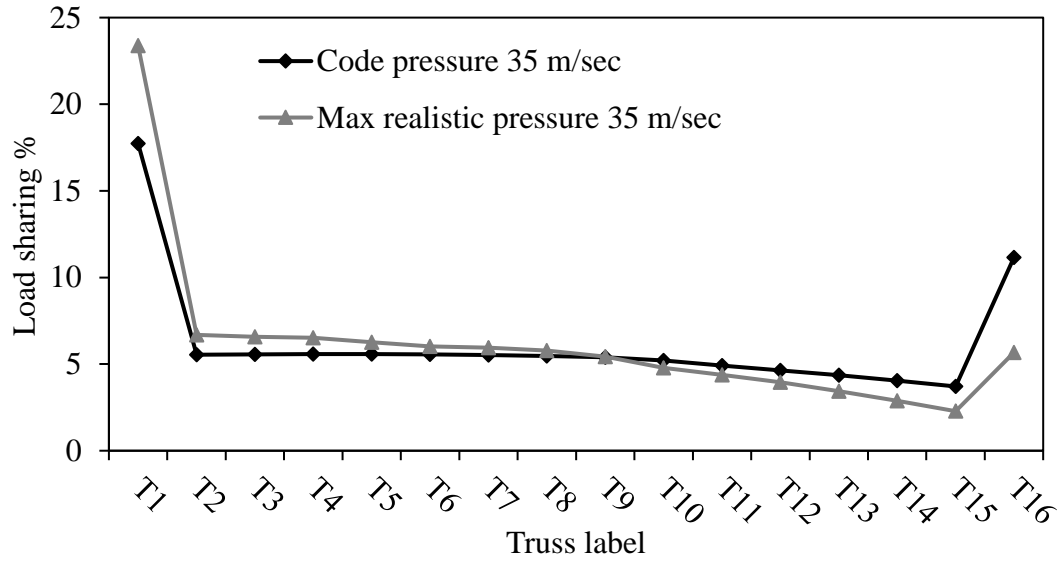
Figure 2.18: Comparison of load sharing with the code pressure and the maximum realistic pressure obtained from FEM.
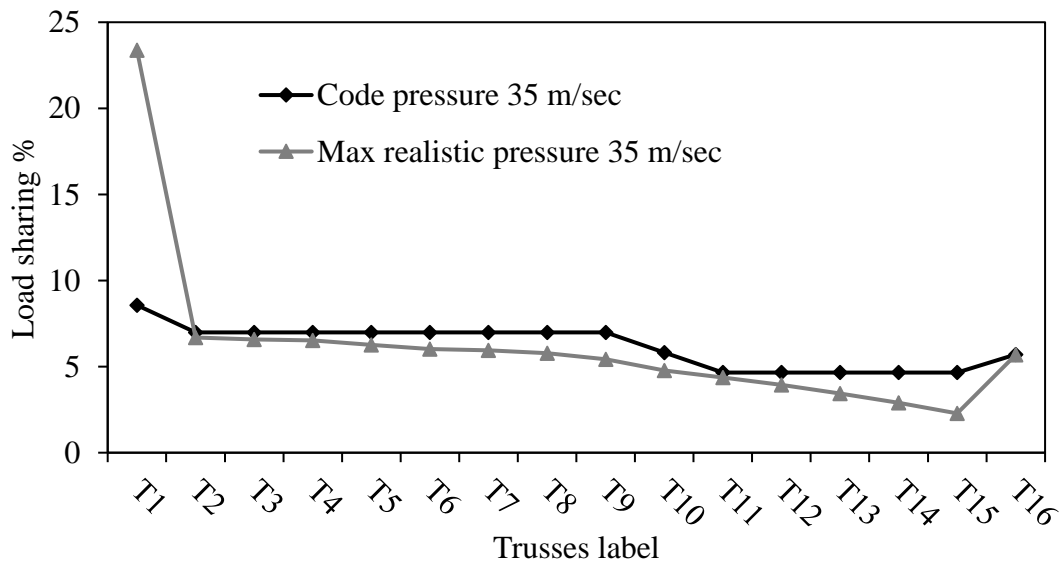
Figure 2.19: Comparison of load sharing with the code pressure (tributary area method) and the maximum realistic pressure (FEM).

2.5 Conclusion

This chapter has presented an examination of the use of both FEM and the simple tributary area method for the analysis of gable roof trusses subjected to uplift wind loads under the pressure of a variety of wind speeds. For the purposes of this study, three categories of pressure were considered: realistic pressure, code pressure, and uniform pressure. Realistic pressure, which varies with respect to time and space, was based on experimental testing conducted at the Insurance Research Lab for Better Homes located at the University of Western Ontario (Morrison et al., 2012). The uniform pressure was established as a weighted average of each pressure box at the maximum global uplift load. The code pressure was estimated based on the National Building Code of Canada (2010).

The numerical model was validated against the experimental results under the realistic pressure in order to evaluate the performance of the predicted deflections at the RTWCs. Good agreement regarding the RTWCs deflections was obtained for minimum and maximum global uplift loads, especially at wind speeds of 30 m/sec to 40 m/sec. However, differences between the numerical and experimental deflections were observed under the pressure associated with the failure speed of 45 m/sec, with a maximum difference of 9.6 mm apparent at RTWC S3. This difference occurs due to the use of the same load-deflection relationship for all of the RTWCs. As discussed by Reed et al., (1997), the ultimate uplift capacity of toe-nail connections has a coefficient of variation of about 25 %, depending on the nature of the wood.

Values representing load sharing among the trusses were obtained from the numerical model for the pressure associated with maximum global uplift loads for a variety of wind speeds. Because of the higher degree of stiffness of the gable end trusses relative to the middle trusses and the greater windward pressure intensity, the load share of end gable truss T1 is greater than that of the other trusses, even end gable truss T16. At the failure speed of 45 m/sec, trusses T2 to T8 reach their maximum RTWC capacity at zero slopes on the load sharing curve. Analysis performed using the tributary area method under the realistic pressure produces underestimates of the load shares of the gable end trusses because this method does not include consideration of the stiffness of the trusses. On the

other hand, to sustain the equilibrium of the global uplift loads, the tributary area method produces overestimates of the load shares in the middle trusses.

Values obtained based on the code pressure reveal similar load sharing from the maximum global uplift wind load when finite element analysis is applied. However, a comparison of the load sharing results provided by finite element analysis solved for the maximum global uplift loads and those resulting from the tributary area method analysis solved for the code pressure shows good agreement, with the exception of the results for the gable end truss on the windward side. The load sharing of both end gable trusses calculated using the tributary area method under the code pressure is 14 %, while finite element modelling produces a 29 % load share under code pressure. Because the uniform load does not represent the spatial variations that characterize the true pressure situation, it was applied in the model only for an evaluation of the effect of truss stiffness.

2.6   References

Chowdhury, A. G., Canino, I., Mirmiran, A., Suksawang, N., and Baheru, T. (2013), "Wind-loading effects on roof-to-wall connections of timber residential buildings", *Journal of Engineering Mechanics*, **139**(3), 386-395.

Datin, P. L., Mensah, A. F. and Prevatt, D. O. (2010), "Experimentally Determined Structural Load Paths in a 1/3-Scale Model of Light-Framed Wood, Rectangular Building", *2010 ASCE Structures Congress*, Orlando, Florida, United States, May.

Datin, P.L. and Prevatt, D.O. (2013), "Using instrumented small-scale models to study structural load paths in wood-framed buildings", *Engineering Structures*, **54**, 47-56.

Dessouki, A. A. (2010), "Analysis and retrofitting of low rise houses under wind loading", Master Thesis, University of Western Ontario, London, ON, Canada.

Doudak, G., McClure, G. and Smith, I. (2012), "Experimental evaluation of load paths in light-frame wood structure", *Journal of Structural Engineering*, **138**(2), 258-265.

FEMA (1992), *Building Performance: Hurricane Andrew in Florida, Observation, Recommendations, and Technical Guidance*, Federal Emergency Management Agency, Federal Insurance Administration, United States.

Foschi, R. O., (2000), "Modeling the Hysteretic Response of Mechanical Connections for Wood Structures", 6th World Conf. on Timber Engineering, Whistler, Canada, July.

Guha, T.K. and Kopp, G.A. (2014), "Storm duration effects on roof-to-wall-connection

failures of a residential, wood-frame, gable roof", *Journal of Wind Engineering and Industrial Aerodynamics*, **133**, 101-109.

He, M., Lam, F., and Foschi, R. O., (2001), "Modeling three-dimensional timber light-frame buildings", *Journal of Structural Engineering*, **127**(8), 901-913.

Henderson, D.J., Morrison, M.J. and Kopp, G.A. (2013), "Response of toe-nailed, roof-to-wall connections to extreme wind loads in a full-scale, timber-framed, hip roof", *Engineering Structures*, **56**, 1474-1483.

Jacklin, R. B. (2013), "Numerical and experimental analysis of retrofit system for light-framed wood structures under wind loading", Master Thesis, University of Western Ontario, London, ON, Canada.

Jacklin, R.B., El Damatty, A.A. and Dessouki, A.A. (2014), "Finite-element modeling of a light-framed wood roof structure", *Wind and Structures*, **19**(6), 603-621.

Kasal, B., Leichti, R. J., and Itani, R. Y. (1994), "Nonlinear finite-element model of complete light-frame wood structures", *Journal of Structural Engineering*, **120**(1), 100-119.

Kasal, B., Collins, M., Paevere, P. and Foliente, G. (2004), "Design models of light frame wood buildings under lateral loads", *Journal of Structural Engineering*, **130**(8), 1263-1271.

Khan, MAA. (2012), "Load-sharing of toe-nailed roof-to-wall connections under extreme wind loads in wood-frame houses", Master Thesis, University of Western Ontario, London, ON, Canada.

Kumar, N., Dayal, V. and Sarkar, P.P. (2012), "Failure of wood-framed low-rise buildings under tornado wind loads", *Engineering Structures*, **39**, 79-88.

Luszczki, G.E., Clapp, J.D., Davids, W.G. and Lopez-Anido, R. (2013), "Withdrawal capacity of plain, annular shank, and helical shank nail fasteners in spruce-pine-fir lumber", *Forest Products Journal*, **63**(5-6), 213-220.

Minghao, L., Foschi, R. O., and Lam F., (2012), "Modeling Hysteretic Behavior of Wood Shear Walls with a Protocol-Independent Nail Connection Algorithm", *Journal of Structural Engineering*, **138**(1), 99-108.

Morrison, M. J., Kopp, G. A., Gavanski, E., Miller, C., and Ashton, A.(2014), "Assessment of damage to residential construction from the tornadoes in Vaughan, Ontario, on 20 August 2009", *Canadian Journal of Civil Engineering*, **41**,550-558.

Morrison, M. J., Henderson, D. J. and Kopp, G. A. (2012), "The response of a wood-frame, gable roof to fluctuating wind loads", *Engineering Structures*, **41**, 498-509.

Morrison, M. J. and Kopp, G. A. (2011), "Performance of toe-nail connections under realistic wind loading", *Engineering Structures*, **33**, 69-76.

NBCC (2010), *User's Guide--NBC 2010*: *Structural Commentaries (Part 4 of Division B)*, Canadian Commission on Building and Fire Codes, National Research Council Canada, and Institute for Research in Construction (Canada), Ottawa,

ON, Canada.

Prevatt, D. O., van de Lindt, John W, Back, E. W., Graettinger, A. J., Pei, S., Coulbourne, W., Gupta, R., James, D., Agdas, D.,(2012), "Making the case for improved structural design: tornado outbreaks of 2011", *Leadership and Management in Engineering*, **12**(4), 254-270.

Reed, T. D., Rosowsky, D. V. and Schiff, S. D. (1997), "Uplift capacity of light-frame rafter to top plate connections", *Journal of Architectural Engineering*, **3**(4), 156-163.

Satheeskumar, N., Henderson, D.J., Ginger, J.D. and Wang, C. (2017), "Three-dimensional finite-element modeling and validation of a timber-framed house to wind loading", *Journal of Structural Engineering*, **143**(9), 04017112.

Satheeskumar, N., Henderson, D. J., Ginger, J. D., and Wang, C. H. (2017), "Finite element modelling of the structural response of roof to wall framing connections in timber-framed houses", *Engineering Structures*, **134**, 25-36.

Satheeskumar, N., Henderson, D.J., Ginger, J.D., Humphreys, M.T. and Wang, C.H. (2016), "Load sharing and structural response of roof–wall system in a timber-framed house", *Engineering Structures*, **122**, 310-322.

Shivarudrappa, R. and Nielson, B. G. (2013), "Sensitivity of load distribution in light-framed wood roof systems due to typical modeling parameters", *Journal of Performance of Constructed Facilities*, **27**(3), 222-234.

Thampi, H., Dayal, V. and Sarkar, P. P. (2011), "Finite element analysis of interaction of tornados with a low-rise timber building", *Journal of Wind Engineering and Industrial Aerodynamics*, **99**(4), 369-377.

Van de Lindt, John W, Graettinger, A., Gupta, R., Skaggs, T., Pryor, S., and Fridley, K. J. (2007), "Performance of wood-frame structures during hurricane katrina", *Journal of Performance of Constructed Facilities*, **21**(2), 108-116.

Zisis, I. and Stathopoulos, T. (2012), "Wind load transfer mechanisms on a low wood building using full-scale load data", *Journal of Wind Engineering and Industrial Aerodynamics*, **104-106**, 65-75.

Chapter 3

3   Semi-Analytical Solution for a Light-Frame Wood Structure under Uplift Wind Loads

3.1   Introduction

The vast majority of North American residences are light-frame wood houses: up to 90 % in the United States alone (Dao et al., 2012). Severe hurricanes have seriously damaged significant numbers of these wood houses, making these storms some of the most costly unavoidable events. For example, in 1992, Hurricane Andrew was responsible for losses costing \$20 billion (Li and Ellingwood, 2006). It was noted in the assessment reports produced by the Federal Emergency Management Agency (FEMA) that the damage to light-frame wood houses in Florida during Hurricane Andrew was caused primarily by uplift wind pressure on the roofs (FEMA, 1992).

Uplift wind pressure causes roof rafters or trusses to detach from top plate members due to the inability of the wood connections to sustain the distribution of the tension forces created by this pressure. Jacklin et al., (2014) defined two critical wood connections involved in resisting uplift wind pressure: sheathing-to-truss connections (STTCs) and roof-to-wall connections (RTWCs). Many configurations of wood connections are possible, depending on the number and type of nails used, such as common, box, and sinker nails, all of which have differing diameters, lengths, and withdrawal capacity (NDS, 2015). Other types of connections, such as metal straps, provide higher levels of withdrawal capacity than common nails (Reed et al., 1997).

Light-frame wood houses are composed of a variety of structural members, such as trusses, sheathings, and cross members between supporting trusses. Each of these structural members performs a function in transferring the load to the supporting trusses. One of the critical links in transferring an uplift wind load from the roof to the foundation is the RTWC, so it is thus important to calculate at each RTWC the required tension forces and how the uplift wind load is distributed in order to achieve a better design. A common method used for obtaining these RTWC reactions is the tributary area method

(TAM), which is an easy way of obtaining an approximate distribution of the applied loading on a series of supporting members. This method is based on the assumption that the diaphragms between the supporting members are relatively flexible so that the loads are transferred based on the spacing between those members, an assumption that leads to an overestimation of the reactions in the middle truss connections and an underestimation of the reactions in the end trusses. An accurate estimation of the RTWC reactions can be achieved by modelling wood houses using three-dimensional (3D) finite element modelling (FEM) (Enajar et al., 2019) because FEM accounts accurately for the load sharing between the trusses as well as the nonlinear behaviour of the RTWCs.

The key component in obtaining RTWC reactions is therefore a satisfactory definition of the uplift wind load sharing among the supporting trusses. In measuring the lateral load sharing between the walls, Kasal et al., (2004) investigated the accuracy of the most common analysis approaches: the plate method, the relative stiffness method, the beam on elastic foundation method, and 3D FEM. They observed that, compared with the results for a full-scale L-shaped experimental test house, the FEM calculation entailed the lowest error percentage, followed by estimates produced by the plate and beam on elastic foundation methods, which provided reasonable agreement.

The structural load path within light-frame wood houses has been investigated experimentally under gravity, lateral, and uplift load. For example, Wolfe (1996) conducted an experimental test for a light-frame wood structure under gravity load and concluded that there was significant load sharing between the trusses. Doudak et al., (2012) performed other experiments on a full-scale wood house under gravity and lateral load in order to determine the load path through the RTWCs and wall-to-foundation connections (WTFCs). Datin et al., (2010) studied vertical load distribution within wood houses by evaluating the reactions of the RTWCs and WTFCs based on a database-assisted design (DAD) approach. The DAD approach combines wood house influence functions with the aerodynamic pressure coefficient obtained from wind tunnel test for the same shape. Datin et al., (2010) evaluated the influence functions experimentally for a small-scale house by applying concentrated uplift loads on point grids at the sheathings in order to measure the reactions of the load cells located at 11 RTWCs and at 9 WTFCs.

In contrast, other researchers have investigated the load path of light-frame wood houses numerically by conducting FEM analysis. One example was Martin (2010), who developed a numerical linear finite element model using SAP2000 commercial software in order to determine the reactions in the WTFCs. In Martin's (2010) model, the RTWCs were assumed to be pin supports, while linear springs were assigned for WTFCs to represent the stiffness of the anchor bolts and hold-down connections. Martin's (2010) plotted contours of influence functions in order to validate this numerical model through a comparison with the experimental small-scale testing under uplift wind load conducted by Datin et al., (2010).

Shivarudrappa and Nielson (2013) investigated the vertical load path in light-frame wood houses, especially with respect to uplift wind loads. For their study, they developed a 3D finite element model using ANSYS commercial software in order to model the experimental testing conducted by Datin et al., (2010). They assessed the load path by plotting influence functions for each RTWC and validated them against the Datin et al., (2010) results. They used multilinear constitutive relation models for both the RTWCs and the STTCs. Guha and Kopp (2014) created a two-dimensional (2D) numerical model based on analytical slope deflection equations in order to distinguish the effect of strong wind durations on RTWCs in light-frame wood houses. Their model analyzed the reactions that were generated for a series of RTWCs under simulated uplift wind loads. The model also had the ability to capture the load sharing behaviour of RTWCs when some failed, with the loads on the failed connections then being transferred to the remaining ones that had not failed. The results of this model were validated through experimental testing performed by Khan (2012). In Khan (2012) experiment, series of RTWCs which were connected between top plate members in the bottom with two steel beams in the top. The flexural stiffness of these steel beams was similar to half of the roof (i.e., half of the sheathing and fascia section). This setup was loaded with a simulated uplift wind load using a pressure box as well as ramp load, with tension load cells and a displacement transducer to capture the uplift capacity and displacement of the RTWCs.

In previous studies such as that by Kasal and Leichti (1992) beam models supported by linear and nonlinear springs were employed to model walls of wood houses under lateral

loads, an arrangement that achieved good agreement with both FEM analysis and the results of the experimental testing conducted by Phillips (1990). In another study, Kasal et al., (2004) produced an analytical plate model for establishing the load share for each individual shear wall, taking into account the fact that the diaphragm connecting the shear walls was composed of plate members. They achieved good agreement with the results of an experiment conducted by Paevere et al., (2003). Based on consideration of the uplift load sharing among supporting trusses as analogous to lateral load sharing within shear walls, the aim of this chapter was to derive and analyze a semi-analytical solution model with the assumption that the whole roof can be modelled as a beam with an elastic foundation. The advantage of this solution model can be summarized into these points:

a) The analysis using the semi-analytical model is approximately 25 times faster than the 3D finite element solution.
b) The effort in building the 3D finite element modelling is significantly reduced.
c) The solution model can be programmed easily to perform a reliability assessment of roof trusses subjected to uplift wind loads.

3.2 Numerical Solution Model

The thorough validation of 3D FEM results against most light-frame wood experimental findings has been well documented (Dessouki, 2010; Jacklin, 2013; Shivarudrappa and Nielson, 2013). On the other hand, an equivalent 2D analysis such as TAM fails to predict the actual behaviour of wood roofs because that method relies on the assumption that the diaphragm between the structural elements is flexible (Kasal et al., 2004). However, the numerical model used in the current study relies on the assumption that the diaphragm between the supporting trusses is not flexible to transfer the uplift wind load based on truss stiffness.

The model presented in this chapter simulates the entire roof of a light-frame wood structure as a beam with an elastic foundation. The cross section of the beam should not flexible to account for the load sharing between the trusses, and each individual truss is treated as a linear spring. The model can thus be analyzed as a statically indeterminate beam that has spring supports. The exact behaviour of this version of the structure is

dependent on the definition of the depth-to-length ratio of the cross section. Two main theories are particularly relevant for analyzing this kind of structure; the Euler-Bernoulli theory and the Timoshenko theory. The first theory assumes that the rotation due to flexure at a specific point is equal to the first derivative of the deflection at that point, and that the deformation due to flexure is dominant over shear deformation. This assumption produces accurate results if the depth-to-length ratio is relatively small. However, in opposition to that assumption, the Timoshenko theory approach includes consideration of shear deformation and is valid for all ranges of depth-to-length ratios. According to the *Wood Design Manual* (WDM, 2010) the spacing between the trusses varies from 16 in. (0.4 m) to 48 in. (1.22 m), which are considered short lengths compared to the depth of the trusses. In this situation, the Timoshenko theory therefore provides a better estimate.

As mentioned above, the trusses are treated as linear springs. The stiffness of each truss is obtained from 2D finite element analysis as the ratio of the unit load to top truss deflection. For evaluating the stiffness of the trusses, it is important to include the stiffness of the RTWC from the load-deflection curve as a linear spring because of the upward direction of the unit load. Shivarudrappa and Nielson (2013) argued that there is about a 30 % to 40 % difference in the RTWC reactions when the same amount of load is applied to light-frame wood houses but in the opposite direction, such as with uplift wind loads and gravity loads. This behaviour occurs due to differences in the tension and compression stiffness of the wood connections, so that when an uplift load is applied, and pin supports are assumed, the exact effect of the RTWC responses is not represented.

The beam model presented here was analyzed using slope deflection equations that include the effects of bending and shear deformations. The spatially uplift pressure is thus shared based on the stiffness of each individual truss. Rojas (2012) derived slope deflection Equations (3.1) to (3.3) that included shear deformation. As shown in Figure 3.1 a segment AB of continuous beam, which is subjected to load W and has a constant flexural rigidity EI. Equations (3.1) to (3.3) represent the rotational moment at supports A and B as a function of:

a)   The fixed end moments M_{FAB} and M_{FBA}.

b) The angular rotations θ_A and θ_B.

c) The relative settlement between supports A and B (Δ).

d) The shearing deformation factor ϕ, which is function of the moment of inertia I, the shear area A_S, the modulus of elasticity E and the shear modulus G.

$$M_{AB} = M_{FAB} + \frac{2EI}{(1+\phi)L}\left[(2+\phi/2)\theta_A + (1-\phi/2)\theta_B - \frac{3\Delta}{L}\right] \tag{3.1}$$

$$M_{BA} = M_{FBA} + \frac{2EI}{(1+\phi)L}\left[(1-\phi/2)\theta_A + (2+\phi/2)\theta_B - \frac{3\Delta}{L}\right] \tag{3.2}$$

$$\phi = \frac{12EI}{GA_sL^2} \tag{3.3}$$
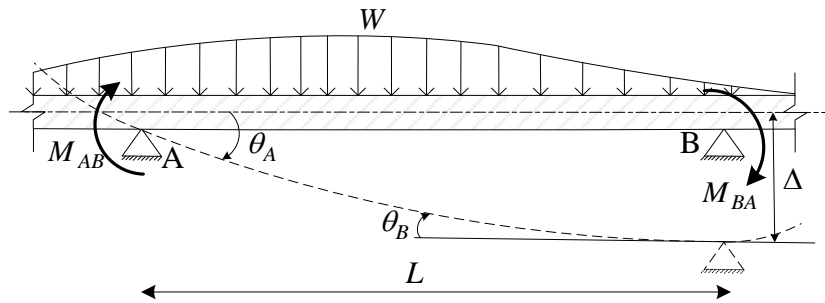
Figure 3.1: Segment of continuous beam.

As mentioned above the semi-analytical solution is based on the analysis of a statically indeterminate continuous beam that is supported by springs. The continuous beam shown in Figure 3.2 has a number of j springs, where each spring represents different truss stiffness (k_i). The number of spans is (j-1) with two cantilevers in the start and end of the beam (i.e., roof overhang). The unit of the applied beam load W is the sheathing pressure (load/area), so the unit of the reaction R_i is (load/length). For simplification overhang ends are replaced by moments M_s and M_n and shearing forces.
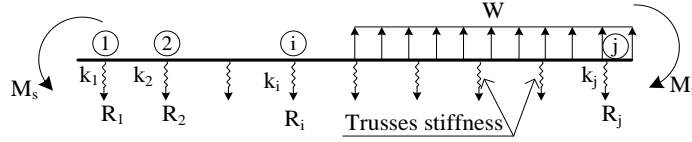
Figure 3.2: Statically indeterminate continuous beams.

Equations (3.1) and (3.2) can be rewritten for each span i, where $i = 1,2,..,(j-1)$, yielding $(j-1) \times 2$ rotational moments equations:

$$M_{i,i+1} = M_{Fi,i+1} + \frac{2EI}{(1+\phi_{i,i+1})L_{i,i+1}}\left[(2+\phi_{i,i+1}/2)\theta_i + (1-\phi_{i,i+1}/2)\theta_{i+1} - \frac{3\Delta_{i,i+1}}{L_{i,i+1}}\right] \tag{3.4}$$

$$M_{i+1,i} = M_{Fi+1,i} + \frac{2EI}{(1+\phi_{i,i+1})L_{i,i+1}}\left[(1-\phi_{i,i+1}/2)\theta_i + (2+\phi_{i,i+1}/2)\theta_{i+1} - \frac{3\Delta_{i,i+1}}{L_{i,i+1}}\right] \tag{3.5}$$

The settlement at each span is calculated as the difference between displacements at each spring as shown in Equation (3.6). The displacement at each spring is found to be the spring reaction to the spring constant:

$$\Delta_{i,i+1} = \frac{R_{i+1}}{k_{i+1}} - \frac{R_i}{k_i} \tag{3.6}$$

Substituting Equation (3.6) into Equations (3.4) and (3.5)

$$M_{i,i+1} = M_{Fi,i+1} + \frac{2EI}{(1+\phi_{i,i+1})L_{i,i+1}}\left[(2+\phi_{i,i+1}/2)\theta_i + (1-\phi_{i,i+1}/2)\theta_{i+1} - \frac{3}{L_{i,i+1}}\left(\frac{R_{i+1}}{k_{i+1}} - \frac{R_i}{k_i}\right)\right] \tag{3.7}$$

$$M_{i+1,i} = M_{Fi+1,i} + \frac{2EI}{(1+\phi_{i,i+1})L_{i,i+1}}\left[(1-\phi_{i,i+1}/2)\theta_i + (2+\phi_{i,i+1}/2)\theta_{i+1} - \frac{3}{L_{i,i+1}}\left(\frac{R_{i+1}}{k_{i+1}} - \frac{R_i}{k_i}\right)\right] \tag{3.8}$$

Equations (3.7) and (3.8) represent the relation between the moments at each span of the beam with the angular displacements and spring reactions. Therefore, equilibrium equations and shearing equations are required to obtain the spring reactions. The number of equilibrium equations and shearing equations is similar to the number of springs supports j:

Equilibrium equations

$$M_{1,2} + M_s = 0 \tag{3.9}$$

$$M_{i+1,i} + M_{i+1,i+2} = 0 \quad \text{for } i = 1,2,...,(j-2) \tag{3.10}$$

$$M_{j,j-1} - M_n = 0 \tag{3.11}$$

Shearing equations where R_T is the tributary area load applied to each truss

$$R_1 = -\frac{\left(M_{1,2} + M_{2,1} + M_s\right)}{L_{1,2}} + R_{T1} \tag{3.12}$$

$$R_{i+1} = \frac{\left(M_{i,i+1} + M_{i+1,i}\right)}{L_{i,i+1}} - \frac{\left(M_{i+1,i+2} + M_{i+2,i+1}\right)}{L_{i+1,i+2}} + R_{Ti+1} \quad \text{for } i = 1,2,...,(j-2) \tag{3.13}$$

$$R_j = \frac{\left(M_{j-1,j} + M_{j,j-1} - M_n\right)}{L_{j-1,j}} + R_{Tj} \tag{3.14}$$

The equilibrium equations and shearing equations can be simplified into matrices form as shown in Equations (3.15) and (3.16) respectively where:

$\{0\}_{j\times1}$: Zero vector

$\{R\}_{j\times1}$: Spring reaction vector

$\{\theta\}_{j\times1}$: Angular displacements vector

$\{Mf_1\}_{j\times1}, \{Mf_2\}_{j\times1}$: Fixed end moment vectors

$\{R_T\}_{j\times1}$: Tributary area reactions

$[F_{\theta1}]_{j\times j}, [F_{\theta2}]_{j\times j}$: Coefficients matrices of angular rotations

$[F_{r1}]_{j\times j}, [F_{r2}]_{j\times j}$: Coefficients matrices of spring reactions

$$\{0\}_{j\times1} = \{Mf_1\}_{j\times1} + [F_{\theta1}]_{j\times j} \times \{\theta\}_{j\times1} + [F_{r1}]_{j\times j} \times \{R\}_{j\times1} \tag{3.15}$$

$$\{R\}_{j\times1} = \{Mf_2\}_{j\times1} + [F_{\theta2}]_{j\times j} \times \{\theta\}_{j\times1} + [F_{r2}]_{j\times j} \times \{R\}_{j\times1} + \{R_T\}_{j\times1} \tag{3.16}$$

The parameters which are used in the Equations (3.15) and (3.16) can be written in details as the flowing equations:

$$Mf_1 = \begin{Bmatrix} Mf_{1,2} + M_s \\ Mf_{2,1} + Mf_{2,3} \\ \vdots \\ \vdots \\ Mf_{j-1,j-2} + Mf_{j-1,j} \\ Mf_{j,j-1} - M_n \end{Bmatrix}_{j\times1} \tag{3.17}$$

$$Mf_2 = \begin{Bmatrix} -\dfrac{\left(Mf_{1,2} + Mf_{2,1}\right)}{L_{1,2}} \\ \dfrac{\left(Mf_{1,2} + Mf_{2,1}\right)}{L_{1,2}} - \dfrac{\left(Mf_{2,3} + Mf_{3,2}\right)}{L_{2,3}} \\ \vdots \\ \dfrac{\left(Mf_{j-2,j-1} + Mf_{j-1,j-2}\right)}{L_{j-2,j-1}} - \dfrac{\left(Mf_{j-1,j} + Mf_{j,j-1}\right)}{L_{j-1,j}} \\ \dfrac{\left(Mf_{j-1,j} + Mf_{j,j-1}\right)}{L_{j-1,j}} \end{Bmatrix}_{j\times1} \tag{3.18}$$

$$R_T = \begin{Bmatrix} R_{T1} \\ R_{T2} \\ \vdots \\ \vdots \\ R_{Tj-1} \\ R_{Tj} \end{Bmatrix}_{j\times1} \tag{3.19}$$

$$\phi_{i,i+1} = \frac{12EI}{GA_S L_{i,i+1}^2}$$

Let $\phi n_{i,i+1} = 2 + \dfrac{\phi_{i,i+1}}{2}$ and $\phi m_{i,i+1} = 1 - \dfrac{\phi_{i,i+1}}{2}$

By identifying $\phi_{i,i+1}, \phi n_{i,i+1}, \phi m_{i,i+1}$, other parameters can be written as followings:

$$\alpha_{i,i+1} = \frac{2\phi n_{i,i+1}}{(1+\phi_{i,i+1})L_{i,i+1}} \qquad \beta_{i,i+1} = \frac{2\phi m_{i,i+1}}{(1+\phi_{i,i+1})L_{i,i+1}} \qquad \delta_{i,i+1} = \frac{6}{(1+\phi_{i,i+1})L_{i,i+1}^2}$$

$$\mu_{i,i+1} = \frac{6}{(1+\phi_{i,i+1})L_{i,i+1}^3} \qquad \gamma_{i,i+1} = \frac{2\phi n_{i,i+1}}{(1+\phi_{i,i+1})L_{i,i+1}^2} + \frac{2\phi m_{i,i+1}}{(1+\phi_{i,i+1})L_{i,i+1}^2}$$

$$F_{\theta 1} = EI \begin{bmatrix} \alpha_{1,2} & \beta_{1,2} & 0 & \cdots & \cdots & \cdots & 0 \\ \beta_{1,2} & \alpha_{1,2}+\alpha_{2,3} & \beta_{2,3} & 0 & \cdots & \cdots & 0 \\ 0 & \ddots & \ddots & \ddots & 0 & \cdots & 0 \\ 0 & \cdots & \cdots & 0 & \beta_{j-2,j-1} & \alpha_{j-2,j-1}+\alpha_{j-1,j} & \beta_{j-1,j} \\ 0 & \cdots & \cdots & \cdots & 0 & \beta_{j-1,j} & \alpha_{j-1,j} \end{bmatrix}_{j\times j} \qquad (3.20)$$

$$F_{\theta 2} = EI \begin{bmatrix} -\gamma_{1,2} & -\gamma_{1,2} & 0 & \cdots & \cdots & \cdots & 0 \\ \gamma_{1,2} & \gamma_{1,2}-\gamma_{2,3} & -\gamma_{2,3} & 0 & \cdots & \cdots & 0 \\ 0 & \ddots & \ddots & \ddots & 0 & \cdots & 0 \\ 0 & \cdots & \cdots & 0 & \gamma_{j-2,j-1} & \gamma_{j-2,j-1}-\gamma_{j-1,j} & -\gamma_{j-1,j} \\ 0 & \cdots & \cdots & \cdots & 0 & \gamma_{j-1,j} & \gamma_{j-1,j} \end{bmatrix}_{j\times j} \qquad (3.21)$$

$$F_{r1} = EI \begin{bmatrix} \dfrac{\delta_{1,2}}{K_1} & -\dfrac{\delta_{1,2}}{K_2} & 0 & \cdots & \cdots & \cdots & 0 \\[2mm] \dfrac{\delta_{1,2}}{K_1} & \dfrac{\delta_{2,3}}{K_2}-\dfrac{\delta_{1,2}}{K_2} & -\dfrac{\delta_{2,3}}{K_3} & 0 & \cdots & \cdots & 0 \\[2mm] 0 & \ddots & \ddots & \ddots & 0 & \cdots & 0 \\[2mm] 0 & \cdots & \cdots & 0 & \dfrac{\delta_{j-2,j-1}}{K_{j-2}} & \dfrac{\delta_{j-1,j}}{K_{j-1}}-\dfrac{\delta_{j-2,j-1}}{K_{j-1}} & -\dfrac{\delta_{j-1,j}}{K_j} \\[2mm] 0 & \cdots & \cdots & \cdots & 0 & \dfrac{\delta_{j-1,j}}{K_{j-1}} & -\dfrac{\delta_{j-1,j}}{K_j} \end{bmatrix}_{j\times j} \qquad (3.22)$$

$$F_{r2} = 2EI \begin{bmatrix} -\dfrac{\mu_{1,2}}{K_1} & \dfrac{\mu_{1,2}}{K_2} & 0 & \cdots & \cdots & \cdots & 0 \\[2mm] \dfrac{\mu_{1,2}}{K_1} & -\dfrac{\mu_{2,3}}{K_2}-\dfrac{\mu_{1,2}}{K_2} & \dfrac{\mu_{2,3}}{K_3} & 0 & \cdots & \cdots & 0 \\[2mm] 0 & \ddots & \ddots & \ddots & 0 & \cdots & 0 \\[2mm] 0 & \cdots & \cdots & 0 & \dfrac{\mu_{j-2,j-1}}{K_{j-2}} & -\dfrac{\mu_{j-1,j}}{K_{j-1}}-\dfrac{\mu_{j-2,j-1}}{K_{j-1}} & \dfrac{\mu_{j-1,j}}{K_j} \\[2mm] 0 & \cdots & \cdots & \cdots & 0 & \dfrac{\mu_{j-1,j}}{K_{j-1}} & -\dfrac{\mu_{j-1,j}}{K_j} \end{bmatrix}_{j\times j} \qquad (3.23)$$

Equations (3.15) and (3.16) have two unknown vectors which are the spring reaction vector $[R]_{j\times 1}$ and the angular rotations vector $[\theta]_{j\times 1}$ .By solving these two equations the solution will be written as:

Let $\{A\}_{j\times 1} = \left[[I]_{j\times j} - [F_{r2}]_{j\times j} \right]^{-1} \times \left\{ \{R_T\}_{j\times 1} + \{Mf_2\}_{j\times 1} \right\}$ $\qquad$ (3.24)

Where $[I]_{j\times j}$ is the unit matrix

Let $[B]_{j\times j} = \left[[I]_{j\times j} - [F_{r2}]_{j\times j} \right]^{-1} \times [F\theta_2]_{j\times j}$ $\qquad$ (3.25)

$\{\theta\}_{j\times 1} = \left[[F\theta_1]_{j\times j} - [F_{r1}]_{j\times j} \times [B]_{j\times j} \right]^{-1} \times \left\{ - \{MF_1\}_{j\times 1} - [F_{r1}]_{j\times 1} \times \{A\}_{j\times 1} \right\}$ $\qquad$ (3.26)

$\{R\}_{j\times 1} = \{A\}_{j\times 1} + [B]_{j\times j} \times \{\theta\}_{j\times 1}$ $\qquad$ (3.27)

3.3 Methodology

The objective of this chapter was to develop and run a semi-analytical solution model built on the assumption that the whole roof can be modelled as a beam with an elastic foundation. In other words, the beam cross section is represented by the cross members between the trusses, the fascia, and the sheathing, all lumped together with the assumption that the spacing between the trusses is small compared with the truss's depth. Figure 3.3 and 3.4 illustrate an example of the determination of RTWCs reactions. For this example, a flowchart is drawn to show the required linear and nonlinear steps which are used throughout this chapter as shown in Figure 3.5. For the example shown in Figure 3.3, a gable roof house has $j = 9$ number of trusses and is loaded with six uniformly distributed pressures (i.e., W_1 to W_6 load per unit area) on top of the roof. The following steps can be used to determine the distribution of these loads linearly to each individual truss, and then obtaining the corresponding RTWCs reactions.

(a) Gable roof structure

(b) Plan view of the roof with wind uplift pressure
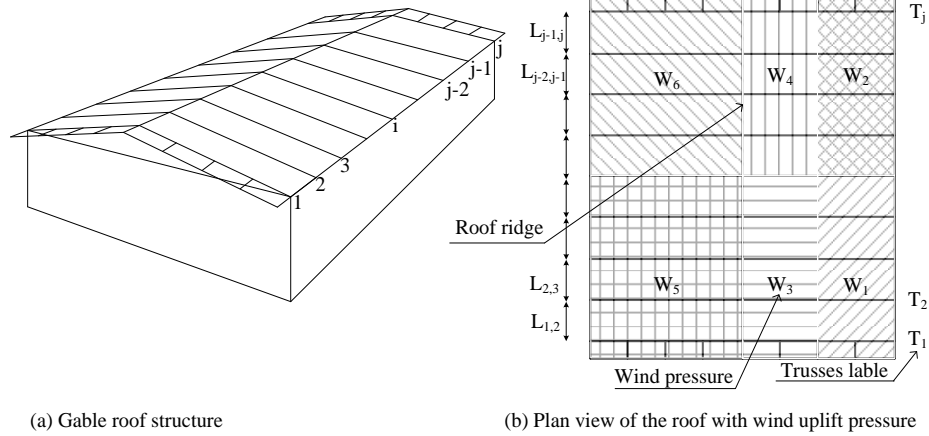
Figure 3.3: Example of a light-frame wood structure with a set of uplift wind loads.

(a) Beams on elastic foundation

(b) Load shared to each truss
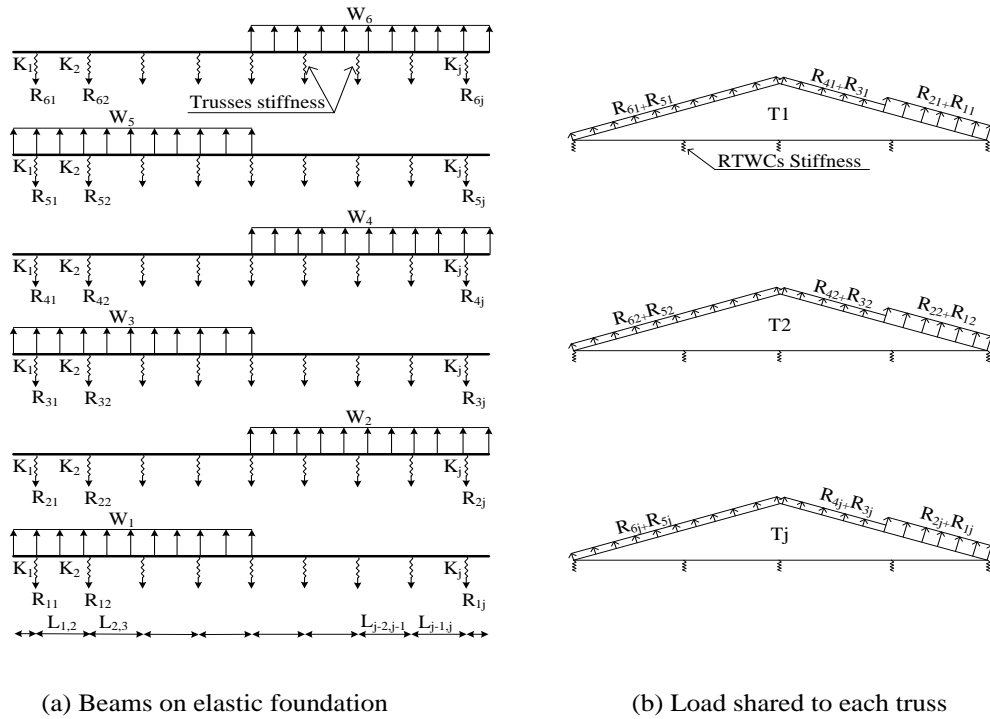
Figure 3.4: Load distribution to RTWCs by the use of beams on elastic foundation for the example of Figure 3.3.
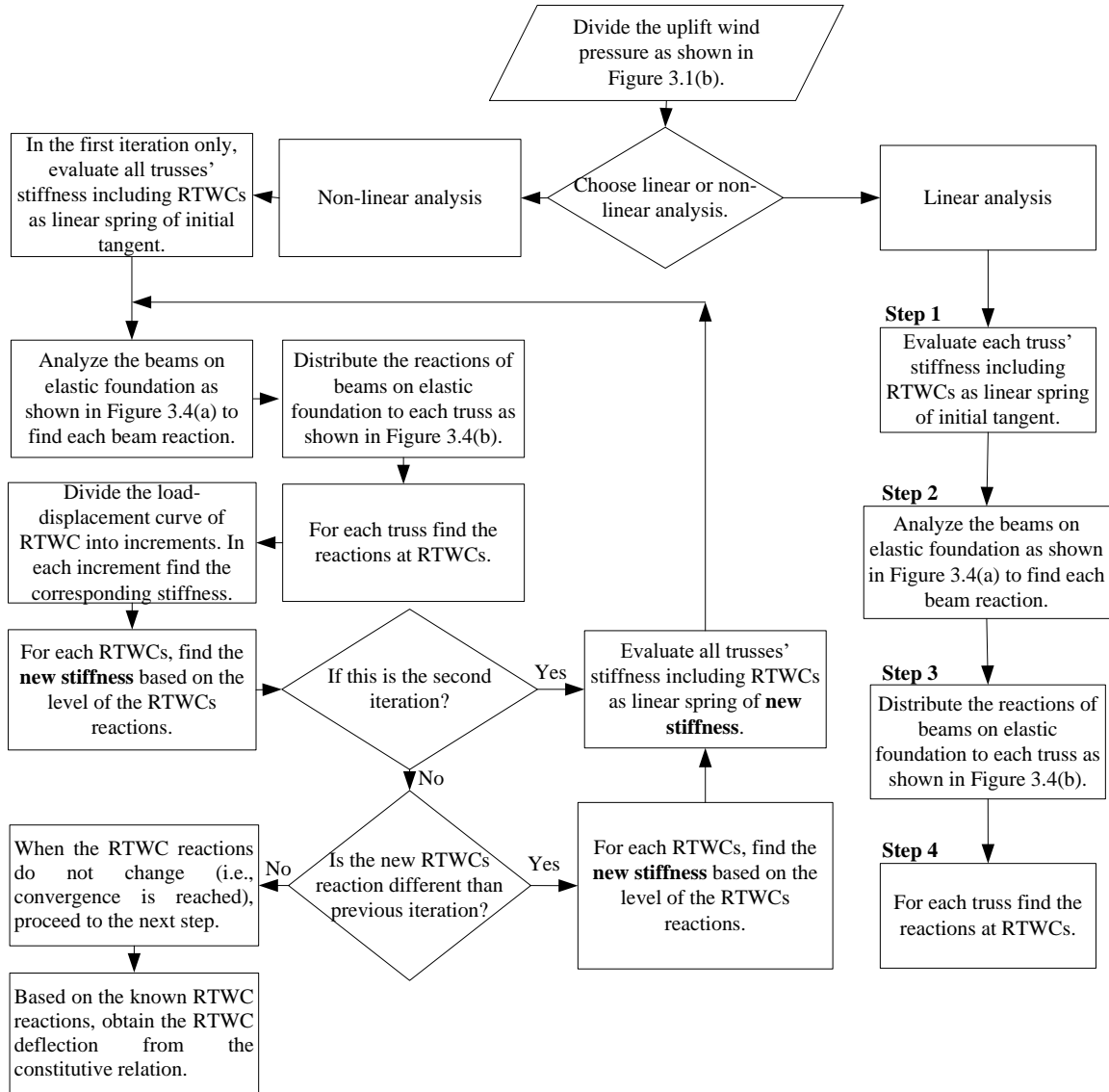
Figure 3.5: Flowchart for determination of RTWCs reaction and corresponding deflection.

Step 1. Evaluate the stiffness of each individual truss as the ratio of the unit load to top truss deflection as K_i through 2D finite element model. Each RTWC is also designated a linear spring of initial tangent stiffness.

Step 2. Analyze the beams on elastic foundation shown in Figure 3.4a in order to evaluate each beam reactions by using the solution model as followings. Noting that, each beam represents one uplift pressure.

a) Evaluate the fixed end moment vector matrices Mf_1, Mf_2 (i.e., Equations 3.17 and 3.18) under the effect of pressure W_1, where $Mf_{1,2}$ is the fixed end moment between truss 1 and truss 2; M_s, M_n are the moments at the overhang ends at the south and north sides, respectively; $L_{1,2}$ is the horizontal distance between truss 1 and truss 2; and $i = 1, 2, ..., (j-1)$.

b) Evaluate the tributary area reaction vector R_T (i.e., Equation 3.19) under the effect of pressure W_1, where R_{T1} is the tributary area load applied to truss 1.

c) For each subsequent section between the trusses, as shown in Figure 3.6, find the moment of inertia I, the shear area A_S, the modulus of elasticity E, and the shear modulus G. Evaluate the parameters: ϕ, ϕ_n, ϕ_m, α, β, γ, δ, and μ. Next, find the four matrices $F_{\theta 1}$, $F_{\theta 2}$, F_{r1}, and F_{r2}.
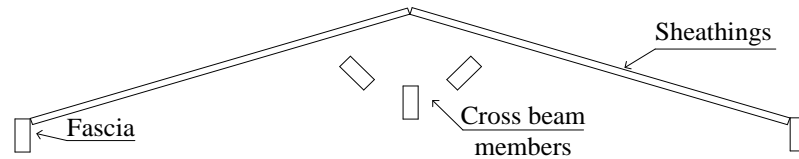
Figure 3.6: Cross section of a beam on an elastic foundation.

d) Solve Equations (3.24) to (3.27) in order to obtain the loads distributed to each truss under the effect of pressure W_1 (i.e., R_{11} to R_{19} in Figure 3.4a). These loads represent the individual share of pressure W_1 for all trusses, and the loads are applied to each truss in the same W_1 width area as shown in Figure 3.4b. The analysis is then applied for the remaining pressures (i.e., W_2 to W_6).

Step 3. Distribute all beams' reactions to each truss as illustrated in Figure 3.4b. Therefore, each truss extracts the load sharing from all applied loads (i.e., W_1 to W_6).

Step 4. For each truss, evaluate the reactions at the location of the RTWCs which is modeled as a linear spring.

The nonlinear analysis has similar steps comparing to the linear analysis, but it incorporates a different stiffness of the RTWCs. The nonlinear analysis can be performed in number of iterations until the analysis reaches convergence by dividing the load-deflection curve of RTWC into number of increments. In the first iteration, the analysis is performed with the initial tangent stiffness of each RTWC. The reactions of each RTWC from the first iteration are used in the second iteration in order to evaluate the corresponding new stiffness of RTWCs from the load-deflection curve. Based on this new stiffness of RTWCs, a new truss stiffness is evaluated. The load sharing of each truss is, in turn, calculated with the use of the solution model in order to evaluate the reactions of all RTWCs in the second iteration. These iterations are repeated until there is no change in the reactions of all RTWCs.

3.4 Validation of the Numerical Model

3.4.1 Reaction of RTWCs using Linear Analysis

The semi-analytical solution discussed in the previous section was first used for analyzing a gable roof house under a simulated uplift wind load. Jacklin (2013) had previously analyzed this roof house with the use of FEM and had obtained results that were reasonable in comparison with the findings from experimental testing on a gable roof house conducted at the Insurance Research Lab for Better Homes (IRLBH) located at the University of Western Ontario (Morrison et al., 2012). This section presents the results of a linear comparison of the solution model and FEM results with respect to the RTWC reactions.

As shown in Figure 2.2, the plan view of the gable roof used in this comparison was approximately 9 m by 9 m with a roof pitch of 1:3. The gable roof consisted of 16 Howe trusses spaced 0.6 m apart, all having a roof overhang of 0.5 m in each direction. The middle 14 trusses (i.e., T2 to T15) were each supported by two RTWCs, one on the north side and one on the south side of the house, while the remaining trusses were gable end

trusses (i.e., T1 and T16), one each on the eastern and western sides, which were supported by walls as well as by seven RTWCs. On average, three twisted shank nails, either 12D or 16D, were used for each RTWC. The top and bottom chord sections of the trusses were 2 in. (50.8 mm) by 4 in., (101.6 mm) and the webs were 2 in. (50.8 mm) by 3 in. (76.2 mm), with four extra webs added to increase the stiffness of the end gable trusses, as shown in Figure 3.7. The thickness of the plywood sheathing used was 9 mm.

For the experimental testing, the wind load was simulated with the use of 58 pressure boxes, as illustrated in Figure 2.2. These boxes created suction pressure in order to simulate the uplift wind load. In addition, there were a number of boxes that varied in size and distribution, with each box applying temporally varying pressure intensity. The experimental test was performed in six loading stages, ranging from a wind speed of 20 m/sec up to complete failure of the roof at a wind speed of 45 m/sec. Each testing speed was allocated a time period, which decreased as the speed increased. Further details about the experimental test can be found in the thesis by Morrison et al., (2012). To conduct a numerical comparison of the solution model and FEM results, 35 m/sec was chosen for the analysis under a maximum global uplift pressure. To ensure that only the effects of the uplift wind load would be accounted for, the self-weight of the roof was not included.
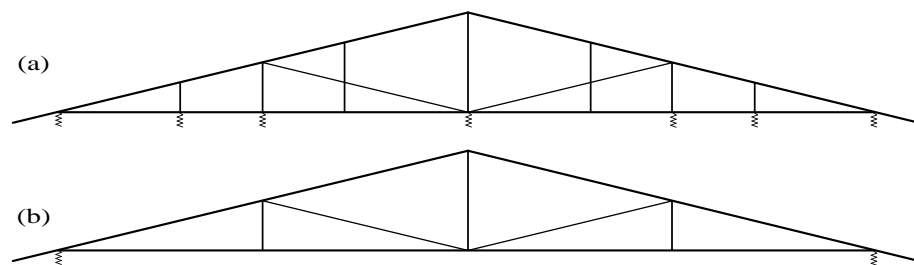
Figure 3.7: Howe trusses: (a) end gable trusses; (b) middle trusses.

For FEM analysis, Jacklin (2013) proposed a multilinear load deflection relation to account for the nonlinear behaviour of the RTWCs, as shown in Figure 2.3. This relationship was based on the nonlinear curve resulting from the experimental testing performed by Morrison and Kopp (2011). However, in the beam on elastic foundation

solution model, the stiffness of the connection was considered to be linear as the initial slope of the multilinear load deflection relation which is found to be 1642 kN/m. Each truss was modelled as a linear spring, and the stiffness of the spring was evaluated based on the ratio of the unit loads applied to the vertical deflection at the top point of the truss. The stiffness of the truss was evaluated using 2D finite element in-house coding, which modelled each truss member as a frame element with two nodes. Each node of the model represents three degrees of freedom (i.e., two translations and one rotation).

The stiffness values obtained for the trusses were 997 kN/m and 3934 kN/m for the middle trusses and end gable trusses, respectively. The flexural stiffness of the beam included in the elastic foundation model was evaluated based on Figure 3.6 as $EI=271309.2$ kN.m^2. Figure 3.8 provides a comparison of the FEM and solution model results with respect to the reaction of all RTWCs. The reactions were evaluated for a wind speed of 35 m/sec under the effects of the ultimate applied pressure during the associated time history. As shown in Figure 3.8, good agreement exists between the results for the north and south sides in terms of magnitude and trend. With reference to the FEM results for wind speeds of 35 m/sec, the maximum differences between the FEM and the solution model reaction values are 0.7 kN on north side and 0.48 kN on south side, resulting in a mean percentage difference between the FEM and the solution model output of 11 % and 10 % for the north and south sides, respectively.

Figure 3.8: FEM and solution model reaction values for all RTWCs on the north and south sides under a maximum global uplift pressure from wind speeds of 35 m/sec at time step 633.

3.4.2 Reaction of RTWC S3 using Nonlinear Analysis

Another comparison was performed between the solution model and FEM in terms of evaluating the reaction of the RTWC S3 for the gable roof house conducted at IRLBH (Figure 2.2). RTWC S3 was observed to exhibit the greatest deflection measurements (Morrison et al., 2012). Four testing wind speeds were chosen for the analysis, beginning with 30 m/sec and increasing in 5 m/sec increments up to complete roof failure at 45 m/sec. These values were chosen because these loading stages cause RTWCs to exhibit permanent withdrawal. From all of the chosen testing speeds, 20 sec periods that contained the minimum and maximum pressure intensities in the time history were selected. In this section, the self-weight of the roof was not included.

The solution model was modified to include the trilinear stiffness of the RTWCs, as shown in Figure 2.3, so that each RTWC has three slopes that are dependent on the level of the forces acting on each connection. For example, if an RTWC reaction is between zero and 2.3 kN, the stiffness of the connection is the initial tangent modulus k1; if the RTWC reaction is between 2.3 kN and 3.3 kN, the stiffness is k2; and k3 represents the

stiffness of the connection when the reaction is greater than 3.3 kN. The reason these three slopes were included in the solution model was to account for the load sharing among the connections, so that when a weak RTWC reaches failure, the extra load is transferred to the adjacent RTWCs, placing an increased demand on the RTWCs that have not yet failed. The consequence of any increases in the applied uplift load is that the remaining RTWCs become unable to sustain that augmented uplift load, resulting in additional failures.

The solution model presented in this chapter simulated a light-frame wood roof as a beam on an elastic foundation, with each truss being treated as a linear spring. Using the trilinear stiffness of the RTWCs, the model was developed to represent a beam on an inelastic foundation. The stiffness of each truss was evaluated using 2D in-house finite element coding based on the ratio of the unit load to the top truss deflection, with the stiffness of the RTWCs being included in the in-house code. Middle trusses have two RTWCs: one on the north side and the other on the south side, with each RTWC having three possible springs. Based on the level of the forces, each middle truss thus has 9 possible truss stiffness values. Both end gable trusses have seven RTWCs; therefore, regarding the number of connections and the trilinear stiffness of the RTWCs, there are 2187 possible end gable truss stiffness values.

Figures 3.9 to 3.12 illustrate the reaction values for RTWC S3 through the time history associated with pressure from four wind speeds ranging from 30 m/sec up to 45 m/sec. RTWC S3 was selected because it exhibited the greatest deflection measurements (Morrison et al., 2012). As shown in Figures 3.9 to 3.12, good agreement is indicated between the FEM and the solution model reactions with respect to the magnitude and shape of the curves. However, the average differences between the RTWC S3 reactions indicated in the FEM results and those produced by the solution model are 0.092 kN, 0.12 kN, 0.21 kN, and 0.43 kN, resulting in a mean percentage difference between the FEM and the solution model of 8 %, 9 %, 17 % and 31 %, under pressure of wind speeds of 30 m/sec, 35 m/sec, 40 m/sec, and 45 m/sec, respectively. The difference increases with greater wind speed, due to the approximation of solution model analysis. The complete failure of the roof was observed experimentally at the wind speed of 45 m/sec. The

solution model tends to overestimate the FEM at the failure speed, which will lead to the same results anyway.
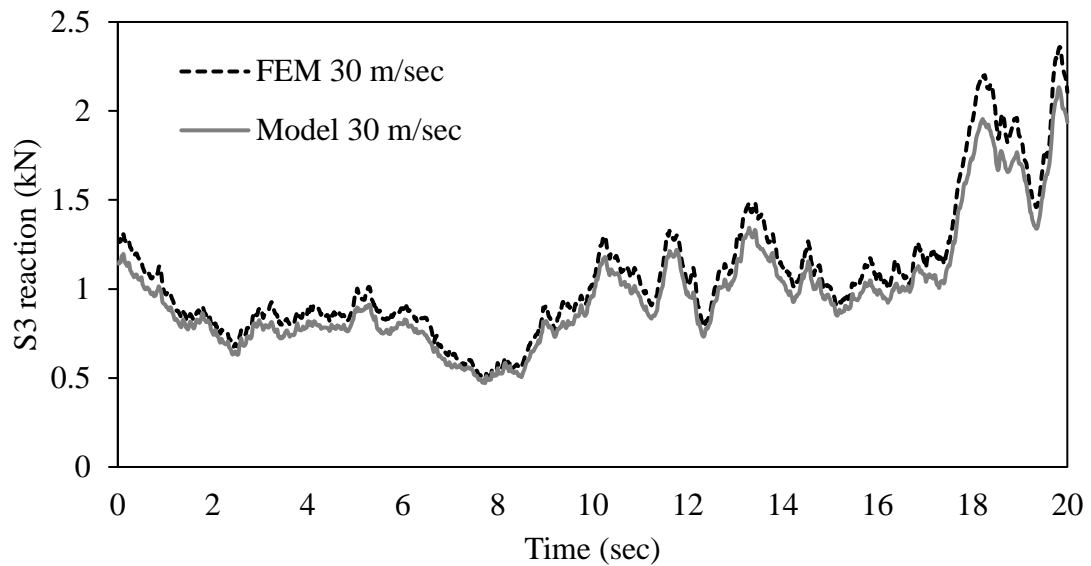
Figure 3.9: FEM and solution model reaction values for RTWC S3 during the time history for wind speeds of 30 m/sec.
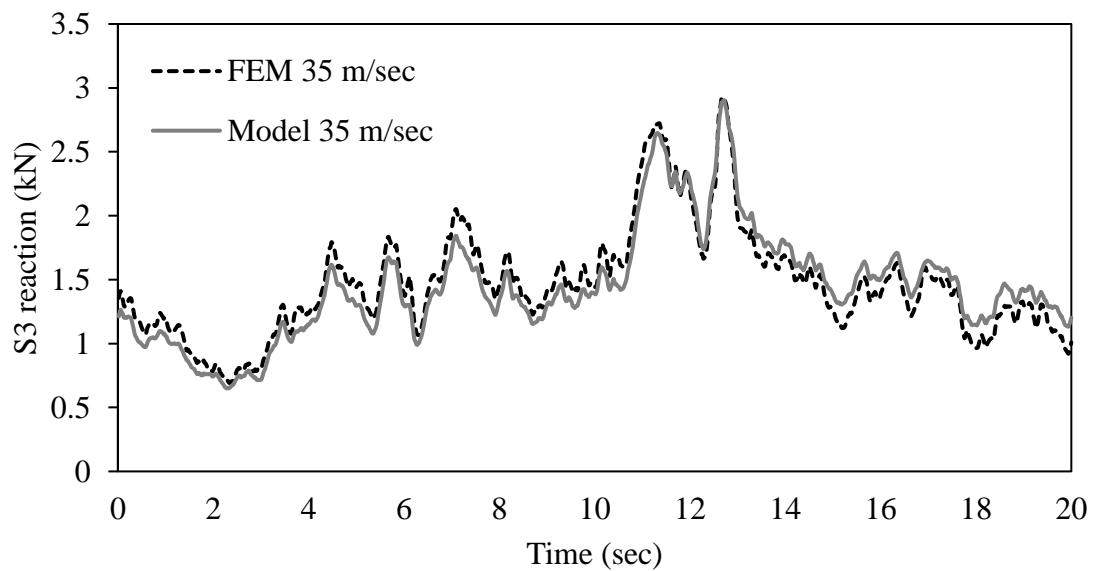
Figure 3.10: FEM and solution model reaction values for RTWC S3 during the time history for wind speeds of 35 m/sec.
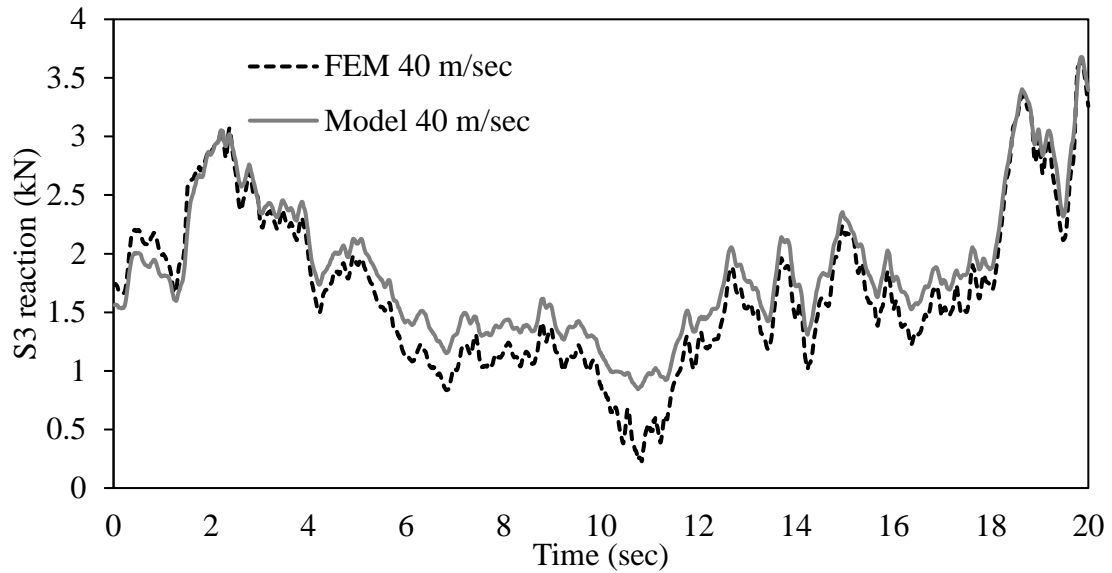
Figure 3.11: FEM and solution model reaction values for RTWC S3 during the time history for wind speeds of 40 m/sec.
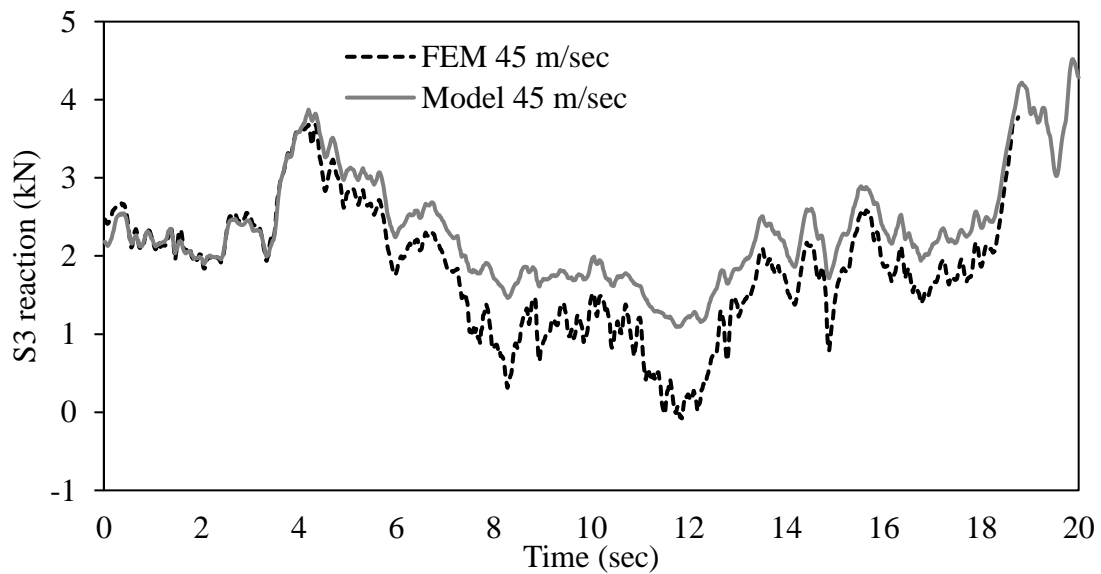
Figure 3.12: FEM and solution model reaction values for RTWC S3 during the time history for wind speeds of 45 m/sec.

3.4.3 Deflection of RTWCs using Nonlinear Analysis

To evaluate the performance of the modelled solution against the results of the experimental testing conducted by Morrison et al., (2012) at (IRLBH), the predicted RTWC deflections were compared with the experimental findings. The realistic pressure applied in the experimental testing was used for analyzing the modelled solution, beginning with pressure from a speed of 30 m/sec and increasing in 5 m/sec increments up to complete roof failure at 45 m/sec. These wind speed ranges were investigated because permanent withdrawal of RTWCs occurs within them. The pressure applied on the roof of the house was varied both spatially and temporally, so that the 58 pressure boxes created a different intensity at each time step (Figure 2.2). The solution model was run with 20 sec intervals divided into 1000 time steps that included the maximum and minimum uplift wind load. During this stage of the validation, and to simulate the exact behaviour of the case study, the self-weight of the roof was included in the analysis.

The solution model analysis was performed based on the developed in-house coding that generated all four speeds selected for the experimental testing: 30 m/sec, 35 m/sec, 40 m/sec, and 45 m/sec. Each speed included 58 pressure boxes with 1000 time steps for each box. For example, at the first time step of the 30 m/sec wind speed, the solution model was run 58 times for each pressure box, using the initial tangent slope of each RTWC. After time step 1 has been analyzed, the stiffness of each truss is recalculated based on the level of forces observed to be acting on each RTWC. The new truss stiffness values are reused for analyzing a number of iterations for time step 1 until the analysis reaches convergence with respect to the RTWC reactions (i.e., no change in the results). The code then starts the analysis of the remaining steps until 1000 time steps have been performed. In the final step, when all of the reactions of all of the RTWCs have been evaluated, the deflection predicted for each RTWC can be evaluated by substituting it into the constitutive relation depicted by the curve shown in Figure 2.3.

Morrison et al., (2012) observed that RTWCs exhibited permanent withdrawal when the connections reached peak load. Because a complete time history analysis was not performed, the current analysis was based on the assumption of an initial zero withdrawal in the first time step and did not take into account any previous withdrawal. To enable the

deflection values predicted by the solution model to be compared with the experimental results, both the predicted deflections and the experimental results should match at the first time step. This correspondence can be achieved through an approximated assumption for modifying the solution model output by taking the differences between the experimental results and the solution model predictions at each RTWC for the first time step and then adding these differences to all time steps. This approximation provides a reasonable prediction since the analysis is based on neglecting any previous plastic damage that occurred at the earlier peaks in the pressure time history.

Figures 3.13 to 3.17 provide a comparison of the experimental results and the solution model predictions with respect to the deflection of all RTWCs. The deflections were evaluated under the effects of the ultimate pressure applied during the associated time history for four wind speeds: 30 m/sec, 35 m/sec, 40 m/sec, and 45 m/sec. As shown in Figures 3.13 and 3.14, good agreement exists between the experimental and predicted deflections for the north and south sides in terms of trend and magnitude. With reference to the model deflections, the average percentages of difference between the experimental deflections and the predicted deflections for wind speeds of 30 m/sec and 35 m/sec on the north side reached 12 % and 11 %, respectively, while on the south side, they reached 9 % and 6 %, respectively.

When the applied pressures associated with the greater wind speeds of 40 m/sec and 45 m/sec were examined, the differences between the predicted model deflections and the experimental deflections were higher as well, mainly for the south side RTWCs, as shown in Figures 3.15 and 3.16. These differences occurred primarily because the solution model analysis did not include the full time history but was targeted only at the maximum and minimum uplift pressure values. Another factor in these differences is that the solution produced by the model was based on the use of a similar constitutive relation for all RTWCs, which does not represent actual conditions, especially for toe-nailed connections. As mentioned by Reed et al., (1997), test results for individual toe-nail connections revealed that the coefficient of variation for the ultimate uplift capacity can be up to 25 %. The differences also indicate the occurrence of RTWC failure. On the other hand, however, there was good agreement between the experimental results and the

solution model predictions with respect to the north side connections at higher speeds, with reference to the model deflections, the average percentages of differences being 17 % and 14 % for wind speeds of 40 m/sec and 45 m/sec, respectively.
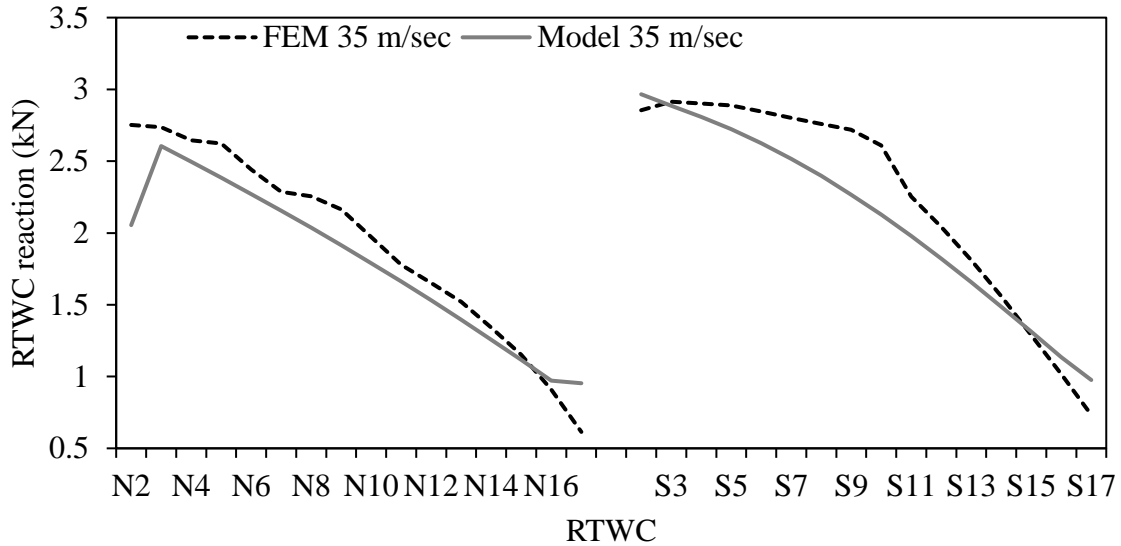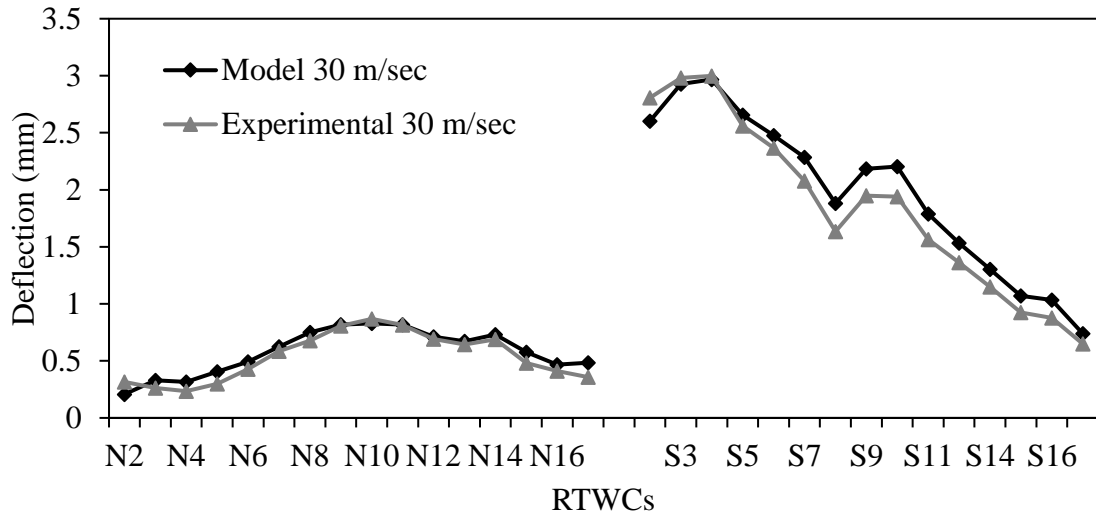

Figure 3.13: Experimental and solution model deflection values for all RTWCs on the north and south sides under maximum global uplift pressure from a 30 m/sec wind speed at time step 900.
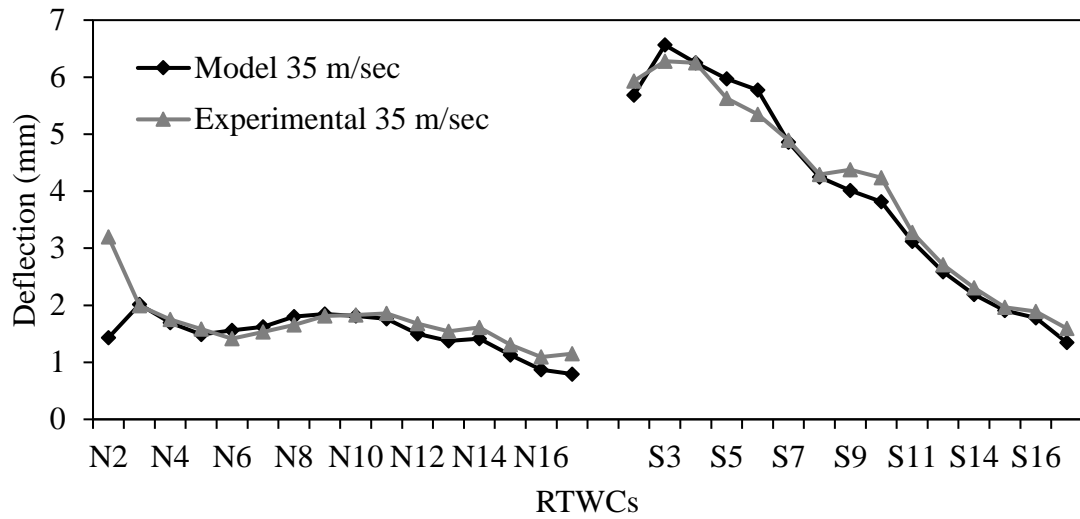
Figure 3.14: Experimental and solution model deflection values for all RTWCs on the north and south sides under maximum global uplift pressure from a 35 m/sec wind speed at time step 633.
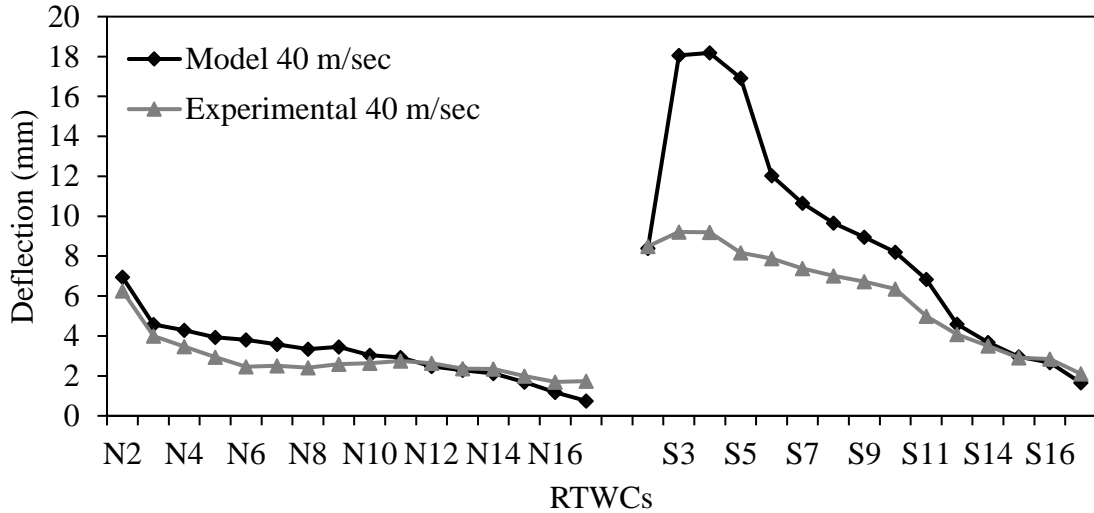
Figure 3.15: Experimental and solution model deflection values for all RTWCs on the north and south sides under maximum global uplift pressure from a 40 m/sec wind speed at time step 991.
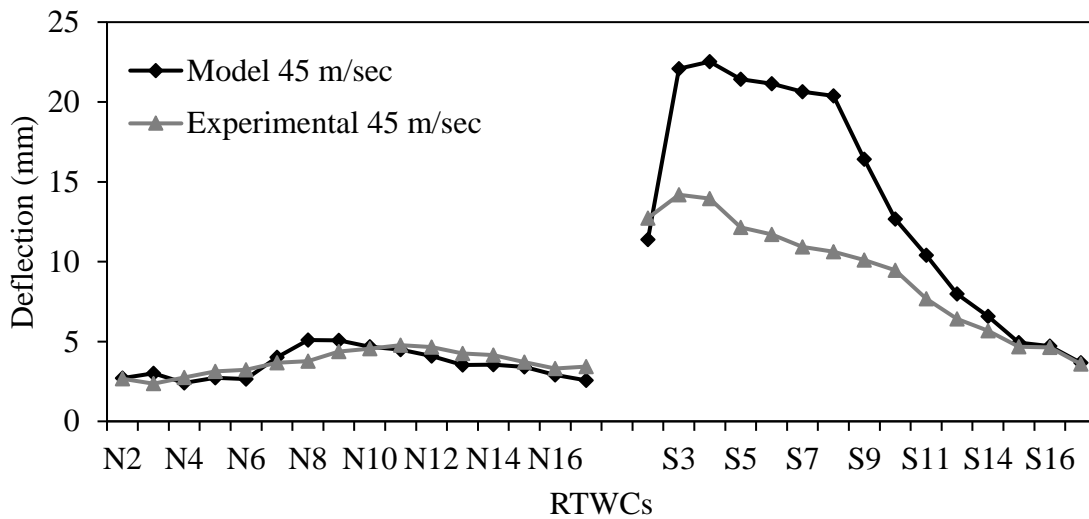
Figure 3.16: Experimental and solution model deflection values for all RTWCs on the north and south sides under maximum global uplift pressure from a 45 m/sec wind speed at time step 210.

3.5 Load Sharing among Trusses

After the solution model predictions have been validated against the experimental results in terms of RTWC deflections, the load sharing between the trusses can be obtained in order to compare the solution model results with those produced using the common methods of analyzing light-frame wood houses: the simple 2D tributary area method (TAM) and the 3D finite element modelling (FEM). Defined as the ratio of the support reactions of each individual truss to the total uplift load, load sharing is used as a means of determining how the uplift load is transferred among the trusses. The realistic uplift wind pressure used in this comparison was derived from the experimental testing conducted by Morrison et al., (2012). In this current study, the self-weight of the roof is neglected in order to enable the investigation of the effects of uplift wind load alone. The solution model analysis is also based on the use of trilinear RTWC stiffness values.

Table 3.1 lists the percentages of the load sharing for both end gable trusses T1 and T16 and for middle truss T4 under ultimate uplift pressure for wind speeds ranging from 30 m/sec to 45 m/sec. As shown in Table 3.1, there is good agreement between the solution

model and 3D FEM results, with a maximum difference of 1.8 % at end gable truss T1. Due to the high degree of stiffness in the end gable trusses compared with that in the middle trusses, trusses T1 and T16 extracted a greater share of the load. However, end gable truss T16 extracted a smaller load share than truss T1 due to the high intensity of the pressure applied close to truss T1. This pressure then decreases gradually towards truss T16. It is clear from Table 3.1 that the use of TAM analysis for determining load sharing results in an underestimation of the load sharing for the end gable trusses and an overestimation of the load sharing for the middle trusses, an effect attributed to the fact that differences in truss stiffness are not taken into consideration and that the load distribution is based on the position of the pressure on the nearest truss.

Table 3.1: Percentage of load sharing among the trusses at the maximum applied pressure

Speed	30 m/sec			35 m/sec		
Truss	T1 %	T4 %	T16 %	T1 %	T4 %	T16 %
TAM	14.7	8.2	4.4	16.4	8.5	4.0
FEM	22.5	6.3	7.4	23.4	6.5	5.7
Model	24.1	6.0	9.3	23.2	6.3	5.6
Speed	40 m/sec			45 m/sec		
Truss	T1 %	T4 %	T16 %	T1 %	T4 %	T16 %
TAM	16.6	8.4	4.1	11.2	7.4	5.4
FEM	23.2	6.4	4.2	19.5	5.5	9.5
Model	21.4	6.5	4.0	19.0	5.7	10.4

Figure 3.17 shows the percentages of the load sharing for all trusses at the time step associated with the ultimate pressure produced by the 35 m/sec wind speed. As depicted in Figure 3.17, the maximum load sharing difference of 0.43 % indicates a good match between the results obtained from the solution model and those produced using FEM, which is considered the most reliable tool for modelling light-frame wood structures. In contrast, the TAM analysis led to an underestimation for the end gable truss reactions, as discussed above. Figures 3.18 and 3.19 provide a comparison of the load sharing based on FEM analysis and the results produced by the solution model for end gable truss T1 and middle truss T4 for the entire 40 m/sec time history. As shown in Figure 3.18,

compared to the FEM analysis, the solution model effectively estimated the load sharing, with an average difference of 2 %. A comparison of the TAM and solution model results throughout the full time history reveals that TAM analysis failed to predict the load sharing due to the assumption inherent in that method that the diaphragm between the trusses is flexible.
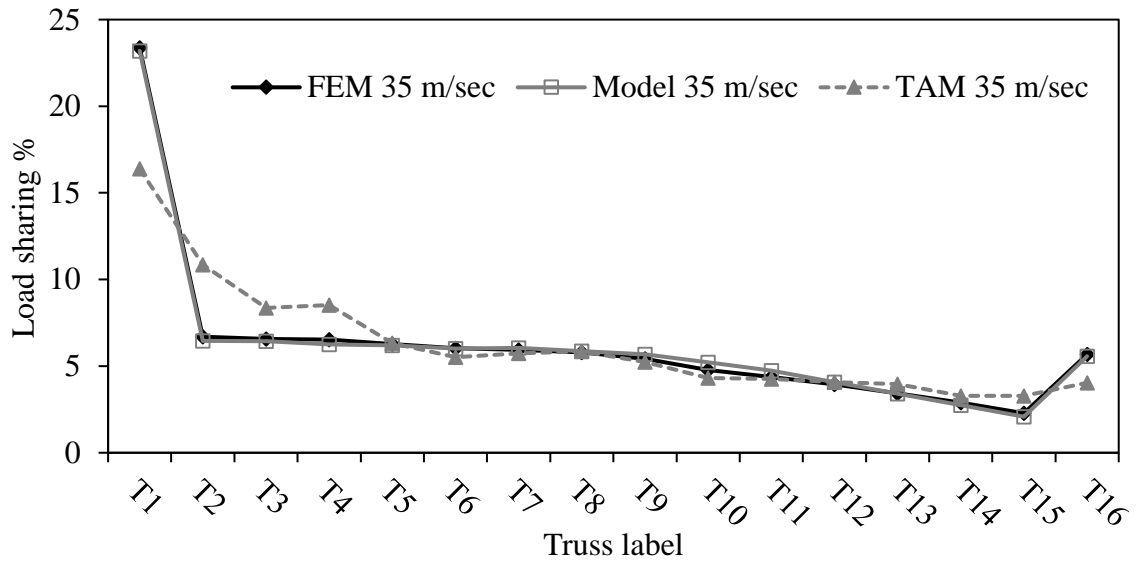
Figure 3.17: Comparison of load sharing computed using FEM, the solution model, and TAM at the maximum global realistic uplift load of a 35 m/sec wind speed.
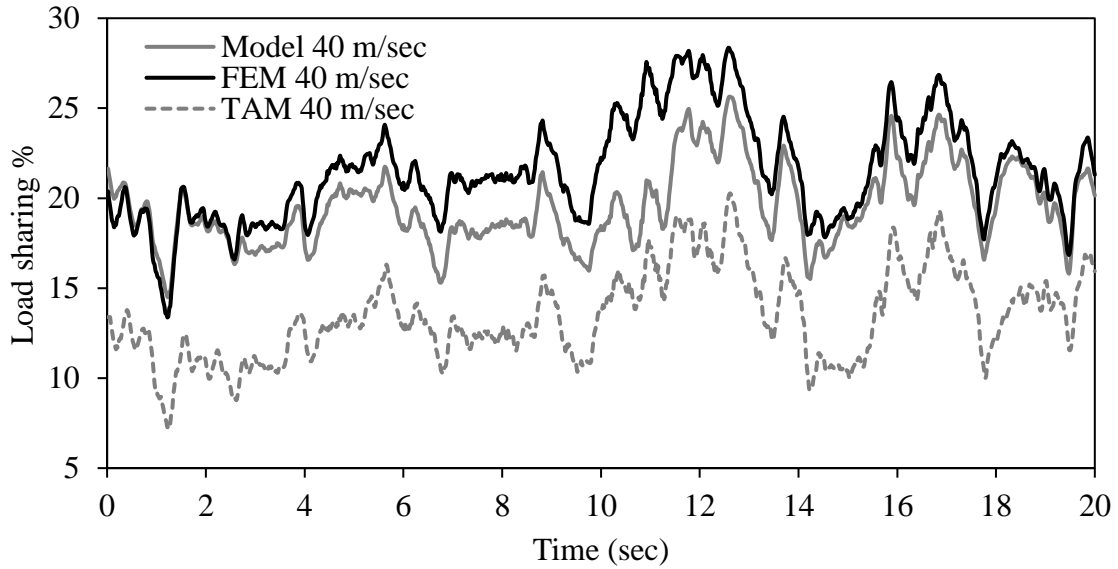
Figure 3.18: Comparison of load sharing computed using the FEM, solution model, and TAM results for end gable truss T1 under a realistic uplift load from a 40 m/sec wind speed.
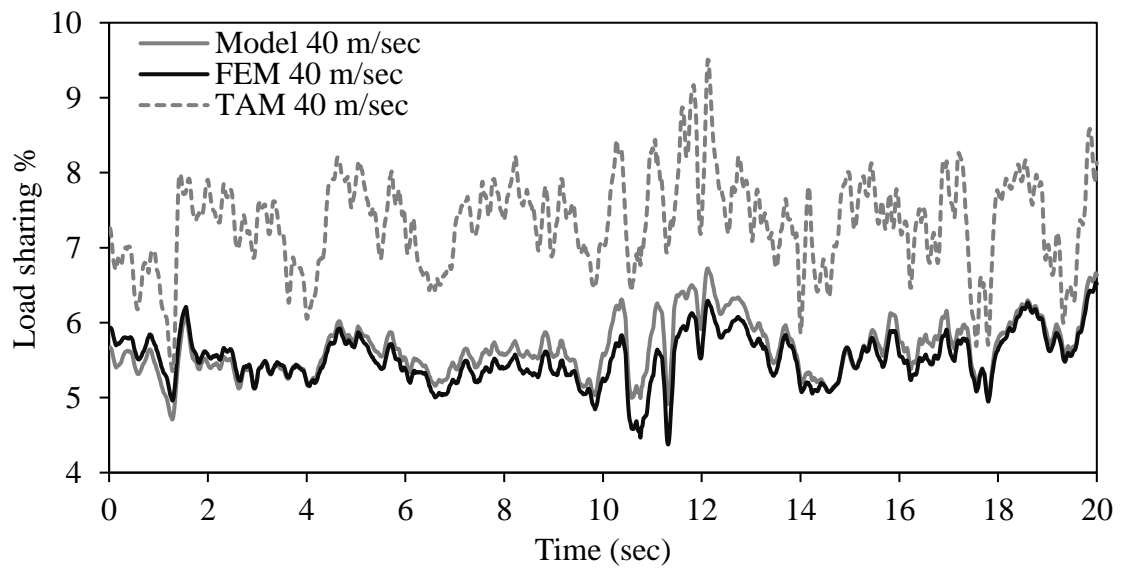
Figure 3.19: Comparison of load sharing computed using the FEM, solution model, and TAM results for middle truss T4 under a realistic uplift load from a 40 m/sec wind speed.

3.6 TAM and FEM versus Solution Model Results under a Code Load

This section presents a comparison of the simplest ways of evaluating RTWC reactions which is 2D TAM analysis versus the more complex FEM analysis. The comparison involved evaluations based on the code pressure established by the *National Building Code of Canada* (NBCC, 2010). The comparison was extended to include the use of a solution modelled with linear springs in order to investigate the performance of the solution model against the FEM and TAM results. The NBCC (2010) divides uplift wind load pressure into four regions: 2, 2E, 3, and 3E, with the greatest pressure being at 2E in the southeast direction where open terrain exposure has been selected in order to obtain the relevant pressure on the roof.

Figures 3.20 and 3.21 enable a comparison of the three methods with respect to determining the reactions of the RTWCs under pressure from 15 design wind speeds, ranging from 30 m/sec up to 45 m/sec. Figure 3.20 represents the reaction of RTWC S2, a connection that was selected because it was subjected to the highest magnitude of forces at the gable end trusses T1 and T16 (Figure 2.2), while Figure 3.21 indicates the greatest reaction of all of the RTWCs. It can be seen that the reactions obtained from the solution model match the FEM results well for the pressure from wind speeds of 30 m/sec to 39 m/sec, with an average percentage of difference from the FEM results of 11.9 % and 13.4 % for RTWC S2 and RTWC S3, respectively. Beyond the pressure from a wind speed of 39 m/sec, the FEM results tend to reach a constant value of maximum connection withdrawal, meaning that the connection will fail at this loading stage. However, the solution model still produces forces consistent with increases in the speed due to the use of linear springs in this comparison. On the other hand, the TAM analysis leads to underestimates of the reaction at RTWC S2 at the end gable trusses and overestimates of the reaction at RTWC S3 for the middle trusses, because the stiffness of the trusses is not taken into account.
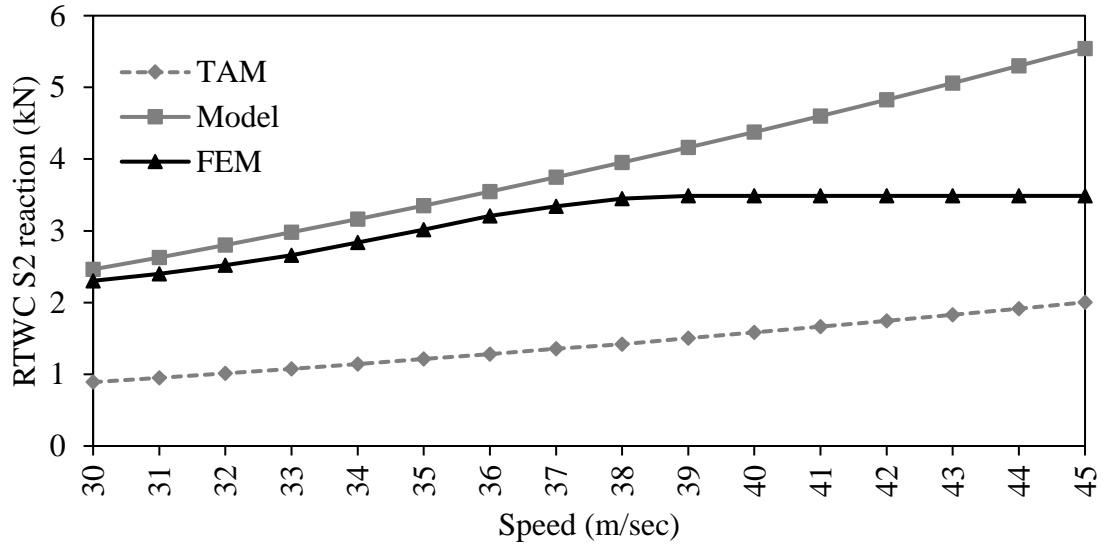
Figure 3.20: Comparison of load sharing computed using TAM, the solution model, and FEM analysis under a code uplift wind load at RTWC S2.
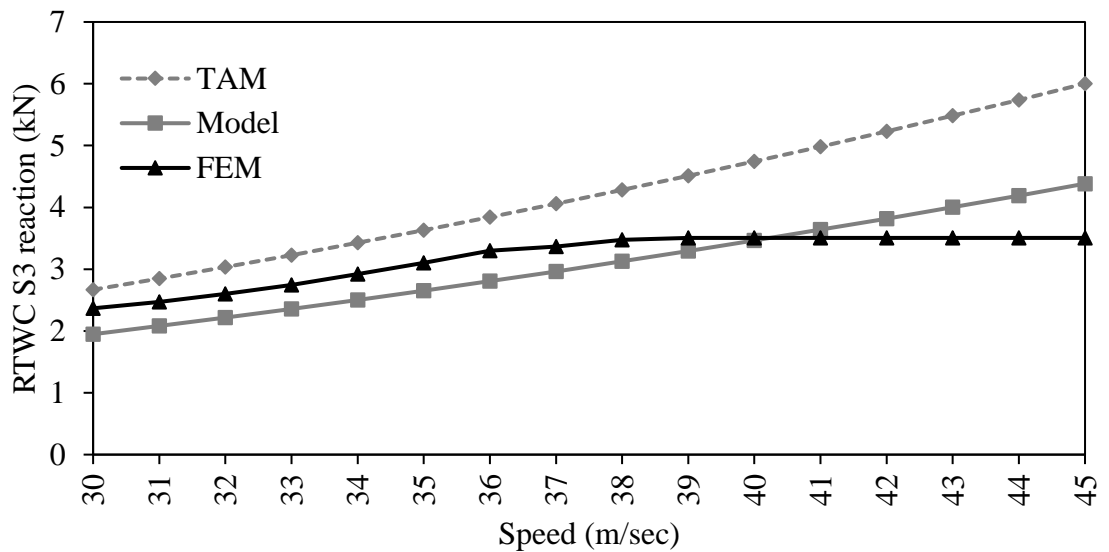
Figure 3.21: Comparison of load sharing computed using TAM, the solution model, and FEM under a code uplift wind load at RTWC S3.

3.7 Conclusion

This chapter has presented a method for analyzing critical connections in light-frame wood houses utilizing a semi-analytical solution under the effects of uplift wind loads. This semi-analytical solution hinges on the assumption that the diaphragms between the trusses are not flexible to transfer the uplift load based on the stiffness of each individual truss. Each truss was simulated as a linear spring in which the spring constant was evaluated according to the ratio of the unit load to top truss deflection. Statically indeterminate slope deflection equations that include the effects of shear deformation were used for deriving the modelled solution. For validation purposes, two pressure distributions were investigated: a realistic pressure and a code pressure. The realistic pressure was obtained from experimental testing conducted at the Insurance Research Lab for Better Homes located at the University of Western Ontario (Morrison et al., 2012), while the code pressure was estimated based on the requirements specified in the National Building Code of Canada (2010).

The validation process involved the execution of two strategies for analyzing the solution produced by the model, which included the use of linear and trilinear RTWC stiffness values. Based on the initial tangent slope of RTWC stiffness, good agreement was obtained between the FEM analysis and the modelled solution results for the gable roof in terms of all RTWC reaction at 35 m/sec. In addition to linear analysis validation, in-house coding was also written for evaluating the reaction of RTWC S3 through the time history, good agreement is indicated between the two analysis tools, resulting in a mean percentage difference of 9 % at wind speeds of 35 m/sec. The percentage difference for the RTWC S3 reaction increases to 31 % at wind speeds of 45 m/sec. The difference increases with greater wind speed, due to the approximation of solution model analysis.

In terms of the deflection at the RTWCs, good agreement was evident between the solution model results and the findings of the experimental testing conducted by Morrison et al., (2012) at wind speeds of 30 m/sec and 35 m/sec on the north and south sides of the gable roof. However, the solution model predictions tended to overestimate the deflection, especially for the south side of the gable roof under wind speeds of 40

m/sec and 45 m/sec. The overestimation was due to the use of a similar load-deflection curve for all RTWCs, which in reality vary, especially for toe-nailed connections.

The solution model was also used for investigating the percentage of load sharing between the trusses under the effects of uplift wind loads. This investigation involved the application of two common methods of analysis, FEM and TAM, and a reasonable match between the FEM and the solution model results was achieved, with difference of 0.43 %. A further comparison of the modelled solution against FEM and TAM analysis was conducted under the effects of code pressures (NBCC, 2010). It was observed that TAM analysis underestimates the reaction of the end gable truss connections while the modelled solution provides the closest match to the FEM results.

In summary, the significance of this model comparing to the existing three-dimensional FEM model is simplicity to use and effectively evaluated the reactions of the RTWCs, producing results in good agreement with FEM computations. Another advantage of this model is lesser computational time than FEM. However, with respect to RTWC deflection, the model tends to overestimate RTWC deflection at high wind speeds due to the variability inherent in the wood connections. This solution model can be implemented for reliability analysis that needs a large number of simulations.

3.8 References

Canadian Wood Council and Canadian Standards Association. (2010), "Wood design manual", The complete reference for wood design in Canada Ottawa, *Canadian Wood Council*.

Dao, T. N., van de Lindt, John W, Prevatt, D. O., and Gupta, R. (2012), "Probabilistic procedure for wood-frame roof sheathing panel debris impact to windows in hurricanes", *Engineering Structures*, **35**,178-187.

Datin, P. L., Mensah, A. F. and Prevatt, D. O. (2010), "Experimentally Determined Structural Load Paths in a 1/3-Scale Model of Light-Framed Wood, Rectangular Building", *2010 ASCE Structures Congress*, Orlando, Florida, United States, May.

Dessouki, A. A. (2010), "Analysis and retrofitting of low rise houses under wind loading", Master Thesis, University of Western Ontario, London, ON, Canada.

Doudak, G., McClure, G. and Smith, I. (2012), "Experimental evaluation of load paths in light-frame wood structure", *Journal of Structural Engineering*, **138**(2), 258-265.

Enajar, F.E., Jacklin, R.B., El Damatty, A.A. (2019), "Nonlinear Modeling of Roof to Wall Connections in a Gable-Roof Structure under Uplift Wind Loads", *Wind and Structures*, **28**(3),181-190.

FEMA (1992), *Building Performance: Hurricane Andrew in Florida, Observation, Recommendations, and Technical Guidance*, Federal Emergency Management Agency, Federal Insurance Administration, United States.

Guha, T.K. and Kopp, G.A. (2014), "Storm duration effects on roof-to-wall-connection failures of a residential, wood-frame, gable roof", *Journal of Wind Engineering and Industrial Aerodynamics*, **133**, 101-109.

Jacklin, R. B. (2013), "Numerical and experimental analysis of retrofit system for light-framed wood structures under wind loading", Master Thesis, University of Western Ontario, London, ON, Canada.

Jacklin, R.B., El Damatty, A.A. and Dessouki, A.A. (2014), "Finite-element modeling of a light-framed wood roof structure", *Wind and Structures*, **19**(6), 603-621.

Kasal, B., and Leichti, R. J. (1992), "Incorporating load sharing in shear wall design of light-frame structures", *Journal of Structural Engineering*, **118**(12), 3350-3361.

Kasal, B., Collins, M., Paevere, P. and Foliente, G. (2004), "Design models of light frame wood buildings under lateral loads", *Journal of Structural Engineering*, **130**(8), 1263-1271.

Khan, M. A. A. (2012), "Load-sharing of toe-nailed, roof-to-wall connections under extreme wind loads in wood-frame houses", Master Thesis, University of Western Ontario, London, ON, Canada.

Li, Y., and Ellingwood, B. R. (2006), "Hurricane damage to residential construction in the US: importance of uncertainty modeling in risk assessment", *Engineering Structures*, **28**(7), 1009-1018.

Martin, K. G. (2010), "Evaluation of system effects and structural load paths in a wood-framed structure," Master Thesis, Oregon State University, Corvallis, Oregon, UAS

Morrison, M. J., Henderson, D. J. and Kopp, G. A. (2012), "The response of a wood-frame, gable roof to fluctuating wind loads", *Engineering Structures*, **41**, 498-509.

Morrison, M. J. and Kopp, G. A. (2011), "Performance of toe-nail connections under realistic wind loading", *Engineering Structures*, **33**, 69-76.

NBCC (2010), *User's Guide--NBC 2010: Structural Commentaries (Part 4 of Division B)*, Canadian Commission on Building and Fire Codes, National Research Council Canada, and Institute for Research in Construction (Canada), Ottawa, ON, Canada.

NDS (2015), *National Design Specification for Wood Construction*, American Wood Council, Leesburg, Virginia, USA.

Phillips, T. L. (1990), "Load sharing characteristics of three-dimensional wood diaphragms" Master Thesis, Washington State University, Pullman, Washington.

Paevere, P. J., Foliente, G. C., and Kasal, B. (2003), "Load-sharing and redistribution in a one-story woodframe building", *Journal of structural engineering*, **129**(9), 1275-1284.

Reed, T. D., Rosowsky, D. V. and Schiff, S. D. (1997), "Uplift capacity of light-frame rafter to top plate connections", *Journal of Architectural Engineering*, **3**(4), 156-163.

Rojas, A. L. (2012), "Method of structural analysis for statically indeterminate beams", International Journal of Innovative Computing Information and Control, **8**(8), 5473-5486.

Shivarudrappa, R. and Nielson, B. G. (2013), "Sensitivity of load distribution in light-framed wood roof systems due to typical modeling parameters", *Journal of Performance of Constructed Facilities*, **27**(3), 222-234.

Wolfe, R. (1996), "Structural Performance of Light-Frame Truss-Roof Assemblies", *Proceedings of the international engineering conference*, October 28-31; New Orleans, LA, Baton Rouge, LA, Louisiana State University, **3**, 263-268

Chapter 4

4 Reliability of Roof-to-Wall Connections in a Gable Roof Structure under Uplift Wind Loads

4.1. Introduction

Most North American residential structures are light-frame wood houses (Rosowsky and Cheng, 1999, I; Rosowsky and Cheng, 1999, II; Rosowsky et al., 2005). Recent catastrophic hurricanes have been responsible for significant damage to these types of wooden houses (He et al., 2017; Mishra et al., 2017). The mitigation of these damages is necessary to reduce the possible failure by better understanding the failure mechanisms. One of the failure mechanisms identified is a deficiency with respect to the creation of a continuous load path from the roof of the house to the foundation (Rosowsky and Cheng, 1999, II). This defect arises as a result of a weak roof connection or because the structure of a house has not been adequately designed (Rosowsky and Cheng, 1999, II). The lack of a continuous load path within a light-frame wood house could result in loss of the roof. Another factor associated with the absence of a continuous load path is the creation of a permanent gap between the roof and the walls during hurricanes; this permanent gap can ruin furniture due to the intrusion of water from wind-driven rain (Rosowsky and Cheng, 1999, II; Dao and van de Lindt, 2010).

The main difficulty caused by the loss of a continuous load path is weakness in the roof-to-wall connections (RTWCs) with respect to resisting applied tension loads. RTWCs are characterized as belonging to two main categories: toe-nail connections and hurricane strap connections. Toe-nail connections exhibit greater variation and lower withdrawal capacity than hurricane strap connections (Reed et al., 1997). The research presented in this thesis was focussed on toe-nailed RTWCs. Individual testing of toe-nail connections results in varied load-deflection curves (Khan, 2012). Variability in the stiffness of toe-nail connections means that some connections are stronger than others with respect to transferring tension loads. One objective of this research was to evaluate the behaviour of typical light-frame wood houses through an examination of the impact on a system arising from variability in the stiffness of the toe-nail connections. This goal was

achieved by applying statistical reliability analysis to the semi-analytical solution model developed in Chapter 3 to three-dimensional full-scale gable roof in order to evaluate the reliability of the roof truss system. The semi-analytical model (Chapter 3) yielded a fast model that was easy to employ in the computationally intensive Monte Carlo simulation used for reliability analysis.

Previous studies employed reliability analysis as a means of assessing the performance of light-frame wood houses under wind loads. However, studies were either confined to two dimensional cross-sections of the roof (Guha and Kopp, 2014) or a portion of the roof structure (Gleason, 2009). Rosowsky and Cheng, (1999, II) performed first-order second-moment reliability analysis for gable roof houses, and they concluded that corner sheathings and RTWCs close to end gable trusses are vulnerable to failure. Gleason's (2009) investigation of the reliability of gable roof houses included consideration of two random variables: RTWCs and uplift wind loads. A Monte Carlo simulation was used as a reliability tool, in combination with OpenSees open source finite element software. With his probabilistic RTWC models, Gleason (2009) integrated normal, lognormal, and Weibull distributions, as cited in Shanmugam et al., (2009), while he used lognormal distribution for the uplift wind loads. Two wind speeds of 100 mph and 130 mph in 3-sec gusts were selected for the study, and Gleason (2009) concluded that the probability of failure was 5 % and 38 % for the respective selected wind speeds.

Shanmugam (2011) conducted a detailed reliability analysis for a gable roof house using Monte Carlo simulations that incorporated both the variability in the stiffness values of the RTWCs and the sheathing-to-truss connections (STTCs) as well as the variability in the uplift wind loads on the roof, and he employed ANSYS commercial software as a finite element modelling (FEM) tool for analyzing these simulations. He concluded that incorporating the negative stiffness of the connections after failure had a notable impact on the fragility curves, while designating the random or deterministic stiffness of the connections before peak capacity had little effect on system failure. The spatial correlation of wind uplift pressures also had no effect on the evaluation of the reliability of the roof system (Shanmugam, 2011). van de Lindt et al., (2013) presented a fragility assessment of light-frame wood houses under hurricane loads. The degree of fragility was

evaluated with respect to 2-16D toe-nailed RTWCs. The authors stated that the reliability of the wood houses was 0.33 at 3-sec 44 m/sec wind speed gusts. According to their results, this reliability also increased dramatically when hurricane straps were used rather than toe-nailed RTWCs.

From an economic point of view, designing a house with zero probability of failure is impossible; it is therefore important to determine the probability of failure based on reliability analysis. Monte Carlo simulations have been employed for estimating the reliability of roof truss systems based on the use of appropriate probabilistic models. This simulation approach has been adopted for evaluating the reliability of wooden houses with a variety of components (Rosowsky et al., 2005; Standohar-Alfano et al., 2017; Wang and Eamon, 2013).

Li and Ellingwood (2006) employed the limit state function between the resistance of toe-nail roof-to-wall connection and the applied uplift wind load to evaluate the fragility curve with respect to the 3-sec gust wind speeds. In their study, they used a normal distribution probabilistic model for generation of both the toe-nail resistance (Reed et al., 1997) and the uplift wind load (Ellingwood and Tekie, 1999). Monte Carlo simulations were used in this chapter to develop the fragility curve taking the nonlinearly of the toe-nail connection into account. Padmanabhan et al. (2006) stated that the estimation of the probability of failure using the Monte Carlo simulations provides accurate results with the expense of more computational time compared to the limit state approximation. The output of Monte Carlo simulations has been employed for assessing the effects of variability in the stiffness of toe-nailed connections with respect to the failure of a roof truss system. The semi-analytical solution model used in the simulations represents a simplified solution based on an evaluation of the load sharing among the trusses. Beta and normal distributions were adopted for generating random stiffness values for the toe-nailed RTWCs and for the random uplift wind pressure, respectively.

4.2. Random Load Deflection-Curve and Uplift Wind Load

An important element of the Monte Carlo simulation is to employ the probabilistic models for evaluating components that affect the behaviour of the roofs. These components can be summarized as the random capacity of the RTWCs and the random uplift wind load.

4.2.1 Probabilistic RTWC Load Deflection-Curve

RTWC load-deflection curve is characterized by a high degree of variability, especially with respect to toe-nail connections (Reed et al., 1997). Khan (2012) conducted experimental testing for individual RTWCs under ramp load. The experiment involved 35 RTWCs, each of which had similar setups using 3-12D nails. Figure 4.1 illustrates the output of the individual RTWC testing conducted by Khan (2012), which demonstrates the wide variability in the stiffness of the toe-nailed RTWCs.

 In the current study, and based on the experimental testing conducted by Khan (2012), trilinear RTWC curves were generated with the use of an appropriate probabilistic model. The choice of trilinear curves was driven by its usage as an approximation for the non-linear behavior of the stiffness curves of the connection and the development of a solution model that depends on it as discussed in Chapter 3. Figure 4.2 shows the bounds of generating a random RTWC stiffness curve. Based on experimental results conducted by Khan (2012), it was necessary to find the type, parameters, and bounds of the probability distribution, which is shown in Figure 4.2. The probability distribution of choice was the beta distribution, which will be discussed later in details. A first-degree B-spline was used to fit the trilinear stiffness curves to the experimental data. This B-spline curve fitting has the advantage of providing a piecewise linear fit to the data points. A B-spline curve, (Figure 4.3) is a free form geometric representation method that can be used to represent curves of multiple degrees. Hence, they can be used to fit approximate trilinear stiffness curves to the experimental data.
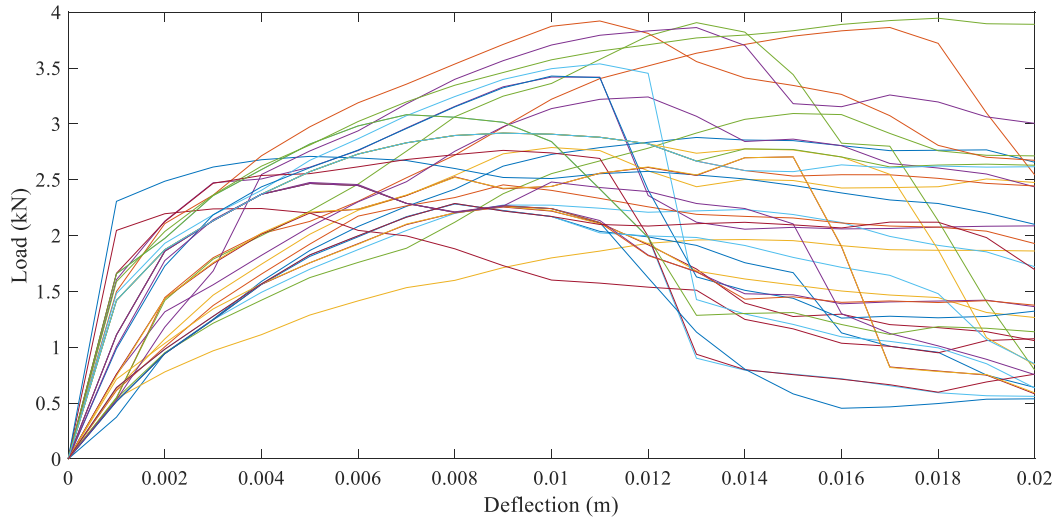
Figure 4.1: Load-deflection curves for the 35 RTWCs evaluated by Khan (2012).

The first step in generating the random trilinear curves for the RTWCs is to find the bounds between which the curve points will be generated (Figure 4.2). In order to achieve such objective, the experimentally obtained stiffness curves (Khan 2012) need to be approximated by the B-splines and the lower and upper bounds of the approximations need to be identified followed by a maximum likelihood estimation of the parameters of the probability distribution between the bounds. A typical B-spline curve is shown in Figure 4.3. This B-spline curve is defined by set of control points which constitute a linear approximation of the curve. If the curve degree is set to one, the lines connecting the control points become the curve itself. To generate a trilinear stiffness curve, three control points were to be generated from three probability distributions (Figure 4.2) which, along with the origin point, constitute the four control points needed for the B-spline trilinear curve. A step preceding the above procedure is the identification of the x-locations and the bounds of the probability curves. To achieve this step, first degree B-spline fitting is applied to the experimentally produced stiffness curves and their control points are used to identify those bounds as shown below:
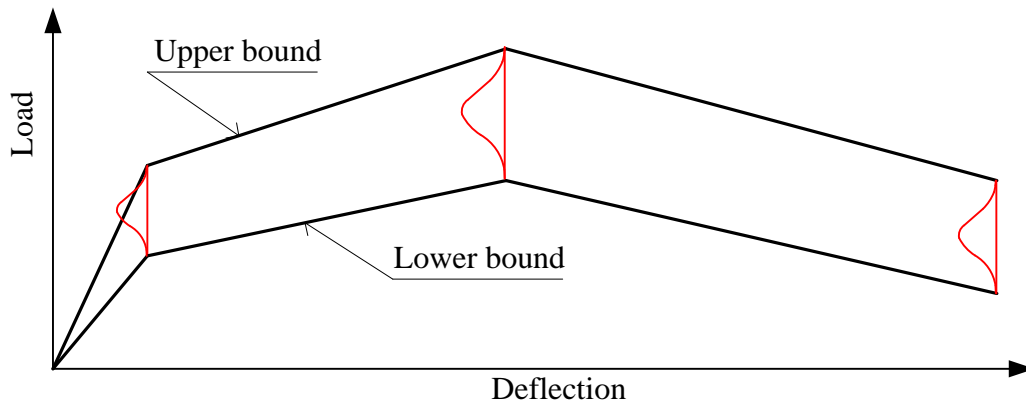
Figure 4.2: Lower and upper bound for generating random trilinear stiffness of RTWCs.
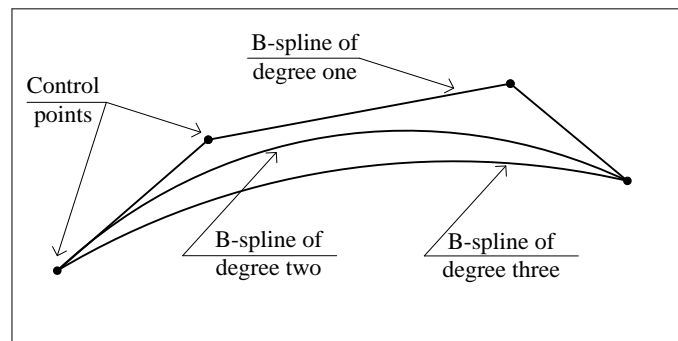
Figure 4.3: Sample of B-spline curve.

The first trial was proposed by using four control points, with a first order curve degree between the control points. Four control points were selected to follow the trilinear curves of RTWC. Figure 4.4 illustrates the output of the first trial curve fitting. It is clear from this figure that using four control points for each curve did not provide an accurate estimation of the initial tangent stiffness, which is of particular importance to predict the RTWCs reactions. The best fit for the measured data, that would not sacrifice the important initial tangent, was found to be eight control points, with a first order curve degree between the control points. However, these eight control points would need further re-adjustment to yield a trilinear stiffness curve which retains the initial stiffness.

MATLAB code was written in order to establish the required curve fitting. In this code, the experimental data measured by Khan (2012) are inserted for the 35 RTWCs. In each RTWC curve, the measured deflection and load are evaluated at 21 equal incremental deflection steps, until a maximum deflection of 20 mm is reached. From the input number of control points and the number of incremental deflection steps, the basis function of the B-spline can be evaluated in form of a matrix in the order of 21×8, as shown in Equation (4.1). Details for the estimation of the B-spline basis functions for curve fitting are given by Piegl and Tiller (1997). A B-spline fit is applied to the measured points of the 35 experiments as shown below:
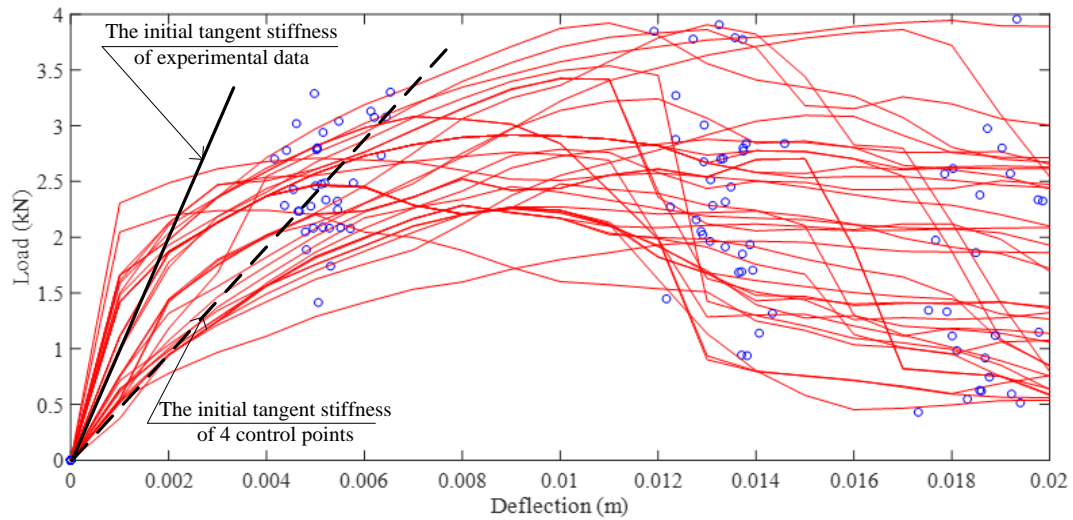
Figure 4.4: Output of the first trial curve fitting.

To obtain the position of the control points for each RTWC, the B-spline basis function matrix must be established. Equation (4.2) represents the relation between the known measured data (x_{m1} to x_{m21}) and the unknown control points (x_0 to x_7). Equation (4.3) denotes the same relation as in Equation (4.2), but with y denotes the loads. It is obvious that the Equation (4.1) matrix is not square and does not have full rank. The inverse of this matrix therefore does not exist, thus making it impossible to determine an exact solution for x and y; however, it is possible to obtain their least square solution, which can be approached by multiplying the measured data vector by the Moore-Penrose pseudoinverse matrix:

$$\begin{bmatrix} N_{0,1(u_{m1})} & N_{1,1(u_{m1})} & \cdots & N_{7,1(u_{m1})} \\ N_{0,1(u_{m2})} & N_{1,1(u_{m2})} & \vdots & N_{7,1(u_{m2})} \\ \vdots & \vdots & \vdots & \vdots \\ N_{0,1(u_{m21})} & N_{1,1(u_{m21})} & \vdots & N_{7,1(u_{m21})} \end{bmatrix}_{21 \times 8}$$ (4.1)

$$\begin{bmatrix} x_{m1} \\ x_{m2} \\ \vdots \\ x_{m21} \end{bmatrix} = \begin{bmatrix} N_{0,1(u_{m1})} & N_{1,1(u_{m1})} & \cdots & N_{7,1(u_{m1})} \\ N_{0,1(u_{m2})} & N_{1,1(u_{m2})} & \vdots & N_{7,1(u_{m2})} \\ \vdots & \vdots & \vdots & \vdots \\ N_{0,1(u_{m21})} & N_{1,1(u_{m21})} & \vdots & N_{7,1(u_{m21})} \end{bmatrix} \begin{bmatrix} x_0 \\ x_1 \\ \vdots \\ x_7 \end{bmatrix}$$ (4.2)

$$\begin{bmatrix} y_{m1} \\ y_{m2} \\ \vdots \\ y_{m21} \end{bmatrix} = \begin{bmatrix} N_{0,1(u_{m1})} & N_{1,1(u_{m1})} & \cdots & N_{7,1(u_{m1})} \\ N_{0,1(u_{m2})} & N_{1,1(u_{m2})} & \vdots & N_{7,1(u_{m2})} \\ \vdots & \vdots & \vdots & \vdots \\ N_{0,1(u_{m21})} & N_{1,1(u_{m21})} & \vdots & N_{7,1(u_{m21})} \end{bmatrix} \begin{bmatrix} y_0 \\ y_1 \\ \vdots \\ y_7 \end{bmatrix}$$ (4.3)

Suppose that Equation (4.2) can be written as follows:

$$x_m = N \times x$$ (4.4)

The least square solution of $\overset{*}{x}$ can then be determined as follows:

$$N^T \times x_m = N^T \times N \times x$$ (4.5)

$$\overset{*}{x} = \left(N^T \times N\right)^{-1} \times N^T \times x_m$$ (4.6)

$\left(N^T \times N\right)^{-1} \times N^T$ is designated as the Moore-Penrose pseudoinverse matrix, which provides the best prediction of the position of control points.

Similarly, the least square solution of $\overset{*}{y}$ can be obtained as follows:

$$\overset{*}{y} = \left(N^T \times N\right)^{-1} \times N^T \times y_m$$ (4.7)

Figure 4.5 illustrates the predicted positions of the control points identified by the blue circles at the top of the experimental data. Each RTWC curve has a total of eight control points. Based on a visual inspection of Figure 4.5, and in order to identify the trilinear

RTWC curve, it was assumed that the second control points in all the curves represent the RTWC yield points. It is also assumed that the ultimate load that the RTWCs can resist lies at the fifth control points, and that the end control points represent the point at which the RTWCs lose their strength. For simplicity, the RTWC deflection at the yield and ultimate points can be determined from the mean deflection values of all second and fifth control points, respectively. The deflection at the point at which the RTWCs lose their strength is specified as 0.02 m.
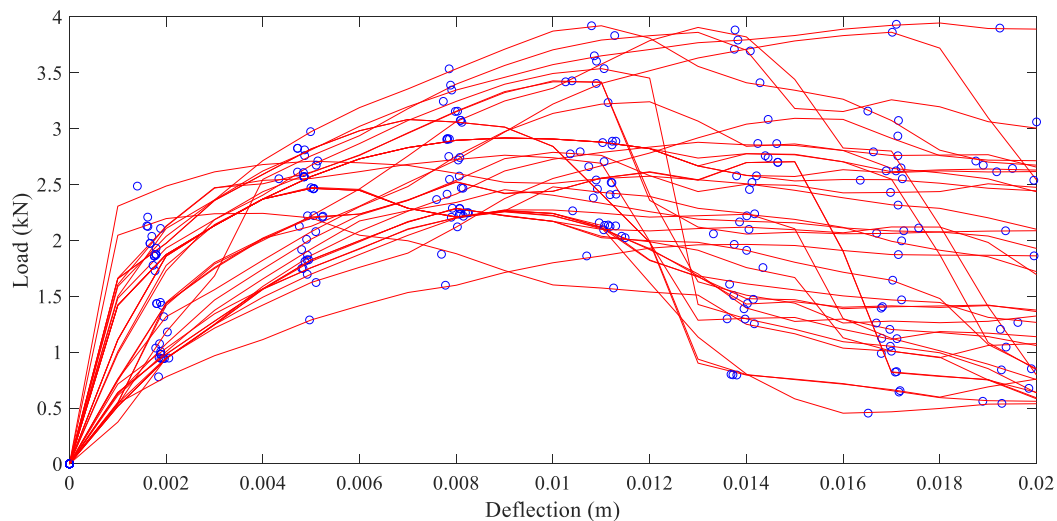
Figure 4.5: Predicted control points for all data from the experiments conducted by Khan (2012).

Previous studies implemented different types of probabilistic models to generate the random stiffness for RTWCs, for example, Shanmugam et al., (2009) used normal, lognormal, and Weibull distributions, while Guha and Kopp (2014) used lognormal probabilistic models. The normal distribution is unbounded, which means that it has extreme negative or positive values. Lognormal and Weibull distributions are partially bounded start with zero to infinity. In this chapter, the beta distribution was employed for generating suitable random trilinear stiffness values for the RTWCs because it is a bounded distribution that provides the best choice for producing a random stiffness value within the maximum and minimum measurements acquired from the experimental data. Benjamin and Cornell (2014) stated that, because of its flexibility, the beta distribution is the best approach for describing the experimental data.

After the deflections associated with the yield, ultimate, and end RTWC stiffness have been identified, the random withdrawal loads at the second, fifth, and end control points are determined using the beta distribution. To perform this task, maximum likelihood estimation is utilized for establishing the first and second shape parameters of the beta distribution. Identification of the shape parameters of the beta distribution in the second, fifth, and end control points enables the generation of random forces at these control points.

The strategy for the selection of the RTWC random load-deflection curve is based on the concept that the ultimate connection capacity is greater than the force at either the yield point or the end curve point. The force at the end curve point should also be less than that at the ultimate connection capacity. To achieve this strategy, the shape parameters of the fifth control point are evaluated to be relative to the second control points, and the shape parameters of the end control point are set to be relative to the fifth control points. Figure 4.6 illustrates the maximum, minimum, and average control points values throughout the load-deflection curve. Hence the shape parameters of the beta distributions at the second, the fifth and the end control points will be estimated using the relative values for the forces instead of the absolute values.
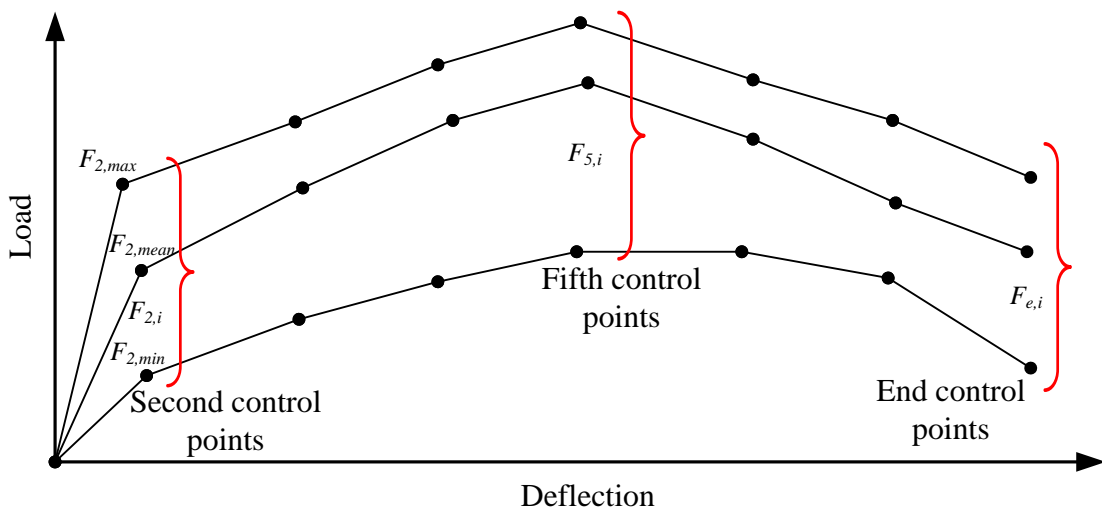
Figure 4.6: Second, fifth, and end control points of the load-deflection curves.

It is worth noting that the standard beta distribution is defined over a bounded range from 0 to 1. Therefore, all experimental forces used in the determination of the shape parameters of the beta distributions will be normalized to range from zero to one:

For the second control point, let:

$$r_{2,i} = \frac{F_{2,i} - F_{2,min}}{F_{2,max} - F_{2,min}}$$

(4.8)

where

$r_{2,i}$ The ith normalized force of the 2nd control point, ($1 \leq i \leq 35$);

$F_{2,i}$ The ith force value of the 2nd control point;

$F_{2,min}$ The minimum force value of the 2nd control points;

$F_{2,max}$ The maximum force value of the 2nd control points;

The fifth control point should be higher than the second control point, therefore the beta distribution is defined on the normalized percentage increase in force value between the 5th and the 2nd control point:

$$P_{5,i} = \frac{F_{5,i} - F_{2,i}}{F_{2,i}}$$

(4.9)

where

$P_{5,i}$ The ith percentage increase in force value between the 5th and 2nd control point;

$F_{5,i}$ The ith force value of the 5th control point;

The percentage $P_{5,i}$ is further normalized as per the following equation:

$$r_{5,i} = \frac{P_{5,i} - P_{5,min}}{P_{5,max} - P_{5,min}}$$ (4.10)

where

$r_{5,i}$ The normalized percentage increase in force value between the 5th and 2nd control point, ($1 \leq i \leq 35$);

$P_{5,min}$ The minimum percentage increase in force value between the 5th and 2nd control point;

$P_{5,max}$ The maximum percentage increase in force value between the 5th and 2nd control point;

As the end control point should be lower than the 5th control point, the above set of equations are repeated in the same manner:

$$P_{e,i} = \frac{F_{e,i} - F_{5,i}}{F_{5,i}}$$ (4.11)

where

$P_{e,i}$ The ith percentage decrease in force value between the end and 5th control point, ($1 \leq i \leq 35$);

$F_{e,i}$ The ith force value of the end and 5th control point;

The percentage $P_{e,i}$ is further normalized as follows:

$$r_{e,i} = \frac{P_{e,i} - P_{e,min}}{P_{e,max} - P_{e,min}}$$ (4.12)

where

$r_{e,i}$ The normalized percentage decrease in force value between the end and 5th control point;

$P_{e,min}$ The minimum percentage decrease in force value between the end and 5th control point;

$P_{e,max}$ The maximum percentage decrease in force value between the end and 5th control point;

Using the relative force data sets ($r_{2,i}$, $r_{5,i}$, $r_{e,i}$) the maximum likelihood analysis is used to evaluate the corresponding beta distribution shape parameters. The first and second shape parameters of the beta distribution are summarized in Table 4.1. The first shape parameter is denoted by the letter A and the second by the letter B.

Table 4.1: Beta distribution shape parameters

Random Variable	Normalized yield force	Normalized percentage increase from the yield force (i.e. peak force)	Normalized percentage decrease from the peak force (i.e. end force)
First shape parameter (A)	A2 = 1.0628	A5 = 1.0636	Ae = 1.0620
Second shape parameter (B)	B2 = 1.1562	B5 = 1.1582	Be = 1.1482

The shape parameters in Table 4.1 were used for the random generation of stiffness curves. The generation of a random stiffness curve follows the procedure shown below:

1. Generate ω_2 , ω_5 and ω_e. These are three random variables generated between a range of 0 to 1 from standard beta distributions with shape parameters (A_2,B_2), (A_5,B_5) and (A_e,B_e) respectively.
2. The force at the yield point F_2 is generated as follows:

$$F_2 = F_{2,\min} + \omega_2\left(F_{2,\max} - F_{2,\min}\right) \tag{4.13}$$

3. The peak force F_5 is generated as follows:

$$F_5 = F_2 + \omega_5\left(F_{5,\max} - F_2\right) \tag{4.14}$$

4. The end force F_e is generated as follows:

$$F_e = F_5 - \omega_e\left(F_5 - F_{e,\min}\right) \tag{4.15}$$

A typical randomly generated stiffness curve using the above equations is shown in Figure 4.7.
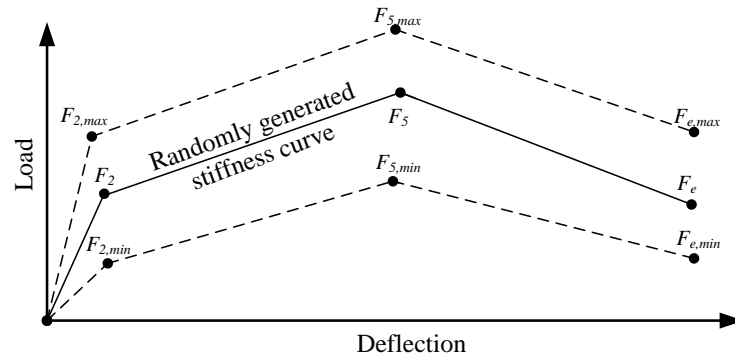
Figure 4.7: Typical randomly generated stiffness curve.

The random stiffness curve generation Equations 4.13 to 4.15 along with the shape parameters of Table 4.1 were used to generate 100 curves. The mean curve of the those randomly generated curves is shown in Figure 4.8 by the bold solid line. The figure also shows the experimental stiffness curves as well as the mean experimental stiffness curve which is shown by a bold dashed line. It is obvious that the mean randomly generated stiffness line is in agreement with the experimental mean with a maximum deviation of 13%.

———— Mean trilinear stiffness curve of 100 random generation

- - - - Mean stiffness curve of the 35 experimental curves (Khan, 2012)
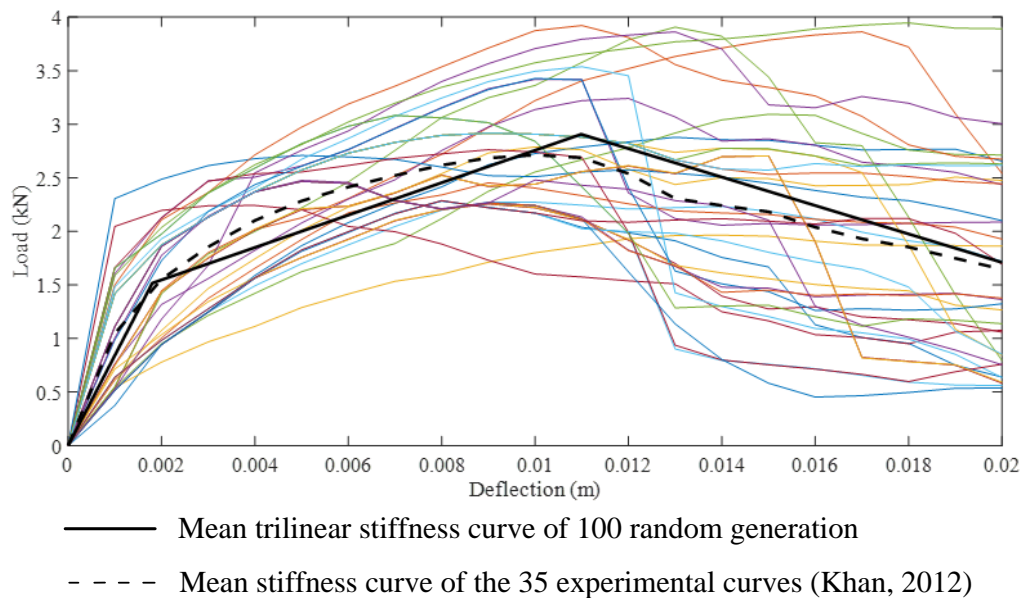
Figure 4.8: Average of one hundred load-deflections generated using the beta distribution compared with the data from the experiments conducted by Khan (2012).

4.2.2 Probabilistic Uplift Wind Pressure Model

A normal distribution probability model has been previously used for estimating the wind uplift pressure coefficients (CpCg) for the four pressure zones on a gable roof (Ellingwood and Tekie, 1999) having similar slope to that considered in this chapter. These CpCg wind uplift pressure coefficients represent the product of the pressure coefficient Cp and the gust factor Cg. An approximate version of this probabilistic model was used in the work conducted for this chapter, but with the pressure coefficients obtained from the *National Building Code of Canada* (NBCC, 2010). Ellingwood and Tekie (1999) stated that the ratio of mean to nominal CpCg ranges from 0.86 to 0.8, with the coefficient of variation selected to be 0.17. In the research for this chapter, the ratio of mean to nominal CpCg was taken as 0.83, with the same coefficient of variation of 0.17. Table 4.2 lists the CpCg normal distribution parameters.

Table 4.2: CpCg normal distribution parameters

Building surfaces	Nominal	Mean	COV	STD
2	1.3	1.079	0.17	0.18343
2E	2	1.66	0.17	0.2822
3	0.7	0.581	0.17	0.09877
3E	1	0.83	0.17	0.1411

4.3. Solution Model

The solution model used for the analysis of the Monte Carlo simulation is a simplified solution. Compared with the results of three-dimensional nonlinear finite element analysis, the use of this simplified solution for the analysis of a gable roof house, as reported in Chapter 3, produced good predictions of RTWC reactions. With respect to RTWC deflections, the simplified solution results were also validated against the findings of experimental testing conducted at the Insurance Research Lab for Better Homes (IRLBH) located at the University of Western Ontario (Morrison et al., 2012).

This chapter describes the use of the same full-scale gable roof house for the analysis, but with larger pressure areas in order to enhance accuracy. As can be seen in Figure 4.9, in the study presented in this chapter, 2112 pressure areas were used in the solution model rather than the 58 pressure areas that were employed in the work explained in Chapter 3. Another modification that increases the accuracy of the solution model is to divide each RTWC into 30 increments. As discussed in Chapter 3, the simplified solution is based on evaluating the load share of each truss from an analysis of the entire roof as a beam on an elastic foundation. Once the load share of each individual truss has been calculated, two-dimensional FEM is utilized for analyzing the truss and for establishing the tension force exerted at each RTWC.

As shown in Figure 4.9, the plan of the gable roof used for this study is approximately 9 m by 9 m, with a roof slope of 1:3. The gable roof consists of 16 Howe trusses spaced 0.6 m apart, all having a roof overhang of 0.5 m in each direction. The middle 14 trusses are each supported by two RTWCs, one on the north side and one on the south side of the house, while the remaining two trusses are gable end trusses, one each on the eastern and western sides, which are supported by walls as well as by seven RTWCs. The top and bottom chord sections of the trusses are 2 in. by 4 in., and all webs are 2 in. by 3 in. The thickness of the plywood sheathing used is 9 mm.

The wind load was simulated based on the uplift pressure coefficients from NBCC (2010), which defines wind speed as the mean hourly wind speed and divides uplift wind pressure into four zones: 2; 2E; 3; and 3E, with the greatest pressure being at 2E in the southwest direction. NBCC (2010) also provides two categories of uplift pressure coefficients for gable roofs: the main wind force resisting system, and components and cladding. Standohar-Alfano (2016), for example, employed the first category for his evaluation of the forces in RTWCs, but with ASCE 7-10. For the work reported in this chapter, the uplift pressure coefficients obtained for the main wind force resisting system were used. Open terrain exposure was selected for the analysis in order to obtain values for the relevant pressure on the roof. The use of the solution model for the analysis of the gable roof requires that the wind load be applied incrementally in a quasi-static manner. The uplift wind load used in the analysis could therefore be divided into a number of

increments or could be applied with wind speeds ranging from 1 m/sec up to the speed resulting in complete roof failure.
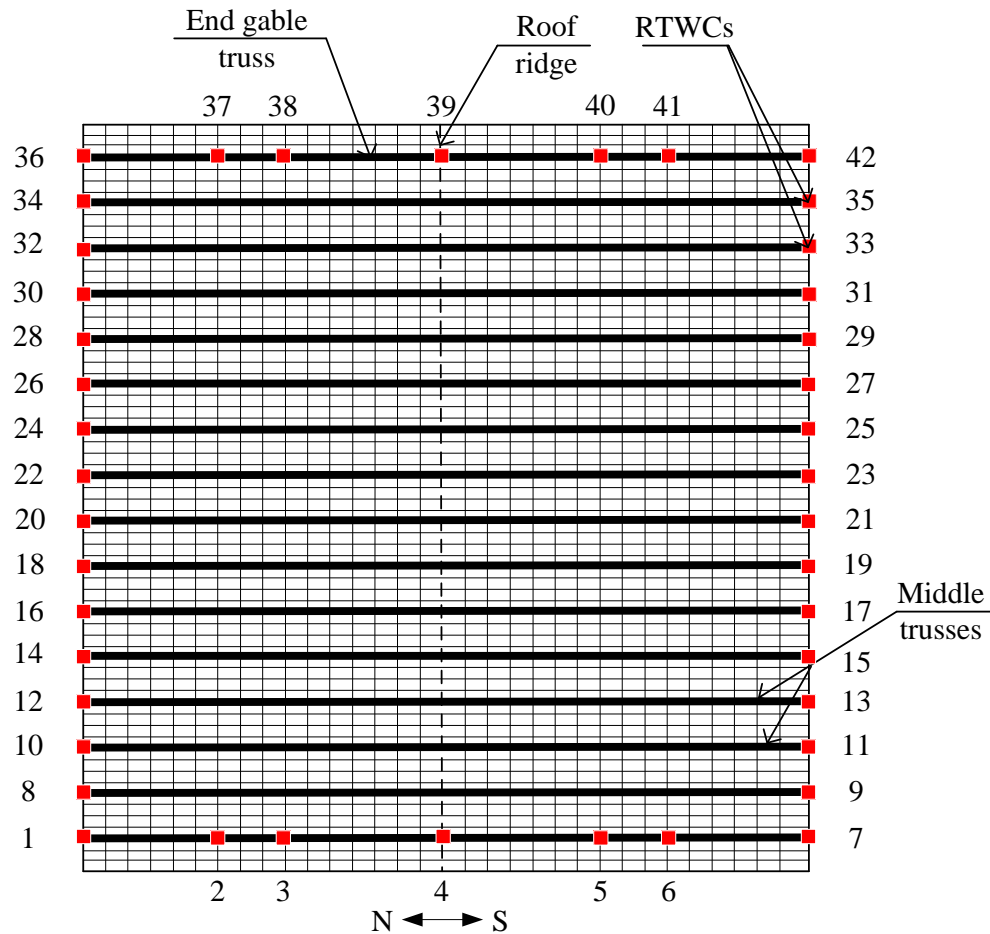
Figure 4.9: Layout of the gable roof used for the simulation.

Previous chapters explain how the solution produced by the model was examined either using FEM or against the experimental results in terms of the use of identical RTWC stiffness values as a mean value derived from the experimental results. The work presented in this section necessitated an investigation of the performance of the solution model using random RTWC values. To this end, 42 random RTWC stiffness values were generated using the beta distribution discussed in the previous section, which were

plotted as shown in Figure 4.10. As indicated in Figure 4.9, the house roof was supported by 42 RTWCs, so each connection was assigned one random stiffness value. The investigation could then be carried out using two different analysis methods: the solution model and FEM with SAP2000 commercial software. According to the analysis produced by these two methods, the first connection failure in the roof was found at RTWC 35, which is located on the south side of the roof. If identical RTWCs were analyzed, RTWC 9 should have failed first, but due to the different degrees of stiffness and the load sharing among the trusses, RTWC 35 was, in fact, the first to fail. Figure 4.11 provides a comparison of the results from the two analysis methods. As is apparent from the figure, both numerical models indicate that the roof would begin to fail at a mean wind speed of 34 m/sec. However, with respect to the FEM results at a mean wind speed of 29 m/sec, the results estimated by the solution model were below the FEM results by a maximum of 30 %. The important output from the developed solution model is a determination of the failure speed for varying degrees of RTWC stiffness. This comparison thus demonstrates that the solution model estimates a failure speed similar to that calculated using FEM even though the solution model computational time is reduced by 15 times compared to the FEM. To get a sense of the variability of the failure wind speed with toe-nail connection characteristics, the roof was analyzed by considering the upper and lower bounds of the toe-nail connection curves obtained from the experimental results (Khan, 2012). The analysis indicates that by considering the upper and lower limits, the failure wind speed ranged between 27 m/sec and 39 m/sec.
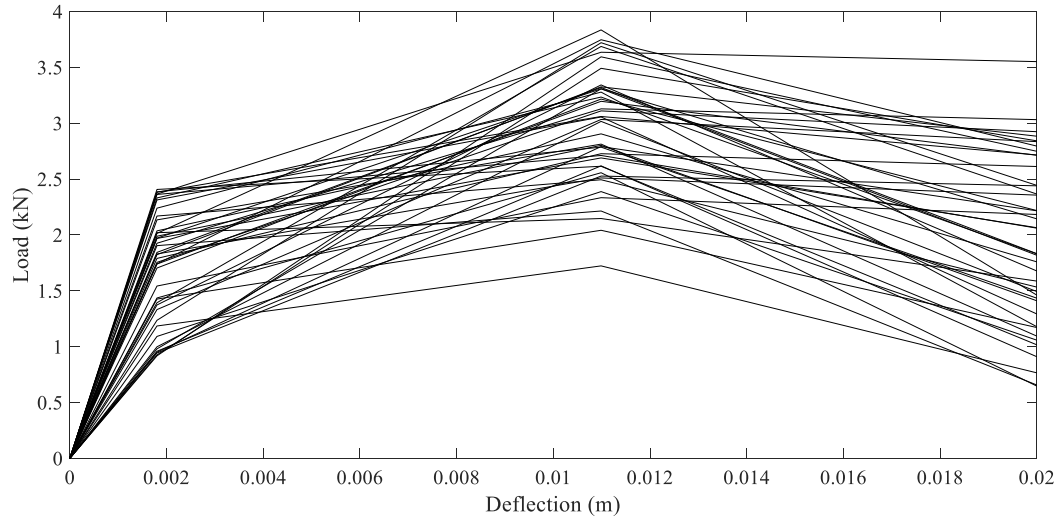
Figure 4.10: Forty-two random RTWC stiffness values used for comparing the solution model output with the FEM results.
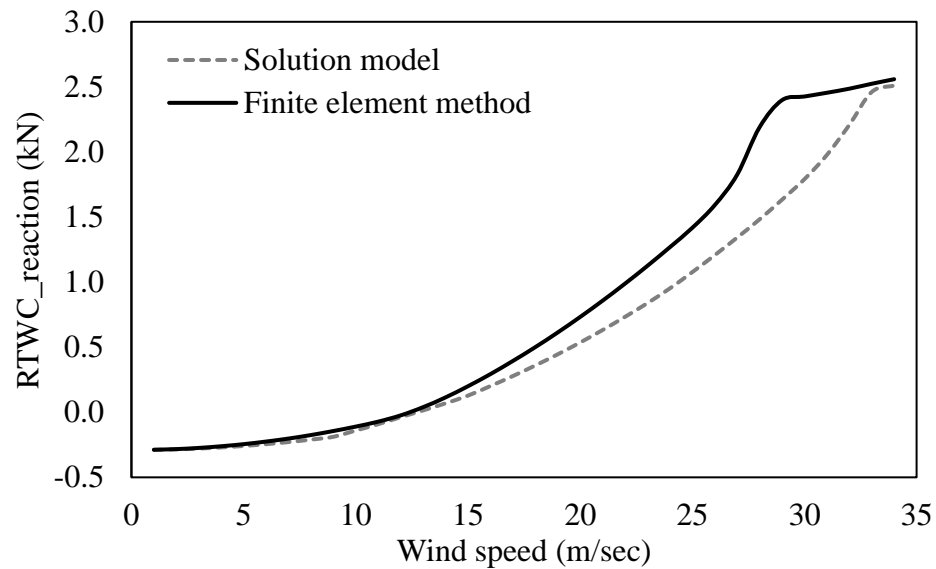
Figure 4.11: RTWC 35 reaction as calculated by the solution model and FEM.

4.4. Monte Carlo Simulation

The solution model discussed in the previous section was used for analyzing the gable house roof based on several random scenarios designed to facilitate an estimation of the

probability of roof failure. For each scenario, the analysis was performed randomly with a different degree of stiffness for each RTWC so that each RTWC also had its own an individual load-deflection curve. The pressure coefficients cited in NBCC (2010) were used for the application of the uplift wind pressure on the gable roof, and the pressure was also applied in quasi-static manner as randomly and deterministically.

4.4.1 Methodology

The methodology used for the Monte Carlo simulation is illustrated briefly as a flowchart in Figure 4.12. The simulation was performed in two steps. In the first step, the target output for each scenario is a determination of the mean wind speed at which the house roof failed. The failure of the roof is defined as the first connection that fails on the south side of the roof, where the uplift pressure exerts greater pressure intensity than on the north side. This study is based on the assumption that the failure of one connection is an indication of further failure in other connections, a mode of failure defined as the "zipper effect" (Gleason, 2009). The failure of the connection can be observed when the tension load applied in the connections exceeds the maximum capacity of the connection. Once the first step has been performed, a range of mean wind speeds is evaluated. This range is later used during the second step, which entails the selection of a number of mean wind speeds for other Monte Carlo simulations. For each selected wind speed, a number of scenarios are analyzed in order to assess the probability of roof failure at that selected speed. The final element is a fragility curve that is drawn as an illustration of the probability of roof failure with respect to mean wind speed. This curve is obtained for both random and deterministic uplift wind pressures.

4.4.2 Monte Carlo Simulation with Deterministic Uplift Wind Pressures

In these simulations, only the randomness of the RTWC stiffness is taken into consideration for the evaluations of the probability of roof failure under similar pressure coefficients. Using identical NBCC (2010) pressure coefficients as a deterministic value for each Monte Carlo scenario does not accurately represent the real situation. However, the reason for using the same pressure coefficients in the first Monte Carlo simulations is

to investigate the effects of varying degrees of RTWC stiffness on the behaviour of the roof.

The number of Monte Carlo scenarios used for this analysis was 10,000. To prove that employing 10,000 scenarios can provide a stable estimation of the probability of failure, Figure 4.13 illustrates the variation of the probability of failure with the number of Monte Carlo scenarios for a range of wind speeds. As shown, at 10,000 scenarios of Monte Carlo simulation, predictions of the probability of failure reach convergence. For each scenario of the 10,000 scenarios, the uplift wind pressure is applied in 50 incremental steps in a quasi-static manner, starting with the uplift pressure associated with a mean wind speed of 1 m/sec and then increasing up to the pressure associated with 50 m/sec. After the 10,000 scenarios have been processed, a variety of mean wind speeds are obtained within the minimum and maximum values of the speed range. For the simulation discussed here, a range of mean wind speeds were obtained: from 26 m/sec up to 38 m/sec. Figure 4.14 provides a histogram of the evaluation based on the failure wind speed: a normal distribution is fitted with a mean of 31 m/sec and a coefficient of variation of 0.063.
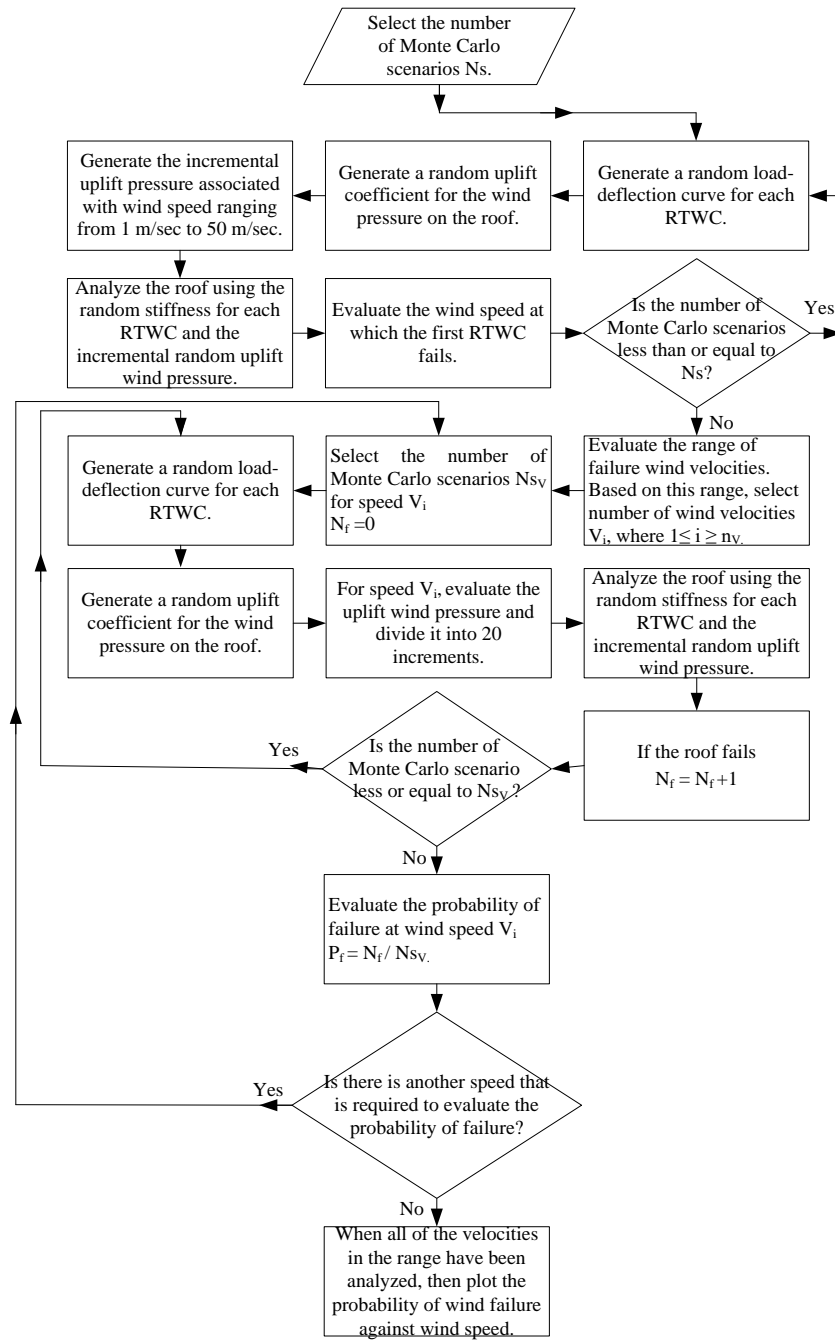
Figure 4.12: Flowchart of the Monte Carlo simulation.
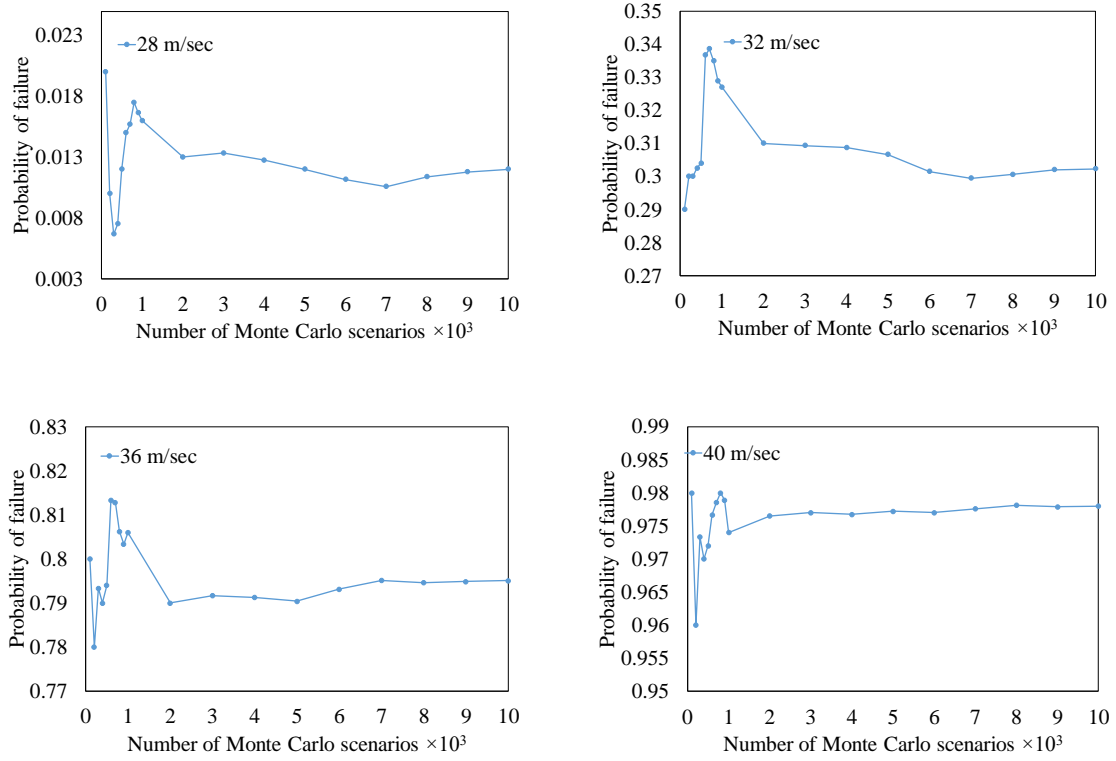
Figure 4.13: Estimates of the probability of failure for selected wind speeds.
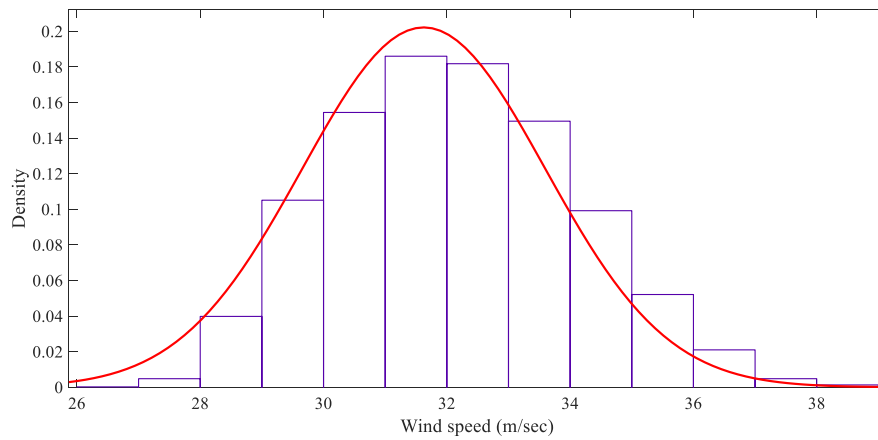
Figure 4.14: Histogram of the failure wind speeds based on a deterministic uplift pressure.

This range of speeds is examined later in order to evaluate the reliability of the gable roof, or the probability of failure, at each wind speed. The probability of failure is assessed from the results of the Monte Carlo simulation in which the mean wind speed is fixed for each simulation. This task involves the estimation of the probability of roof failure for six wind speeds: 26 m/sec, 28 m/sec, 30 m/sec, 32 m/sec, 35 m/sec, and 38 m/sec. For example, the probability of failure must be evaluated at a mean wind speed of V, and therefore, 10,000 scenarios are processed with the uplift wind pressure associated with a wind speed of V. The uplift wind pressure for each scenario should be applied incrementally, so the load is divided into 20 increments. The probability of failure is calculated as a ratio of the number of houses whose roof has failed during the application of a mean wind speed of V to the number of Monte Carlo scenarios, which is 10,000. Table 4.3 lists the probability of roof failure for each wind speed. Figure 4.15 illustrates the fragility curve for roofs with respect to wind speed.

Table 4.3: Reliability of gable house roofs with deterministic uplift pressure

Speed	Nf	Total scenarios	Probability of failure	Reliability
26	32	10000	0.0032	0.9968
28	1359	10000	0.1359	0.8641
30	4728	10000	0.4728	0.5272
32	8200	10000	0.82	0.18
35	9927	10000	0.9927	0.0073
38	10000	10000	1	0

4.4.3 Monte Carlo Simulation with Random Uplift Wind Pressures

In these simulations, two random variables are taken into consideration: the randomness of the RTWC load-deflection curve and the uplift wind pressure. Because of the uncertainty associated with wind pressure, a requirement for the fragility assessment is that the wind pressure value be applied randomly (Stewart et al., 2016). The uncertainty incorporated into the fragility estimation is further increased through the use of a random

wind load (Shanmugam, 2011). As discussed in section 4.2.1, random stiffness values for the RTWCs are generated using the beta distribution probability model, while uplift wind pressure amounts are generated using the normal distribution probabilistic model. The methodology outlined in the flowchart shown in Figure 4.12 was also used for investigating the factors discussed in this section.

The first simulation was conducted with 10,000 scenarios. In each scenario, the analysis was performed with randomly different degrees of stiffness for each RTWC, as well as different amounts of uplift wind pressure. The first step is to apply the uplift wind pressure for each scenario incrementally, starting with the pressure arising from a wind speed of 1 m/sec and ranging up to a pressure corresponding to a 50 m/sec wind speed. The output of the first simulation is a range of failure speeds, i.e., ones at which the gable roof could start to fail. This range consists of 10,000 failure speeds from a mean wind speed of 26 m/sec up to one of 46 m/sec. This range was plotted as a histogram of the failure speeds, as shown in Figure 4.16. A normal distribution is fitted to this histogram with a mean of 35 m/sec and a coefficient of variation of 0.082.
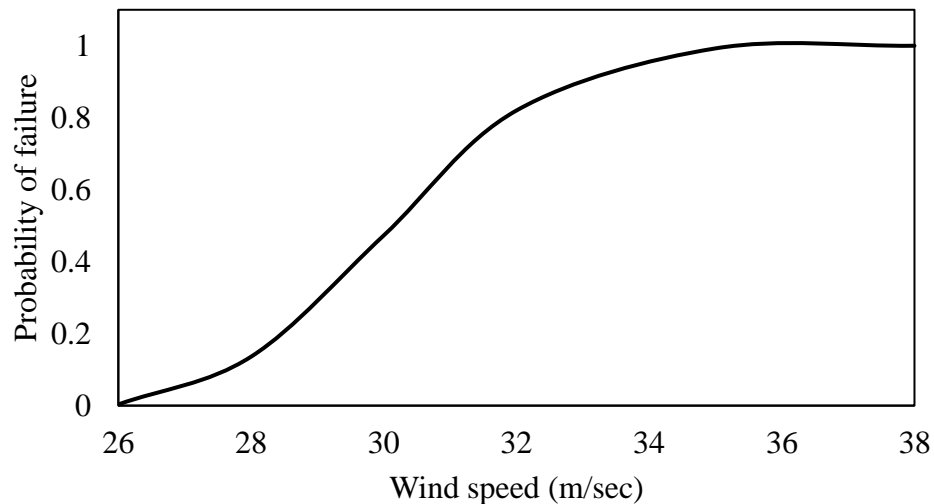
Figure 4.15: Probability of failure relative to wind speed.

To evaluate the required estimate of the probability of roof failure, a number of speeds are used for conducting other Monte Carlo simulations. The speeds selected start with a mean wind speed of 26 m/sec and increase by 2 m/sec increments up to 46 m/sec. For each of these speeds, 10,000 scenarios are analyzed in order to estimate the probability of failure at each of the 20 pressure increments. Table 4.4 lists these speeds with their corresponding probabilities of failure. The resultant probabilities of failure were plotted as the fragility curve shown in Figure 4.17.
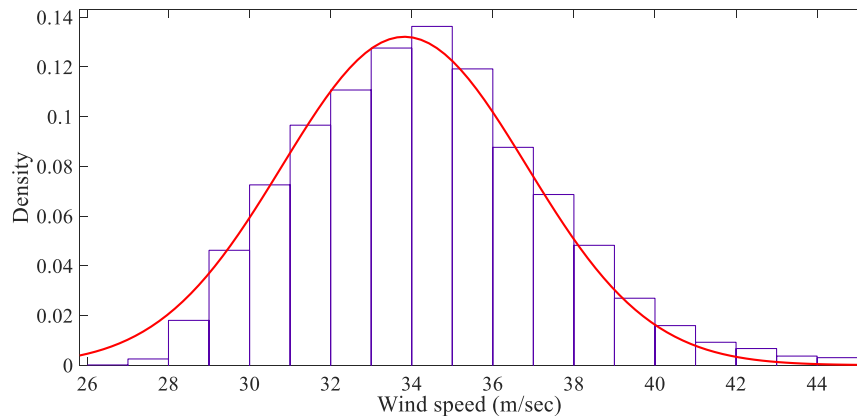
Figure 4.16: Histogram of the wind speeds leading to failure based on random amounts of uplift pressure.

Table 4.4: Reliability of the gable roof associated with random amounts of uplift pressure

Speed	Nf	Total scenarios	Probability of failure	Reliability
26	5	10000	0.0005	0.9995
28	120	10000	0.012	0.988
30	963	10000	0.0963	0.9037
32	3023	10000	0.3023	0.6977
34	5721	10000	0.5721	0.4279
36	7951	10000	0.7951	0.2049
38	9270	10000	0.927	0.073
40	9780	10000	0.978	0.022
42	9952	10000	0.9952	0.0048
44	9989	10000	0.9989	0.0011
46	9999	10000	0.9999	1E-04
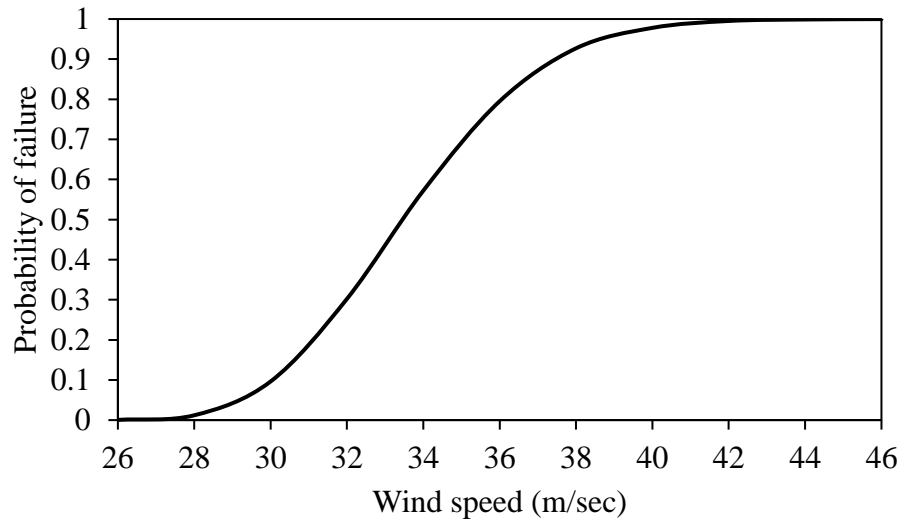
Figure 4.17: Fragility curve representing roof failure relative to random wind speeds.

4.5. Conclusion

This chapter has explained a new method for estimating the reliability of toe-nailed RTWCs in wooden houses under the effects of uplift wind loads. This estimation is applied to three-dimensional full-scale roofs utilizing a semi-analytical model that was previously developed. This analysis is a move ahead from previous literature which was confined to roof portions or cross-sections. Additionally, the chapter showed a procedure for the deduction of stiffness curves of RTWCs from experimental data using B-Spline fits.

The toe nailed RTWC is weak with respect to resisting applied tension loads, and the load-deflection curve of each RTWC differs from that of other RTWCs. This variability in the load-deflection curves causes some connections to be stronger than others in terms of transferring tension loads. As a result of this variability in the degree of RTWC stiffness, the wind speed at which the roof fails varies as well. The objective of this research was to assess the behaviour of typical light-frame wood houses based on consideration of the variable nature of the ability of the RTWCs to resist uplift wind

loads. This goal was achieved through an evaluation of the probability of roof failure with respect to a range of mean wind speeds. Probabilistic models of both the RTWCs and the uplift wind loads were designed and applied with Monte Carlo simulations in order to estimate RTWC reliability.

The development of the probabilistic model of toe-nailed RTWCs was based on the results of the experimental testing conducted by Khan (2012). Based on Khan's (2012) findings, random trilinear RTWC curves were generated using the beta distribution: Khan's (2012) experimental data were fitted to B-spline curves with eight control points for each RTWC. The second, fifth, and end control points are assumed to represent the yield, peak, and end curve points, respectively. Maximum likelihood estimation was utilized for evaluating the first and second shape parameters of the beta distribution for these three points. The probabilistic model of the uplift wind pressure coefficients was selected as an approximate normal distribution of the nominal values cited in NBCC (2010). This normal distribution probability model had already been used for estimating the wind uplift pressure coefficients based on ASCE 7-95 (Ellingwood and Tekie, 1999).

The RTWC reliability assessment is performed in two stages. In the first stage, the randomness associated with RTWC stiffness is included only in the Monte Carlo simulations that involve deterministic uplift wind loads. The results indicate that the mean failure wind speed ranges from 26 m/sec to 38 m/sec. The histogram plotted for this range and fitted to a normal distribution has a mean of 31 m/sec and a coefficient of variation of 0.063. The second stage incorporates into the Monte Carlo simulations both the randomness associated with the RTWC load-deflection curves and that related to the uplift wind loads. Failure speeds are evaluated, with the mean wind speed ranging from 26 m/sec up to 46 m/sec. The histogram plotted for this range and fitted to a normal distribution has a mean of 35 m/sec and a coefficient of variation of 0.082. In both stages, 10,000 scenarios are analyzed randomly using a simplified solution model in order to evaluate the mean wind speed at which the roof begins to fail. The failure of a roof is defined as the first connection failing, and connection failure is considered to have occurred when the tension load applied at the connection exceeds the maximum capacity

of that connection. The final step is an evaluation of the probability of roof failure at each wind speed in order to construct a fragility curve for each stage.

It was found that using the NBCC (2010) pressure coefficients as a deterministic value resulted in a smaller range of failure wind speeds than employing random pressure coefficients. When assessed with the deterministic pressure coefficients, the probability of roof failure was also greater than that produced using random pressure coefficients. This outcome was the result of increased uncertainty in the fragility estimation because of the inclusion of random wind loads (Shanmugam, 2011). A further finding is that above a mean wind speed of 30 m/sec, the probability of roof failure increases rapidly, with the probability of failure being evaluated, for example, as 0.3 at a mean wind speed of 32 m/sec. The first roof connections to fail were located primarily near the end gable truss or at the centre of the roof connections.

In summary, toe-nailed RTWCs constitute a leading cause of roof failure, especially above a mean wind speed of 32 m/sec. Devising a suitable retrofitting system for wooden houses built using these connections is therefore essential for reducing the probability of roof failure.

4.6. References

Benjamin, J. R., and Cornell, C. A. (2014), "Probability, statistics, and decision for civil engineers", Courier Corporation.

Canadian Commission on Building and Fire Codes, National Research Council Canada, and Institute for Research in Construction (Canada). User's Guide--NBC 2010: Structural Commentaries (Part 4 of Division B), National Research Council Canada, Ottawa, 2011.

Dao, T. N., and van de Lindt, John W. (2010), "Methodology for wind-driven rainwater intrusion fragilities for light-frame wood roof systems", *Journal of Structural Engineering*, **136**(6), 700-706.

Ellingwood, B. R., and Tekie, P. B. (1999), "Wind load statistics for probability-based structural design", *Journal of Structural Engineering*, **125**(4), 453-463.

Gleason, A. V. (2009), "Reliability of light frame roof systems subject to high winds", Master Thesis, Clemson University, Clemson, South Carolina, United States.

Guha, T.K. and Kopp, G.A. (2014), "Storm duration effects on roof-to-wall-connection failures of a residential, wood-frame, gable roof", *Journal of Wind Engineering and Industrial Aerodynamics*, **133**, 101-109.

He, J., Pan, F., Cai, C. S. (2017), "A review of wood-frame low-rise building performance study under hurricane winds", *Engineering Structures*, **141**, 512-529.

Khan, M. A. A. (2012), "Load-sharing of toe-nailed, roof-to-wall connections under extreme wind loads in wood-frame houses", Master Thesis, University of Western Ontario, London, ON, Canada.

Li, Y., and Ellingwood, B. R. (2006), "Hurricane damage to residential construction in the US: importance of uncertainty modeling in risk assessment", *Engineering Structures*, **28**(7), 1009-1018.

Mishra, S., Vanli, O. A., Alduse, B. P., Jung, S. (2017), "Hurricane loss estimation in wood-frame buildings using bayesian model updating: Assessing uncertainty in fragility and reliability analyses", *Engineering Structures*, **135**, 81-94.

Morrison, M. J., Henderson, D. J. and Kopp, G. A. (2012), "The response of a wood-frame, gable roof to fluctuating wind loads", *Engineering Structures*, **41**, 498-509.

Padmanabhan, D., Agarwal, H., Renaud, J. E., and Batill, S. M. (2006), "A study using monte carlo simulation for failure probability calculation in reliability-based optimization", *Optimization and Engineering*, **7**(3), 297-316.

Piegl, L. A., and Tiller, W. (1997), "The NURBS book", 2nd ed., New York, Berlin, Springer.

Reed, T. D., Rosowsky, D. V. and Schiff, S. D. (1997), "Uplift capacity of light-frame rafter to top plate connections", *Journal of Architectural Engineering*, **3**(4), 156-163.

Rosowsky, D. V., Yu, G., Bulleit, W. M. (2005), "Reliability of light-frame wall systems subject to combined axial and transverse loads", *Journal of Structural Engineering*, **131**(9), 1444-1455.

Rosowsky, D. V., and Cheng, N. (1999), "Reliability of light-frame roofs in high-wind regions. I: Wind loads", *Journal of Structural Engineering*, **125**(7), 725-733.

Rosowsky, D. V., and Cheng, N. (1999), "Reliability of light-frame roofs in high-wind regions. II: Reliability analysis", *Journal of Structural Engineering*, **125**(7), 734-739.

Shanmugam, B., Nielson, B. G., and Prevatt, D. O. (2009), "Statistical and analytical models for roof components in existing light-framed wood structures", *Engineering Structures*, **31**(11), 2607-2616.

Shanmugam, B. (2011), "Probabilistic assessment of roof uplift capacities in low-rise residential construction", PhD thesis, Clemson University, Clemson, South Carolina, United States.

Stewart, M. G., Ryan, P. C., Henderson, D. J., and Ginger, J. D. (2016), "Fragility analysis of roof damage to industrial buildings subject to extreme wind loading in non-cyclonic regions", *Engineering Structures*, **128**, 333-343.

Standohar-Alfano, C. D. (2016), "Damage analysis and mitigation for wood-frame structures subjected to tornado loading", PhD thesis, Colorado State University, Fort Collins, Colorado, United States.

Standohar-Alfano C.D, van de Lindt, John W, Ellingwood B.R. (2017), "Vertical Load Path Failure Risk Analysis of Residential Wood-Frame Construction in Tornadoes", *Journal of Structural Engineering*,**143**(7), 04017045.

van de Lindt, John W, Pei, S., Dao, T., Graettinger, A., Prevatt, D. O., Gupta, R., and Coulbourne, W. (2013), "Dual-objective-based tornado design philosophy", *Journal of Structural Engineering*, **139**(2), 251-263.

Wang, W., and Eamon, C. D. (2013), "Load path uncertainty in a wood structure and the effect on structural reliability", *Engineering Structures*, **56**, 889-896.

Chapter 5

5 Nonlinear Modelling of a Retrofitted Light-Frame Wood Structure

5.1 Introduction

Light-frame wood houses, especially those located in hurricane-prone areas, have the potential to be seriously damaged (Li and Ellingwood, 2006). One form of this damage is due primarily to the wind uplift forces generated on the roofs of wooden houses. This wind uplift force, or suction pressure, tends to detach the roof trusses from the walls, due to the failure of the wood connections to absorb the tension forces created by such pressure. A wooden roof skeleton contains two critical types of wood connections: roof-to-wall connections (RTWCs) and sheathing-to-truss connections (STTCs) (Jacklin et al., 2014). These connections resist suction pressure through their withdrawal capacity. Datin et al., (2008) defined four failure mechanisms associated with toe-nails: pull-through, withdrawal, partial withdrawal, and board split. Pull-through occurs especially at STTCs when the nail stays attached to the truss. The second and third mechanisms take place at RTWCs where the nails are no longer embedded in the top plate members. The final failure mechanism happens when wood members surrounding the nails rupture.

After Hurricane Andrew in 1992, to reduce the effects of uplift wind loads, houses were built using more sophisticated construction methods, such as utilizing hurricane straps for RTWCs rather than toe-nails (Datin et al., 2008). Current design codes for wood houses include a basic requirement for protection from wind damage. However, some existing houses that were built according to previous code versions are vulnerable because the stipulations in those codes provide only minimal protection. The Federal Emergency Management Agency (FEMA), for example, does not accept the use of toe-nail connections for resisting uplift wind loads (Kapur et al., 2010). As a result, houses built in Florida before 1994 are vulnerable because of their limited ability to resist uplift wind loads; vulnerability that arises from the inadequacy of the wood connections permitted by pre-1994 codes (Prevatt et al., 2014).

Internal retrofit techniques, such as hurricane straps, are costly and difficult to apply due to obstructions created by non-structural elements, such as soffits, that cover toe-nailed RTWCs (Kapur et al., 2010). Another retrofit technique is to apply external strengthening such as cables anchored to the ground. The advantage of this kind of external technique is that it reduces possible toe-nail failure and creates an additional path for the load, rather than having it transferred through the RTWCs. This external retrofitting technique does not require any expensive alterations in an existing house and is utilized only in the case of warning of highly intense winds. Another advantage of retrofitting houses, whether internally or externally, is lower insurance premiums. Well-retrofitted houses located in hurricane-prone areas are subject to reduced insurance premiums, based on improvements made following hurricane damage (Kapur et al., 2010).

Datin et al., (2008) published a technical report about destructive tests for existing light-frame wood houses built prior to 30 years ago. The instrumentation for these destructive tests involved the use of a suction chamber and load tree. The suction chamber was applied to the top of the houses to measure STTC capacity. The load tree was employed for evaluating the capacity of existing RTWCs. A comparison of each test with and without the proposed retrofit revealed an increase in connection capacity following the retrofit. All of the retrofitting strategies used by Datin et al., (2008) were directed at the internal strengthening of existing connections. They retrofitted STTCs, for example, by applying closed-cell polyurethane foam (ccSPF) adhesive beneath the sheathings where this material was used as insulation, while RTWCs were retrofitted with the use of metal straps or adhesive blocks, such as a piece of wood, that glued the sheathing and the end trusses to the top plate members. In a similar study (Datin et al., 2011), the authors concluded that the roof sheathings retrofitted with ccSPF could increase withdrawal resistance by 2.5 to 3 times; however, water leakage would reduce the strength of the bond between the wood and the ccSPF by 54 % (Prevatt et al., 2014).

Kapur et al., (2010) suggested retrofitting strategies for wood houses located in North American hurricane-prone areas, as defined in ASCE/SEI 7-05 (2005), especially on the Atlantic and Gulf of Mexico coasts, where the wind speeds of 3-sec gusts can exceed 40 m/sec. The retrofitting strategies defined by Kapur et al., (2010) are divided into three

types of packages: basic, intermediate, and advanced. A basic retrofitting package involves removing the roof covering, strengthening STTCs, strengthening ventilation (soffits), and strengthening end gable wall overhangs. The intermediate retrofitting package is focussed only on openings, such as windows and doors. With this intermediate package, the openings should be capable of sustaining wind pressure through the use of appropriate doors or windows that would prevent the openings from failing during hurricanes; if a failure occurs, both the internal pressure inside the house and the total uplift forces increase. The advanced retrofitting package is aimed only at providing a continuous load path from the roof of the house to its foundation. A continuous load path is achieved through the strengthening of the RTWCs with the use of hurricane clips. Kapur et al., (2010) also reported that the advanced type of retrofitting cannot be implemented unless the basic and intermediate packages have already been applied. In other words, providing a continuous load path is pointless unless the openings and sheathings have first been secured.

In general, a hurricane strap offers more uplift resistance than toe-nailed connections. Yazdani et al., (2005), for example, designed a room that can offer a safe shelter from hurricanes or tornados. In their design, which provides sufficient wind uplift resistance, Yazdani et al., (2005) installed hurricane straps as RTWCs. Alldredge et al., (2012) tested RTWC capacity by applying a polymer coat (polyurea) to toe-nailed and hurricane tie connections, and they found that this process increased uplift resistance under a tension load by two to four times. Canbek et al., (2011) developed another retrofit technique for strengthening RTWCs against uplift wind loads through the use of a fibre-reinforced polymer (FRP). They used epoxy resin to bond FRP composites around the RTWCs. Their system offers advantages over hurricane straps because the uplift capacity of RTWCs retrofitted with FRP ties is 65 % greater than that of RTWCs retrofitted with hurricane straps. Compared with using hurricane straps that require nail penetration, a further benefit of retrofitting RTWCs with FRP ties is that they do not destroy the wood material. The deformation of RTWCs retrofitted with FRP ties was also less than that associated with RTWCs retrofitted with hurricane straps, which translates into reduced water intrusion from the driven rain that accompanies a hurricane.

Several patents have been issued for external retrofit techniques for houses and mobile homes. Small (1904), for example, invented a roof-anchoring system for reducing damage from severe wind storms. His system consists of base plates with grooves anchored on top of a gable or hip roof. Several cables are attached to these grooves and then anchored to the foundation. Anderson et al., (1973) registered a patent for a method of securing portable structures, such as mobile homes, with the use of pretension external cables, which are held on top of such structures and then anchored to the ground. These external cables are secured by a bracket, so as not to damage the structure. Phillips et al., (1995) developed and patented a technique for anchoring portable structures, such as mobile homes, with the use of threaded rods connecting the roof to a concrete base. Bimberg and Bimberg (1997) patented a cable system for reinforcing houses exposed to severe wind storms. Cables are applied in two directions on the top of the house through the use of bearing plates installed over the sheathings. The bearing plates are positioned at the intersection of the roof cables and feature a rubber base in order to reduce friction. The top cables with the bearing plates are connected to the foundation by external cables fitted with turnbuckles for adjusting the tension. Cornett et al., (2000), Pittman (2004), Pierce and Worth (2005), and Lindstrom and Worth (2008) created generally similar strategies for supporting house roofs with external cables, but each patent details a different configuration.

Reinhold (2003) conducted destructive testing as a means of examining the capacity of an externally retrofitted light-frame wood house. The house tested without retrofitting had a suitable load path, due to the use of hurricane straps as RTWCs. The retrofit system consisted of polyester straps and a tightening device, referred to as a Hurricane Harness (http://hurricaneharness.com). The polyester straps were installed at the top of the house and anchored to the foundation. The uplift wind load was simulated by a crane-held load tree connected to the roof of the house. Load cells were installed at the crane and at the straps, in order to measure the applied uplift load and the capacity of each strap. It was concluded that at the stage when the RTWC failed, the applied uplift load was resisted by the retrofit system, which created an additional load path from the roof to the foundation; this system would increase resistance so that the structure would be able to withstand wind speeds up to 20 % greater.

Prevatt (2007) discussed a number of retrofit techniques that could prevent failure or could increase resistance to uplift wind loads, such as a strong tie rod system. His rod system is basically a threaded rod connecting the roof of the house to a foundation anchor, which provides an additional load path during high uplift wind loads. From another perspective, at the Wall of Wind (WOW) facility, Leatherman et al., (2007) investigated the alteration of a gable roof edge in order to reduce suction pressure. Blessing et al., (2009) conducted an experiment at WOW in which they observed the reduction in the uplift wind load associated with the modification of the roof edges of a full-scale house with a flat roof. The modification included the installation of approximately 15 cm of a metallic sheet, such as a parapet wall.

This chapter focuses on an external retrofit system previously developed and tested at the University of Western Ontario (UWO) by Jacklin (2013). This external retrofitting consists of bearing cables, external cables, and rigid bars. The bearing cables are installed on the roof and attached to rigid bars in the roof edge, which are, in turn, connected to external cables supported by micropiles permanently embedded in the ground. Turnbuckles are used for pretensioning the external cables. Previous numerical and experimental studies conducted at UWO are introduced. The objective of this chapter is to develop a semi-analytical solution model able to predict the nonlinear behaviour of a roof with a retrofit system under uplift wind pressures.

5.2   Previous Studies at UWO

Previous work underlying this research has been focussed on the finite element modelling of light-frame wood houses as a means of estimating predicted RTWC deflection under a simulated wind load (Dessouki, 2010; Jacklin, 2013). Once researchers had validated the numerical model, it was extended to include the modelling of a suitable retrofit system, which was assessed through parametric studies in order to determine the optimal design.

Dessouki (2010) developed a three-dimensional finite element model for simulating a gable roof house subjected to a wind load. The house was tested at the Insurance Research Lab for Better Homes (IRLBH) located at the University of Western Ontario under a simulated wind load provided by a wind tunnel study (Morrison et al., 2012). The

finite element model was created using SAP2000 commercial software, in which the three-dimensional frame element was used for modelling the truss members, stud walls, connecting beams between the trusses, and the top plate of the walls, while the shell element was used for modelling the plywood sheathings. Based on the results of this research, the critical weak joints with respect to resisting the uplift wind load were found to be the toe-nailed RTWCs, which were modelled as nonlinear spring elements with a load-displacement curve adapted from Reed et al., (1997).

Addressing the problem from another perspective, Dessouki (2010) developed a new retrofit system for strengthening the response of house roofs to uplift wind loads. As shown in Figure 5.1, this system consisted of a two-dimensional steel wire net installed on the top of the house. Carbon fibre rods were connected to the wire net on four sides to provide a uniform distributed load on the wire net and to reduce the number of external cables connected between the rods and piles anchored in the foundation. When hurricane warnings are issued, this system can be easily installed to provide an additional load path. The numerical model was extended to simulate the retrofit system under a uniform suction pressure of 2 kN/m^2. The wire net and the external cables were modelled as a nonlinear cable element under their own weight and strain loading, and the carbon fibre rods were modelled as a three-dimensional frame element.
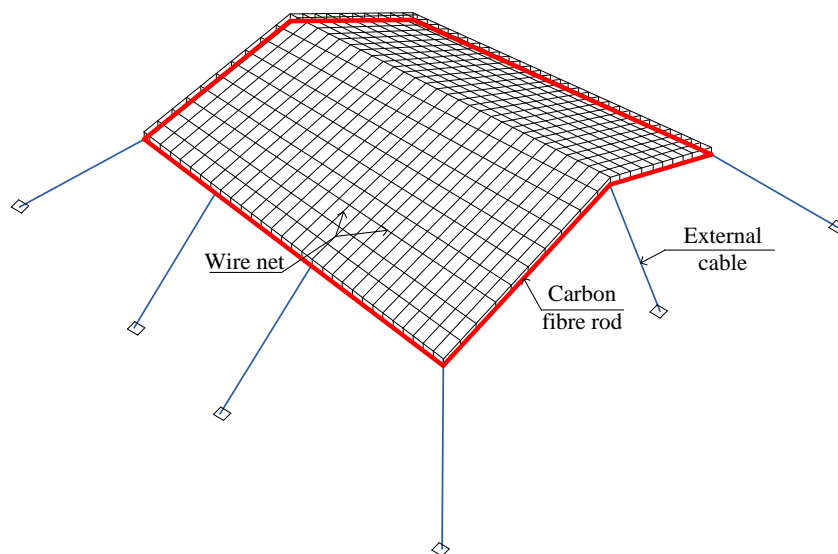
Figure 5.1: Retrofit system proposed by Dessouki (2010).

Jacklin (2013) modified the retrofit system introduced by Dessouki (2010). As shown in Figure 5.2, the modified retrofit system consists of steel bearing cables resting on the top skin of the roof. The bearing cables are connected to horizontal rigid aluminum bars along their edge. The purpose of the rigid bars is to create a uniform load at the bearing cables and to reduce the number of external steel cables that are connected between these bars and permanent small piles anchored to the ground around the perimeter of the structure. The external cables are stretched by applying a prescribed prestressing force through a special loading system, such as turnbuckles. The retrofit system would be designed so that the cables could be kept folded during normal wind conditions, thus avoiding distortion of the style and aesthetics of the house. The installation of the retrofit system would take place when advance hurricane warnings are issued.
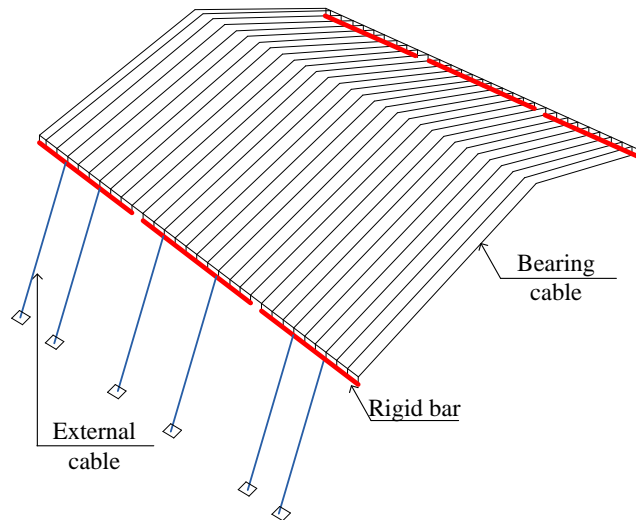
Figure 5.2: Retrofit system proposed by Jacklin (2013).

Jacklin (2013) conducted experimental testing at the structural laboratory at University of Western Ontario. The aim of his experiment was to confirm the efficiency of his proposed retrofitting system with respect to reducing the effects of uplift wind loads. As shown in Figure 5.3, the proposed retrofitting system was simply a series of cables installed at the top of the house and anchored to the foundation. In the experimental prototype, a segment of a full-scale gable roof house was tested under static load. This

prototype consisted of three typical Howe trusses spanning 9 m and spaced 0.6 m apart, with a roof slope of 1:3. The uplift load was created experimentally using two hydraulic jacks located under the prototype exactly at the middle of the vertical webs so that the uplift load would be distributed into six-point loads. The experiment was conducted in three stages. The first stage was to test the prototype without the retrofit system in order to establish how the roof system would react to the uplift load. In the second stage, a new prototype was constructed in the same way as in the first stage, but with the use of the proposed retrofit system. The final stage of the testing took place following the failure of the prototype during the first stage: the retrofit system was employed for the replacement of the damaged connections.
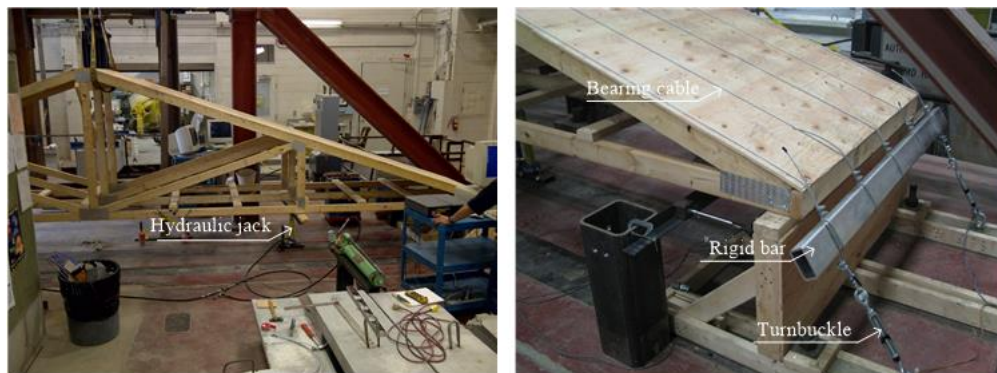
Figure 5.3: Experimental setup for the structural tests prepared by Jacklin (2013).

The final experiment conducted by Rosenkrantz (2017) was the destructive testing of a small-scale light-frame wood house. The objective was to assess the behaviour of external strengthening (i.e., retrofitting) with respect to the roofs of existing light-frame houses. Two prototypes of small wood structures were built as subjects for the evaluation of the capacity of toe-nail connections against a real wind load generated from the Wind Engineering, Energy and Environment (WindEEE) Dome at the University of Western Ontario. This experiment was conducted in three separate stages: a load control test, a displacement control test, and a retrofitted control test. The plan of the prototype as

shown in Figure 5.4 was 3 m by 3 m with a wall height of 0.9 m. the slope of the roof was chosen to be 1:4. The experimental prototypes contained four simply supported Howe trusses spaced 1.0 m apart. The toe-nailed RTWCs were scaled down to consist of 3-2D common nails (1 in. long). Figure 5.5 illustrates the components of the retrofit system.

Figure 5.4: Experimental prototype prepared by Rosenkrantz (2017).

Figure 5.5: Retrofitted control test setup prepared by Rosenkrantz (2017).

5.3 Solution model

The solution model presented in this chapter represents a simplified solution, which was validated against the structural laboratory experiment and the WindEEE experiment. This simplified solution employed a semi-analytical solution that represents an extension of the work described in Chapter 3 related to determining the load sharing between the trusses and the retrofitted system. Once the load sharing among the retrofitted roof components had been evaluated, the results could be used in conjunction with the finite element modelling (FEM) for the analysis of the roof system. The FEM procedure used in the study described in this chapter comprised a combination of frame elements and cable elements. The representation of the retrofitting system as cables holding the roof secure from wind suction pressures meant that two nonlinear elements would be involved in the solution model: RTWCs and cable elements. In other words, the simplified solution analyzes the entire roof as an approximate two-dimensional analysis rather than a three-dimensional finite element modelling (FEM) based on the use of the equivalent load sharing.

5.3.1 Semi-Analytical Solution

The semi-analytical solution discussed in this chapter was previously implemented for analyzing a gable roof house, as described in Chapter 3. The results of this gable roof analysis using this simplified solution agreed well with the predictions produced by the three-dimensional nonlinear FEM (Enajar et al., 2019) with respect to RTWC reactions as well as findings of the experimental testing conducted at IRLBH (Morrison et al., 2012) with respect to RTWC deflection. This semi-analytical solution involved the application of statically indeterminate slope deflection equations that include shear deformation so that the entire set of gable roof trusses was analyzed as a series of beams on an elastic foundation. The cross section of these beams should not flexible to account for the load sharing among the trusses, due to the short spacing between the trusses compared to their depth. According to the *Wood Design Manual* (WDM, 2010), the spacing between trusses varies from 16 in. to 48 in., which are considered short lengths compared to the depth of the trusses. The cross section of a beam is therefore defined as the cross members between the trusses, the facia, and the sheathing, all lumped together. On the

other hand, if the diaphragm between the trusses is assumed to be flexible, the load sharing for each truss would simply be the result of the tributary area loads, and the stiffness of the trusses would have no effect. The tributary area loads create an overestimation of the reactions in the middle truss connections and an underestimation of the reactions in the gable end truss connections. Each individual truss is modelled as a linear spring, and the stiffness of these linear springs is calculated as the ratio of the unit load to the deflection of the top truss. For establishing the stiffness of the trusses, it is important to include the stiffness of the RTWC based on consideration of the load-deflection curve as a linear spring. The model can therefore be analyzed as a statically indeterminate beam that has spring supports under flexural and shear deformation. The slope-deflection method combined with the Timoshenko beam theory is a suitable approach for this task (Rojas, 2012).

5.3.2 Methodology

The methodology for analyzing the retrofitted house is derived from a load sharing philosophy similar to the one used for a house without the retrofit system. The only difference is that, in the case of the retrofitted house, the uplift wind load is transferred based on the stiffness of the supporting trusses and the retrofitted system. As illustrated in Figure 5.6, the retrofitted system includes three main components: bearing cables, external cables, and rigid bars. The bearing cables are attached to the top of the house with the goal of holding the house down during a severe wind storm by means of the pretension forces applied at the external cables. The role of the rigid bars is to distribute the pretension forces equally to each bearing cable. Figure 5.6 depicts the sample retrofitted small-scale gable roof house used for the WindEEE experiment. As can be seen in the figure, each truss is supported by one bearing cable as well as by another bearing cable between the trusses. In two-dimensional analysis terms, there are thus two main types of supporting segments, designated A segments and B segments. An A segment represents a bearing cable on top of a truss, and a B segment represents a bearing cable between the trusses. Based on the Figure 5.6 example, there are four typical A segments and three typical B segments.
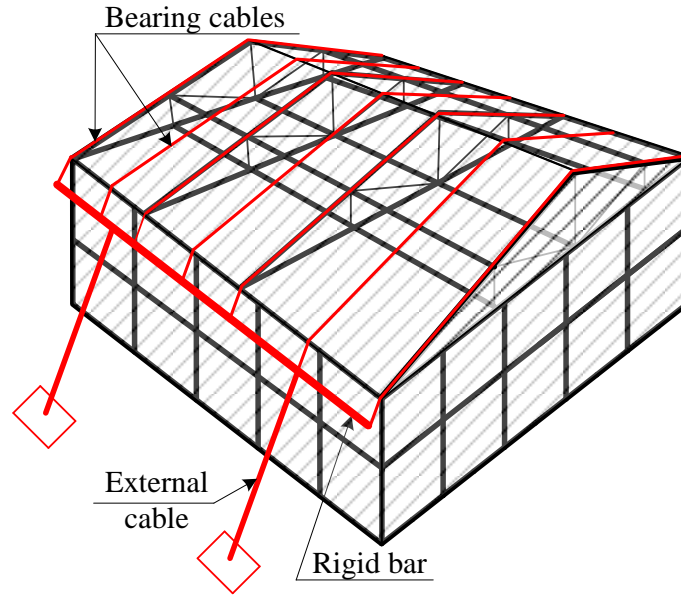
Figure 5.6: Example of a retrofitted gable roof house.

The analysis process begins with the use of the finite element model illustrated in Figure 5.7 for an evaluation of the initial tension force at each bearing cable. Figure 5.7 illustrates one side of the modelled external cables connected to the bearing cables with a rigid bar. The bearing and external cables are modelled as cable elements, and the rigid bars are modelled as frame elements. To assess the initial tension forces at the bearing cables, the tension forces that can be observed in Figure 5.7 at the bearing cables are resolved in a later step that also includes the calculation of the inclination of the external cables and the roof slope.
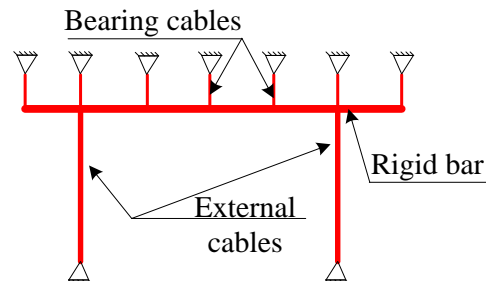
Figure 5.7: Distribution of the pretension forces at the external cables in the direction of the bearing cables.

Once the initial tension force at each bearing cable has been calculated, based on the layout shown in Figure 5.8, the initial stiffness of the A and B segments can be evaluated as the ratio of the unit load to the deflection of the top segment. It is important for the first iteration to include the initial RTWC tangent stiffness as a linear spring when the stiffness of the A segments is calculated. In the first iteration and to establish the load distributed on each segment, the uplift wind pressure is considered to be transferred to each supporting segment based on its initial stiffness value, according to the concept of a beam on an elastic foundation, as illustrated in Figure 5.9. The load distributed at each segment is used for the required evaluation of the RTWC reaction. The RTWC load-deflection curve is divided into a number of increments, each of which has a different RTWC stiffness value based on the RTWC reaction. In the second iteration, new RTWC stiffness values are calculated based on the level of the load observed at each RTWC. The new RTWC stiffness values are then used for evaluating the stiffness of the second A segment, and a new calculation of the load sharing at each segment is performed in order to measure the second RTWC reaction. These iterations are repeated until the RTWC reactions reach convergence and no change is observed in them. At this final stage, the tension at the external cable is calculated along with the RTWC deflection, based on the constitutive relation of the RTWCs. Figure 5.10 sets out the general strategy underlying the methodology for analyzing the retrofitted house.
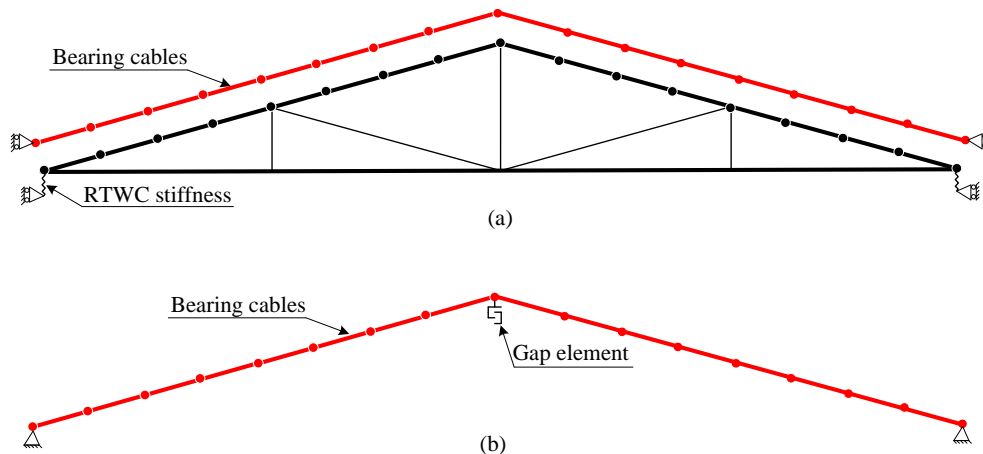
Figure 5.8: Support segments: (a) an A segment, which is a truss with bearing cable; (b) a B segment, which is a bearing cable only.
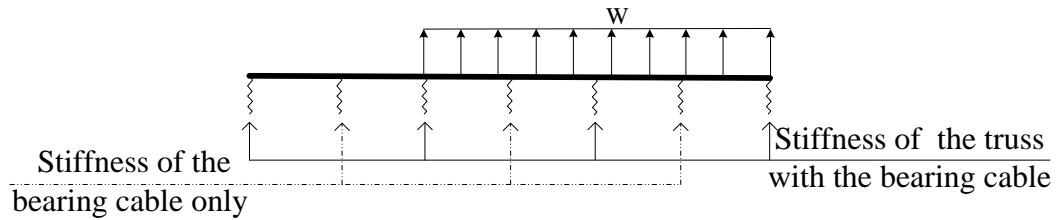
Figure 5.9: Beam on an elastic foundation.

5.3.3 Cable Elements

In general, FEM involves three categories of nonlinearity: material, gap, and geometric (Cook et al., 2002). Geometric nonlinearity implies elements associated with substantial deformation such that the stiffness matrix must be rewritten with respect to the shape of the new element. A cable element can be considered a type of geometric nonlinearity due to its flexibility under applied loads (Papadopoulos et al., 2008). Cable elements carry only tension forces, which means that the moment and shear at each point on the cable are both zero.

Papadopoulos et al., (2008); Torkamani and Shieh (2011); and Coarita and Flores (2015) all stated that the stiffness matrix of a cable element is a superposition of two main matrices: the elastic stiffness matrix (linear) and the geometric stiffness matrix (nonlinear). However, higher order stiffness matrices are also included, but they are neglected in this study for the sake of simplicity. Elastic stiffness is a well-known bar stiffness element in the case of the axial load of a member, as expressed in Equation (5.1), where A is the cable cross section area, L_0 is the initial cable length without deformation, and E is the cable modulus of elasticity. Figure 5.11 illustrates a deformed cable element with respect to the x, z axes under the effect of tension force F and the lateral forces P_n and P_f at nodes n (near) and f (far), respectively:

$$k_{\text{elastic}} = \frac{AE}{L_0}\begin{bmatrix} 1 & -1 \\ -1 & 1 \end{bmatrix}$$

(5.1)
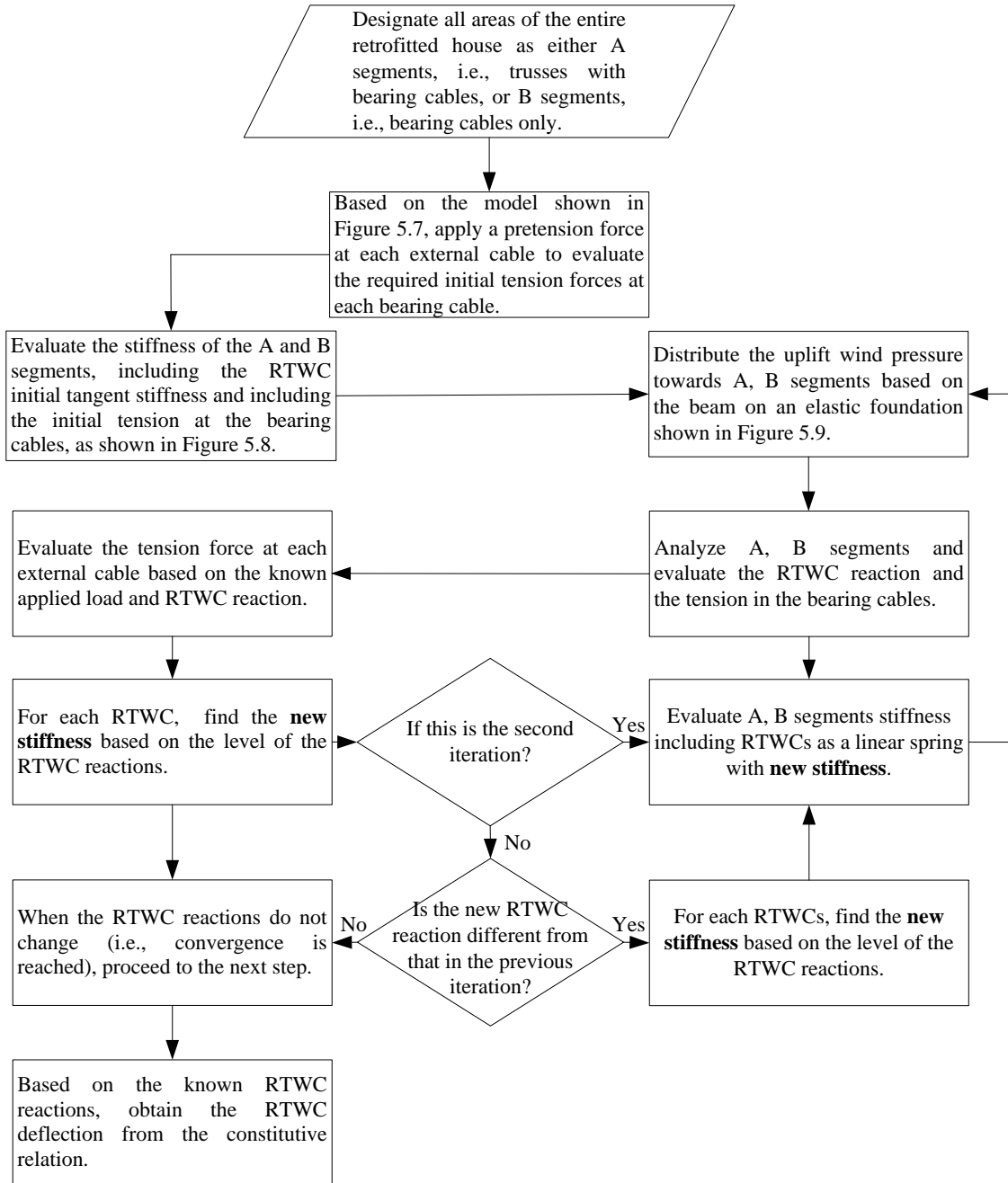
Figure 5.10: Flowchart of the steps in the determination of the RTWC reactions and the external cable tension.

Wilson (2002) derived the geometric stiffness matrix of a cable element from the lateral forces P_n and P_f by taking the moment around node n, where L is defined as the deformed cable length:

$$P_f \times L - F \times V_f + F \times V_n = 0$$

$$\Rightarrow P_f = \frac{F}{L}(V_f - V_n) \qquad (5.2)$$
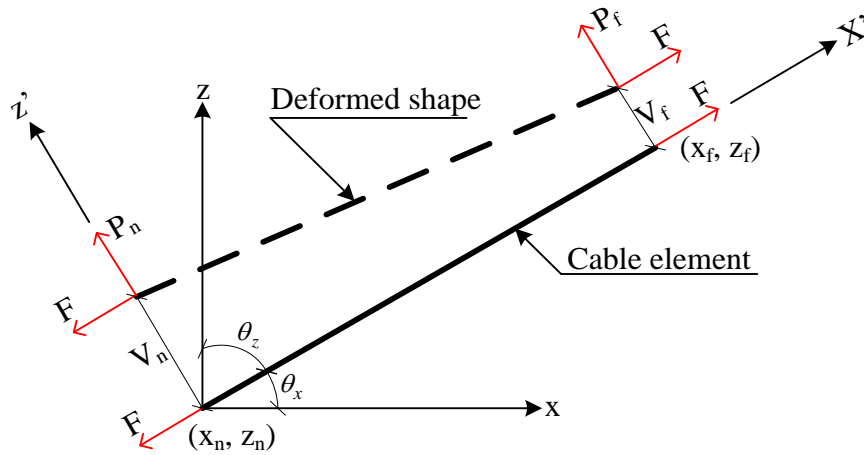
Figure 5.11: Cable element.

If the summation of the forces perpendicular to the cable element is taken:

$$P_f + P_n = 0$$

$$\Rightarrow P_n = \frac{F}{L}(V_n - V_f) \qquad (5.3)$$

Equations (5.2) and (5.3) can be written in matrix form as follows:

$$\begin{bmatrix} P_f \\ P_n \end{bmatrix} = \frac{F}{L} \begin{bmatrix} 1 & -1 \\ -1 & 1 \end{bmatrix} \begin{bmatrix} V_f \\ V_n \end{bmatrix} \qquad (5.4)$$

From Equation (5.4), the geometric stiffness matrix can be written as follows:

$$k_{geometric} = \frac{F}{L}\begin{bmatrix} 1 & -1 \\ -1 & 1 \end{bmatrix}$$

(5.5)

The matrices in both Equation (5.1) and Equation (5.5) are in local axes, where the elastic stiffness matrix represents the stiffness in the direction of the cable element, and the geometric stiffness matrix represents the lateral stiffness of the cable. Equation (5.6) shows the superposition of both matrices in local axes:

$$k_{cable} = k_{elastic} + k_{geometric} = \frac{AE}{L_0}\begin{bmatrix} \overset{x'}{1} & \overset{z'}{0} & \overset{x'}{-1} & \overset{z'}{0} \\ 0 & 0 & 0 & 0 \\ -1 & 0 & 1 & 0 \\ 0 & 0 & 0 & 0 \end{bmatrix}\begin{matrix} x' \\ z' \\ x' \\ z' \end{matrix} + \frac{F}{L}\begin{bmatrix} \overset{x'}{0} & \overset{z'}{0} & \overset{x'}{0} & \overset{z'}{0} \\ 0 & 1 & 0 & -1 \\ 0 & 0 & 0 & 0 \\ 0 & -1 & 0 & 1 \end{bmatrix}\begin{matrix} x' \\ z' \\ x' \\ z' \end{matrix}$$

(5.6)

The stiffness matrix in global axes can be found with the use of the transformation matrix T, as follows:

$$T = \begin{bmatrix} \lambda_x & -\lambda_z & 0 & 0 \\ \lambda_z & \lambda_x & 0 & 0 \\ 0 & 0 & \lambda_x & -\lambda_z \\ 0 & 0 & \lambda_z & \lambda_x \end{bmatrix}$$

(5.7)

where the direction cosines $\lambda_x = Cos\theta_x = \dfrac{x_f - x_n}{L}$ and $\lambda_z = Cos\theta_z = \dfrac{z_f - z_n}{L}$, and the subscripts f, n refer to far and near nodes, respectively:

$$k_{cable} = T^T k_{elastic} T + T^T k_{geometric} T$$

$$k_{cable} = \frac{AE}{L_0}\begin{bmatrix} \overset{x}{\lambda_x^2} & \overset{z}{\lambda_x\lambda_z} & \overset{x}{-\lambda_x^2} & \overset{z}{-\lambda_x\lambda_z} \\ \lambda_x\lambda_z & \lambda_z^2 & -\lambda_x\lambda_z & -\lambda_z^2 \\ -\lambda_x^2 & -\lambda_x\lambda_z & \lambda_x^2 & \lambda_x\lambda_z \\ -\lambda_x\lambda_z & -\lambda_z^2 & \lambda_x\lambda_z & \lambda_z^2 \end{bmatrix}\begin{matrix} x \\ z \\ x \\ z \end{matrix} + \frac{F}{L}\begin{bmatrix} \overset{x}{\lambda_z^2} & \overset{z}{-\lambda_x\lambda_z} & \overset{x}{-\lambda_z^2} & \overset{z}{\lambda_x\lambda_z} \\ -\lambda_x\lambda_z & \lambda_x^2 & \lambda_x\lambda_z & -\lambda_x^2 \\ -\lambda_z^2 & \lambda_x\lambda_z & \lambda_z^2 & -\lambda_x\lambda_z \\ \lambda_x\lambda_z & -\lambda_x^2 & -\lambda_x\lambda_z & \lambda_x^2 \end{bmatrix}\begin{matrix} x \\ z \\ x \\ z \end{matrix}$$

(5.8)

The analysis of the cables using the global stiffness matrices from Equation (5.8) requires several iterations until the solution reaches convergence. During each iteration, a new stiffness matrix is developed based on the deformed shape of the cable elements. The best iteration process is performed using the Newton method or the Newton-Raphson method. In the Newton-Raphson method, the load applied on the cable element is divided into a

number of increments. The following steps reflect the Newton methodology, with the applied load being utilized just once.

1. Suppose that a cable is divided into n number of cable elements, with each cable element having two nodes with two degrees of freedom at each node.

2. Substitute the global stiffness matrix from Equation (5.8) for each element. Note that the deformed cable length L is equal to the initial cable length L_0 in the initial analysis, and that F is equal to the pretension force due to the initial cable tightening F_i.

3. After the global stiffness matrix for each element has been assessed, assemble all matrices based on all degrees of freedom in order to evaluate the assembled global stiffness matrix in the order of (2n + 2).

4. Apply the boundary condition to the assembled global stiffness matrix K. Then calculate the global load vector after the application of the boundary conditions P. Evaluate the load vector only on the end cable nodes in two directions.

5. Use the following relation to evaluate the displacement of each node:

$$d = K^{-1} \times P \tag{5.9}$$

6. During the next iteration, evaluate a new assembled global stiffness matrix K_n based on the new cable coordinates and new tension forces in each cable element.

7. Calculate the new cable coordinates as a summation of the initial cable coordinate and the nodal displacements from the previous analysis.

8. Calculate the new tension forces F in each cable element, as follows:

   8.1 For each cable element, calculate the new cable length according to the new cable coordinates.

   8.2 Calculate the elongation ΔL of each element by subtracting the new cable length from the initial cable length.

   8.3 To evaluate the new tension force F at each cable, substitute in Hooke's law, as follows:

$$F = F_i + EA \frac{\Delta L}{L_0} \tag{5.10}$$

9. At each node, evaluate the out-of-equilibrium forces in two directions as a vector of ΔP so that it includes the tension on the cable elements and the applied loads.

10. Evaluate the incremental displacement Δd from the new assembled global stiffness matrix Kn and the out-of-equilibrium forces vector ΔP, as follows:

$$\Delta d = K_n^{-1} \times \Delta P \tag{5.11}$$

11. Calculate the new displacement vector as a summation of the previous nodal displacements plus the incremental displacement Δd.

12. Repeat the analysis in steps 6 to 11 until the cable displacements reach convergence, and then evaluate the tension in each cable according to step 8.

A numerical example was developed in order to provide additional understanding of the use of the cable element described in this chapter. This example is provided in Appendix A.

5.3.4 Analysis of a B Segment of a Bearing Cable between the Trusses

Figure 5.8(b) shows a B segment of a bearing cable between the trusses. This segment provides the roof sheathing with extra strength against uplift wind pressure. The alignment of this segment follows the gable roof slope because this cable is attached to the roof. The tension forces exerted on this segment from the pretension force in the external cables are acting to push the sheathing downward. For this reason, a gap element with a high degree of compression stiffness and zero tension stiffness is assigned at the top of the B segment. The gap element is modelled as a linear spring with a high degree of negative stiffness, and it is applied only when the B segment exhibits downward deflection. Downward deflection occurs in the presence of a small amount of uplift wind pressure. The boundary condition of this segment is chosen so that it is simply supported at both ends. To increase the accuracy of the model, this cable segment is divided into a number of cable elements, with each element carrying a different uplift wind pressure according to the distribution of the wind pressure. The nonlinear stiffness matrix defined

in section 5.3.3 is used for analyzing the B segment with a given pretension force and a uniformly distributed uplift wind load at each cable element.

5.3.5 Analysis of A Segment of a Truss with Bearing Cable

The main components in resisting uplift wind load are the trusses, which are connected to the top plate members by their critical connections (i.e., RTWCs). The bearing cables that are attached on the top of each truss provide additional support for the roof and also create an alternative load path during high-intensity wind loads. To establish a finite element model, A segments should be divided into a number of elements. Two types of finite elements are used in an A segment: frame elements and cable elements. For the truss members, a frame element is analyzed linearly, in such a way that each element has two nodes with three degrees of freedom at each node. The three degrees of freedom at the frame elements represent the moment, shear, and axial loads. The second element is the cable element, which is modelled nonlinearly, as discussed in section 5.3.3. To provide the optimal connection between the frame elements and the cable elements, node constraints should be allocated at each intersection of the cable element and the frame element at the top truss chords. These constraints between the top truss chords and the bearing cables are represented through the assignment of similar degrees of freedom in the z-direction at each node between the cable and frame elements. The z-direction degree of freedom is chosen to be in the direction of the RTWC withdrawal. Based on the RTWC load-deflection curve experiments, the RTWCs are modelled as linear springs in the direction of withdrawal. The distributed uplift wind load is applied on the top truss chords. For this reason and to enhance accuracy, each top truss chord is divided into a number of elements. For the example used in the WindEEE experiment and depicted in Figure 5.8(a), each top truss chord member is divided into four elements. For the remaining frame members, such as the bottom truss chords and the truss webs, only one frame element is used for each member since no load is applied on those members. The stiffness matrix for the frame element is written as Equation (5.12) with the local direction defined as indicated in Figure 5.12 (Hibbeler, 2012):
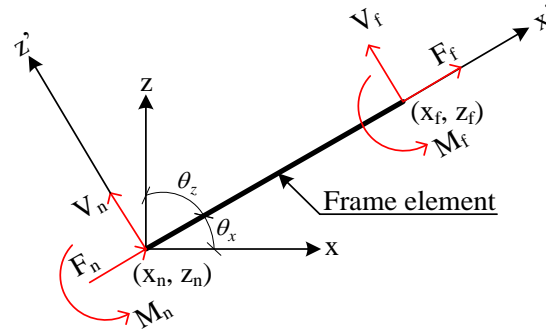
Figure 5.12: Frame element with three degrees of freedom at n and f nodes.

$$
k = \begin{matrix}
 & \overset{F_n}{} & \overset{V_n}{} & \overset{M_n}{} & \overset{F_f}{} & \overset{V_f}{} & \overset{M_f}{} & \\
 \begin{bmatrix}
 AE/L & 0 & 0 & -AE/L & 0 & 0 \\
 0 & 12EI/L^3 & 6EI/L^2 & 0 & -12EI/L^3 & 6EI/L^2 \\
 0 & 6EI/L^2 & 4EI/L & 0 & -6EI/L^2 & 2EI/L \\
 -AE/L & 0 & 0 & AE/L & 0 & 0 \\
 0 & -12EI/L^3 & -6EI/L^2 & 0 & 12EI/L^3 & -6EI/L^2 \\
 0 & 6EI/L^2 & 2EI/L & 0 & -6EI/L^2 & 4EI/L
 \end{bmatrix}
 & \begin{matrix} F_n \\ V_n \\ M_n \\ F_f \\ V_f \\ M_f \end{matrix}
\end{matrix}
\qquad (5.12)
$$

The analysis of an A segment follows a procedure similar to that for the analysis of a B segment. However, in the case of the A segment analysis, the out-of-equilibrium forces vector ΔP includes the tension on the cable elements as well as the internal forces acting on the frame elements. The out-of-equilibrium forces vector ΔP includes the equilibrium in three directions at each node (i.e., normal, shear, and moment). During the initial stage, a global stiffness matrix is evaluated for each element, whether it is a cable or a frame element. The global stiffness matrix for the cable element is defined in Equation (5.8). The global stiffness matrix for the frame element is written as in Equation (5.13):

$$
k_{global} = T^T k_{loacl} T \qquad (5.13)
$$

where k_{local} is the local frame stiffness matrix, as defined in Equation (5.12). The transformation matrix T shown in Equation (5.13) for the frame element is defined in Equation (5.14):

$$
T = \begin{bmatrix}
\lambda_x & \lambda_z & 0 & 0 & 0 & 0 \\
-\lambda_z & \lambda_x & 0 & 0 & 0 & 0 \\
0 & 0 & 1 & 0 & 0 & 0 \\
0 & 0 & 0 & \lambda_x & \lambda_z & 0 \\
0 & 0 & 0 & -\lambda_z & \lambda_x & 0 \\
0 & 0 & 0 & 0 & 0 & 1
\end{bmatrix}
\tag{5.14}
$$

After the global stiffness matrix has been defined for each element, the assembly global stiffness matrix K is evaluated for all A segment. It is also important to include the RTWC linear springs in the assembly global stiffness matrix. Following the application of the boundary condition, the load vector is written as in Equation (5.15). This load vector is used with the assembly global stiffness matrix K in order to calculate the initial displacement:

$$
d = K^{-1} \times P
\tag{5.15}
$$

In the first iteration, up to the point where the analysis reaches convergence, the tension on each cable element is evaluated, and the internal forces in each frame element are also calculated. Equation (5.16) illustrates how to calculate the tension forces in each cable element given the new coordinates of the A segment. F_i and L_0 are the initial cable tension and the initial cable length, respectively. L is the new cable length. Where j= 1,2,...., number of cable elements:

$$
F_j = F_i + EA \frac{L_j - L_{0j}}{L_{0j}}
\tag{5.16}
$$

The frame element has two nodes with three degrees of freedom at each node, which translates into six forces to be evaluated for each element. The six forces represent two axial forces, two shear forces, and two moments. The following steps are used for evaluating the truss member forces, where i = 1, 2,..., number of frame elements:

$$
u_i = T_i \times v_i
\tag{5.17}
$$

$$Q_i = k_i \times u_i - Load_i \tag{5.18}$$

$$Fm_i = T_i^T \times Q_i \tag{5.19}$$

v_i: the nodal displacement for each frame element in the global direction;

T_i: the transformation matrix for the frame elements, as shown in Equation (5.14);

u_i: the nodal displacement for each frame element in the local direction;

$Load_i$: the load applied to each frame element in local directions;

k_i: the local stiffness matrix for each frame element, as shown in Equation (5.12);

Q_i: the internal forces of the frame member in the local direction;

Fm_i: the frame member forces in the global direction.

The out-of-equilibrium forces vector ΔP includes the tension on the cable elements Fj and the internal forces acting on the frame elements Fmi as well as the RTWC reaction, which is calculated by multiplying the deflection by the spring constant. As shown in Equation (5.11), the out-of-equilibrium forces vector ΔP is used with the revised stiffness matrix Kn in order to evaluate the incremental displacement Δd. A numerical example was designed to provide additional understanding of the A segment analysis. This example is provided in Appendix B.

5.4   Validation of the Numerical Solution

The solution model discussed in section 5.3 was validated against the experimental testing conducted at both the structural laboratory and the WindEEE facility. In both experiments, a gable roof house was built in order to examine the behaviour of toe-nailed connections under uplift wind loads and to assess the external retrofit system. In the structural laboratory experiment conducted by Jacklin (2013), the uplift load was

simulated using two hydraulic jacks, which were placed beneath the experimental model so that they created six concentrated uplift loads. In the WindEEE testing conducted by Rosenkrantz (2017), a wind flow was applied by the WindEEE fans in order to simulate the real behaviour of the system. In both experiments, the experimental model was tested with and without the application of the external retrofit system.

5.4.1 Structural Laboratory Testing

Jacklin (2013) conducted a structural laboratory test in three separate stages: a house without the proposed retrofitting, a house with the retrofit system, and the retrofitted house that had been damaged during the first stage. The second stage is the one used for the validation presented in this current chapter. Figure 5.13 depicts the layout of the structural laboratory experiment, which comprised three supporting trusses with six RTWCs, as shown in the figure. A total of six bearing cables were attached to the house on top of each truss and on the top of the sheathings between the trusses. The six bearing cables were anchored to two rigid bars, one on each side of the house. Each rigid bar was anchored by two external cables.
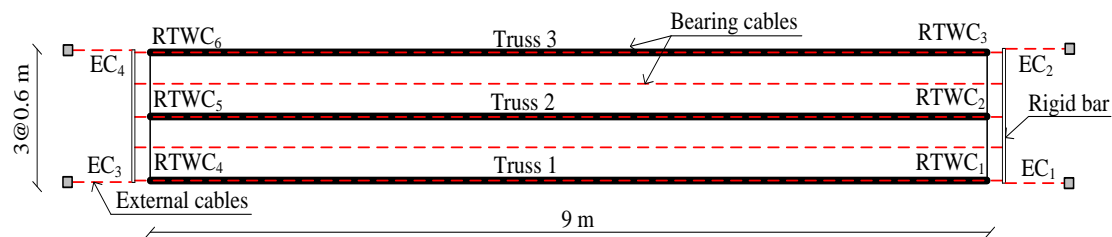
Figure 5.13: Layout of the structural laboratory experiment conducted by Jacklin (2013).

For the solution model to perform a numerical analysis, it is important to define the nonlinear RTWC stiffness. Jacklin (2013) defined RTWC stiffness based on the first stage experiment, in which the house was subjected to uplift jack forces without the application of the retrofitting system. The nonlinear stiffness curve shown in Figure 5.14 is composed of the RTWC load calculated as the total uplift load divided by six, which

was plotted against the RTWC deflection calculated as an average of the deflection values for all six connections.
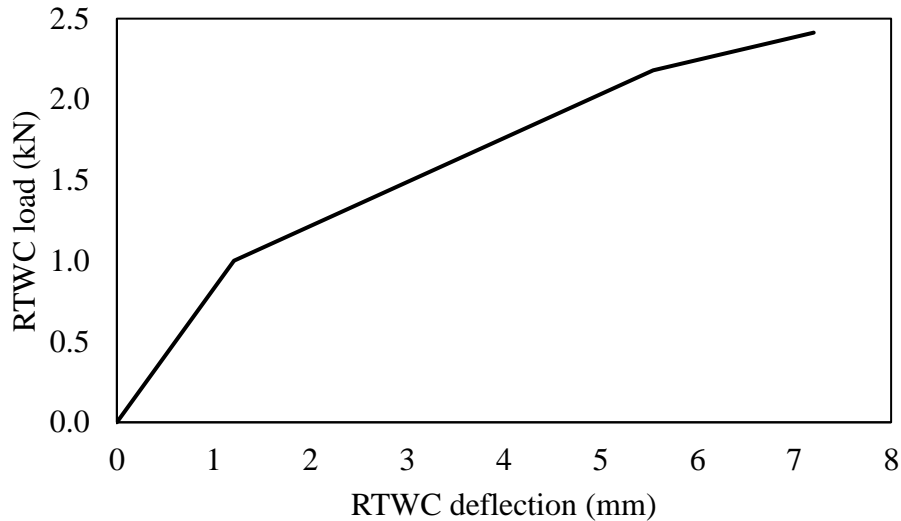
Figure 5.14: Trilinear RTWC load-deflection curve used in the solution model Jacklin (2013).

As mentioned earlier, the experimentally applied uplift load was concentrated on six points, while the solution model input requires the uplift load to be distributed across the sheathings. The concentrated uplift load is therefore simulated as a uniformly distributed uplift pressure on the sheathing in such a way that the resultant load would be fairly similar based on either interpretation. Figure 5.15 provides a comparison between the proposed uniformly distributed uplift pressure for analyzing the solution model, on one hand, and the experimental concentrated loads obtained from the load cells under the hydraulic jacks, on the other. The comparison is formatted as 190 load steps with the results of both load patterns expressed in kN force units. The proposed uniformly distributed uplift pressure is applied incrementally in the solution model, and the self weight of the experimental setup is distributed equally to each RTWC in order to provide a reaction during the first iteration.
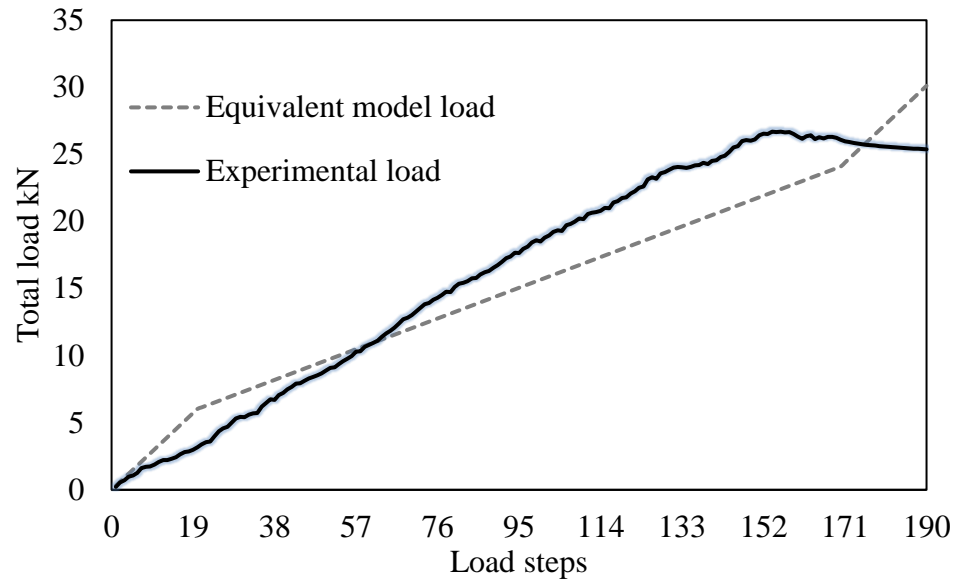
Figure 5.15: Comparison of the proposed uniformly distributed uplift pressure and the experimental concentrated loads.

Figure 5.16 presents the two types of segments used in the solution model. In total there are three A segments and three B segments. In the A segments, the top truss chords are divided into 20 finite frame elements, each 0.47 m long. These 20 frame elements are connected to a bearing cable using the same degrees of freedom as in the vertical direction. The other truss members are modelled with one frame element since no loads are applied on these elements. The cross sections of the top and bottom chords are 2 in. by 4 in., and all of the webs are 2 in. by 3 in. The B segments are divided into 20 cable elements, each 0.47 m long. The uplift pressure is distributed over the segments as load per unit length. The loads on the roof sheathings are therefore divided into 80 areas.
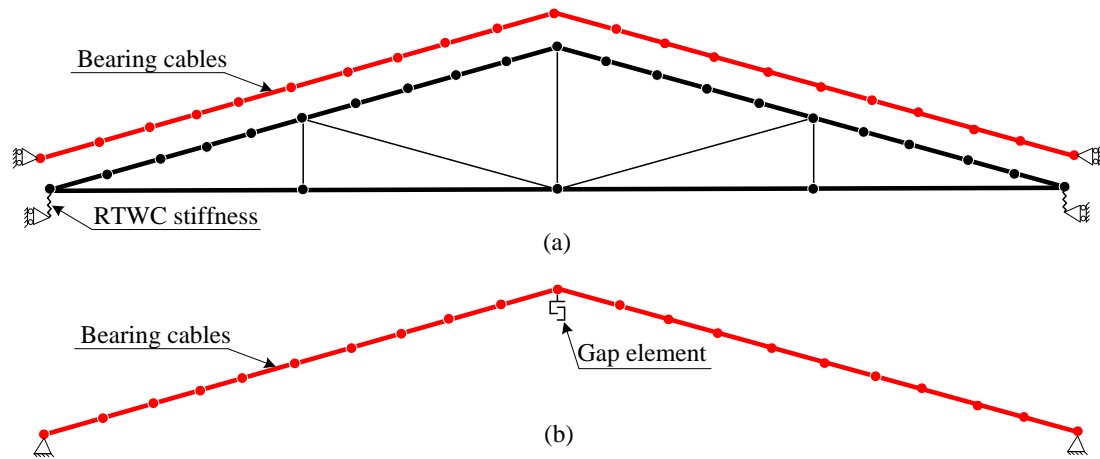
Figure 5.16: A and B segments: (a) truss with bearing cable (A segments); (b) bearing cable only (B segments).

Figure 5.17 is a graph of the RTWC deflection predictions plotted against the experimental results. The connection deflections indicated on the horizontal axes are compared with the total uplift loads specified on the vertical axes. Due to the use of uniform pressure and similar degrees of RTWC stiffness in the solution model, the predicted deflection was evaluated based on a similar value for all connections. Not all experimental results are represented in Figure 5.17 since two connections failed quickly, exhibiting excessive deflection. This situation is attributable to the variation in the RTWCs, as discussed by Reed et al., (1997) and Khan (2012). In general, the predicted RTWC deflections represent a good match with the experimental results in terms of values and trends.

Figure 5.18 shows the tension predicted in the external cables against that revealed by the experimental results. A comparison was carried out with respect to the total applied load. In the numerical model prediction, when the total uplift load ranges from zero to 20 kN, the tension in the external cables remains at the pretension force of 1.0 kN. Above 20 kN, the tension in the cables increases rapidly with increases in the total uplift load. The output produced by the solution model leads to the conclusion that, during the initial stage, the RTWCs absorb most of the tension forces. After a specific point when the connections become weaker, the tension in the external cables increases quickly. However, an obvious difference exists between the predicted and the measured values.

This discrepancy relates to the effects of the concentrated load during the experiment testing versus the equivalent pressure used in the solution model analysis.
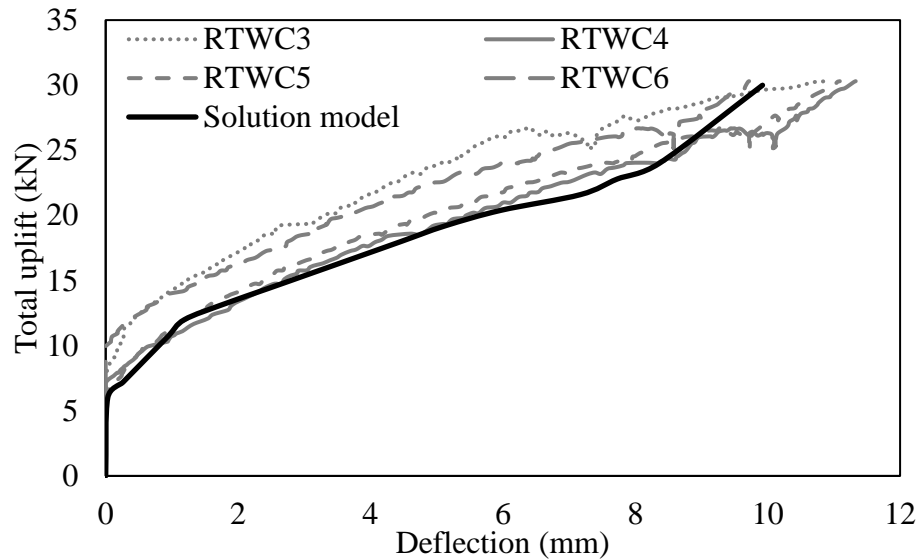
Figure 5.17: Predicted deflection plotted against the experimental RTWC deflection.
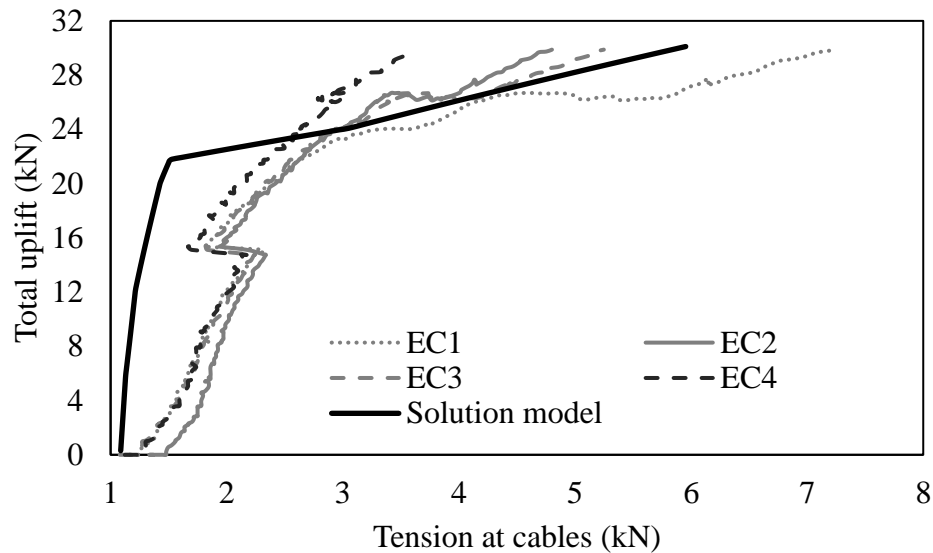
Figure 5.18: Predicted external cable tension plotted against the experimental cable tension.

In summary, the analysis of the structural laboratory experiment using the solution model shows good agreement with the experimental responses, especially for the RTWC

deflections. On the other hand, the predicted external cable tension does not adhere to the experimental values due to the approximation of the analysis. The critical links for carrying the uplift wind loads are RTWCs, for which this solution model offers reasonable predictions. Cables, such as aircraft cables, could carry heavy axial loads even after the RTWCs fail so that the tension in the cables does not necessarily signal the failure of the house.

5.4.2 WindEEE Experiment

As shown in Figure 5.19, the WindEEE experiment performed by Rosenkrantz (2017), was conducted in three stages: a load control test, a displacement control test, and a retrofitted control test. In the first stage, the pressure coefficient of the prototype was evaluated at each fan speed. These pressure coefficients are evaluated at 40 points over the roof Rosenkrantz (2017). To perform the numerical analysis, the pressure on the roof sheathing is divided into 288 pressure areas. Two-dimensional cubic interpolation is employed for determining the pressure coefficient at the centre of each pressure area. Figure 5.20 displays the pressure coefficients at 288 points on the roof. The toe-nails used in this experiment were 3-2D common nails. The constitutive relation for this type of toe-nail was established experimentally by Rosenkrantz (2017) according to ASTM D1761, as indicated in Figure 5.21.

To assess the performance of the experimental prototype with and without the retrofitting system, both the pressure coefficients and the constitutive relation are incorporated into the solution model. The evaluation of the solution model without the retrofitted system involved the analysis of four typical trusses, including an assessment of the nonlinear stiffness of the toe-nailed connections. The solution model that included the retrofitting system is divided into two types of segments: A segments and B segments, as illustrated in Figure 5.8.
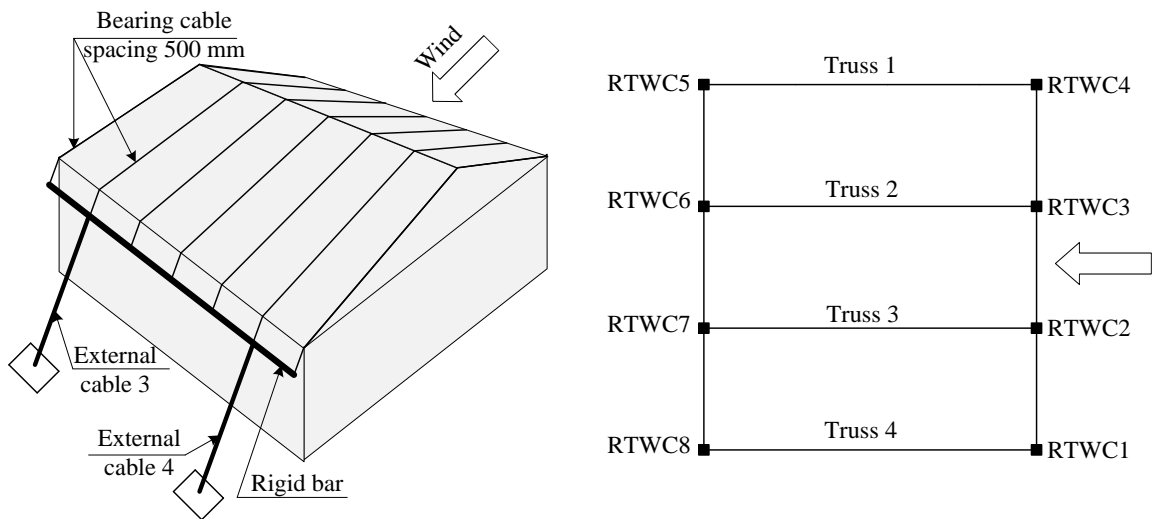
Figure 5.19: Layout of the WindEEE experiment conducted by Rosenkrantz (2017).
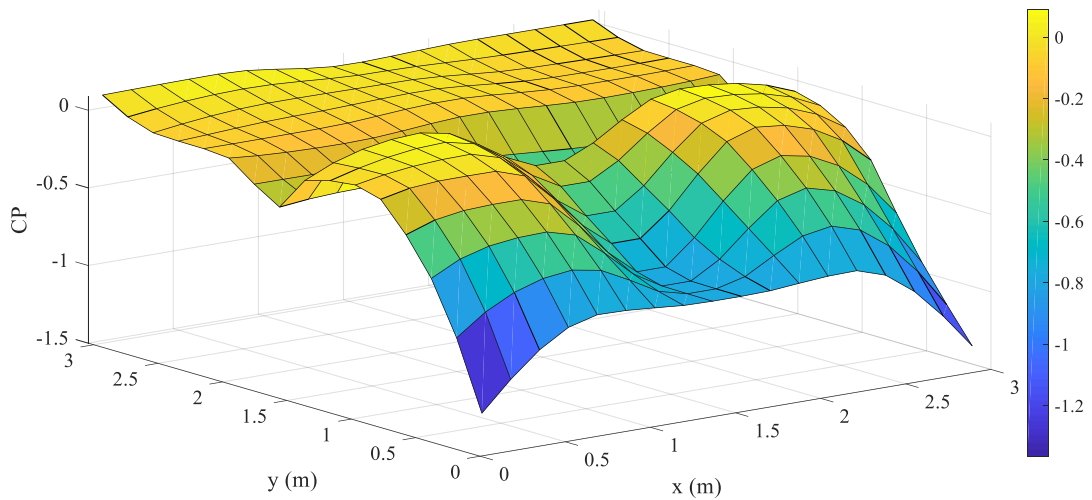
Figure 5.20: Pressure coefficients at 288 roof positions.
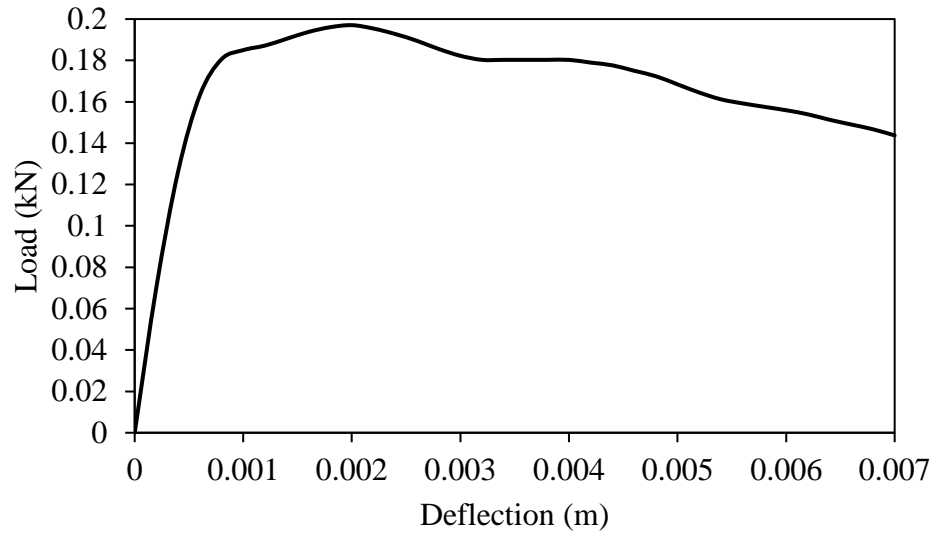
Figure 5.21: Constitutive relation of the 3-2D toe-nails (Rosenkrantz, 2017).

Prior to an examination of the solution model output versus the experimental measurements, the solution model output was compared with the results from another analysis tool: three-dimensional FEM implemented using SAP2000 commercial software. This comparison between the solution model output and the SAP2000 results was performed for the WindEEE experiments with and without the application of the retrofitting system. Figures 5.22 and 5.23 present the comparison for wind speeds ranging from 1 m/sec up to 33 m/sec. For the WindEEE experiments without the retrofitting, the FEM/SAP2000 analysis did not reach convergence until after a wind speed of 33 m/sec. Figures 5.22 through 5.23 present a comparison of the results produced by both analysis methods for the WindEEE experiment without the retrofit system. As can be seen in these figures, good agreement is evident between the three-dimensional FEM results and those produced by the approximated solution model in terms of values and curve trends.
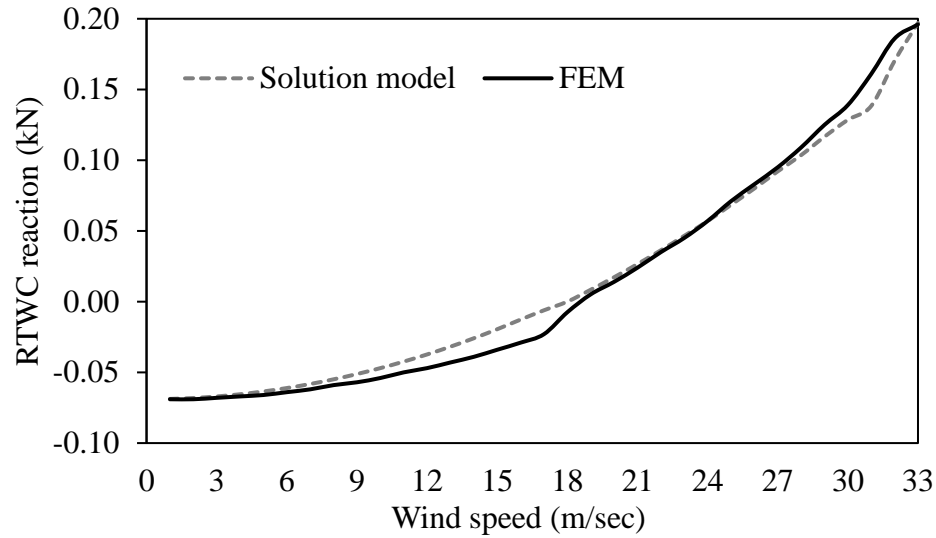
Figure 5.22: Reaction of windward RTWC1 as determined by FEM and by the solution model for the WindEEE experiment without the retrofit.

Figure 5.24 indicates that the results of both analysis methods follow the given nonlinear RTWC curve. Figures 5.25 to 5.27 provide a comparison of the results of the WindEEE experiment conducted with support from the retrofitted system. As illustrated in these figures, the solution model assumptions are a good match for the FEM results. However, in terms of evaluating the tension in the external cable, compared to the FEM results, the solution model underestimates the cable tension by a mean difference of 4.7 %.
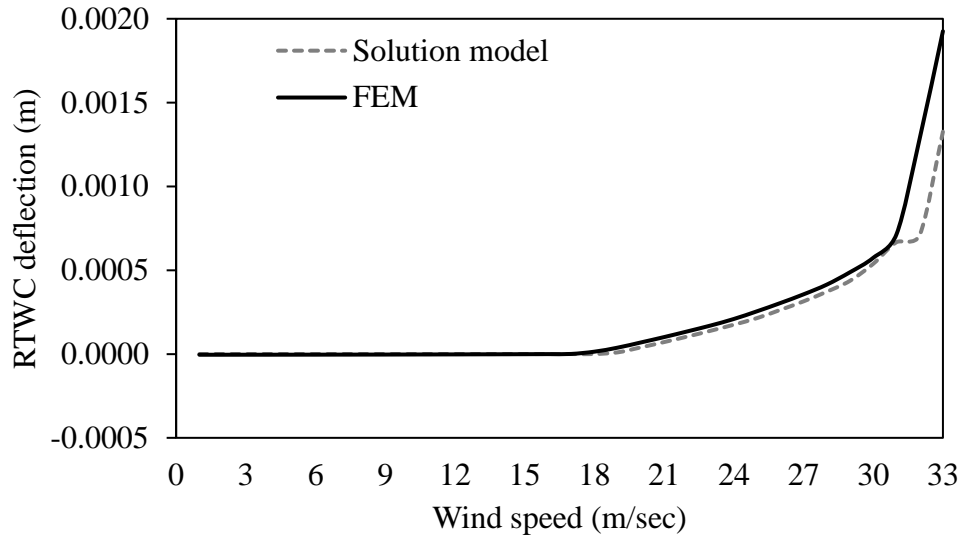
Figure 5.23: Deflection of windward RTWC2 as determined by FEM and by the solution model for the WindEEE experiment without the retrofit.
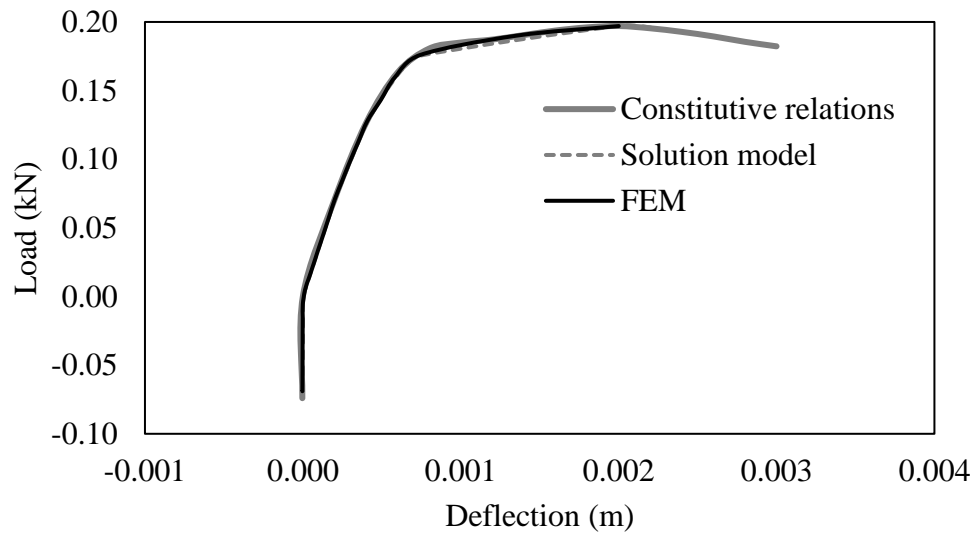
Figure 5.24: Load-deflection curve of leeward RTWC4 as determined by FEM and by the solution model in comparison with the constitutive relation of three-2D toe-nails for the WindEEE experiment without the retrofit.
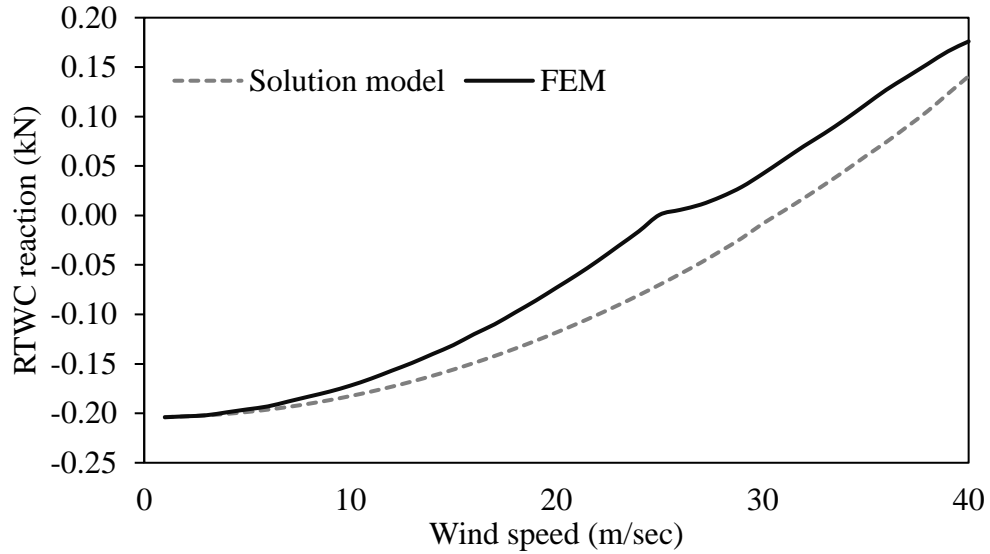
Figure 5.25: Reaction of windward RTWC2 as determined by FEM and by the solution model for the WindEEE experiment with the retrofit.
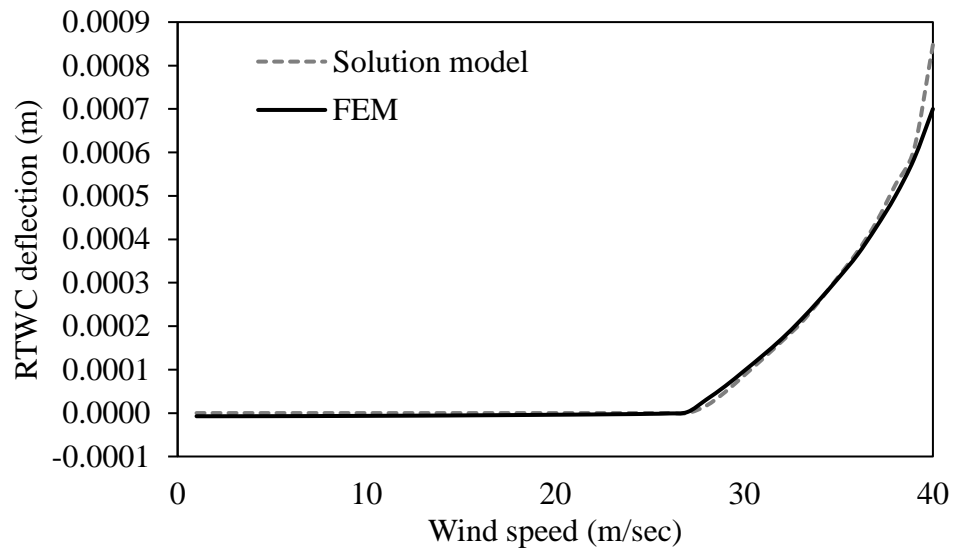
Figure 5.26: Deflection of leeward RTWC4 as determined by FEM and by the solution model for the WindEEE experiment with the retrofit.
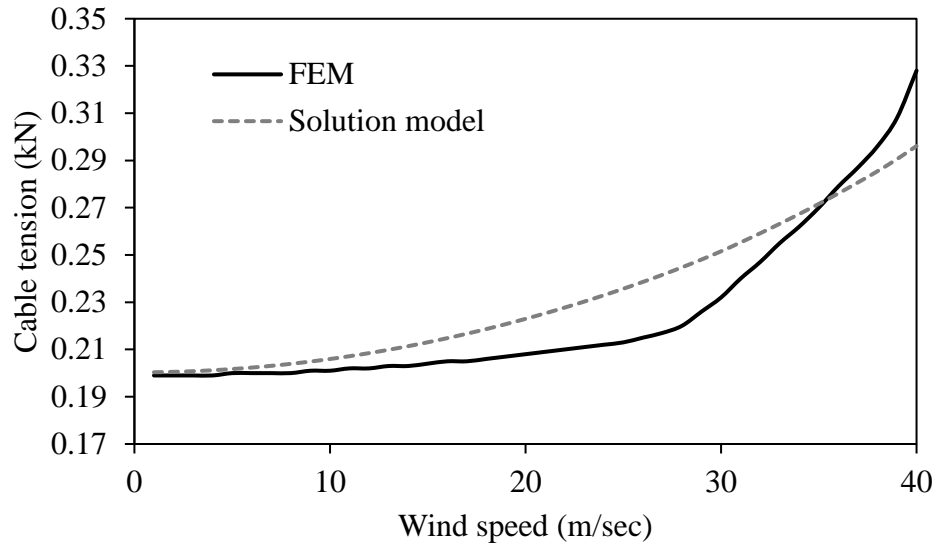
Figure 5.27: Tension in windward cable 3 as determined by FEM and by the solution model for the WindEEE experiment with the retrofit.

The first step in validating the solution model against the results of WindEEE experiment is targeted at the second stage of the experiment: the displacement control test. In this test, the displacement of the RTWCs is measured against three fan speeds: 50 %, 60 %, and 75 %. The validation process involved analyzing the solution model with respect to the pressure coefficients for each fan speed. The analysis thus began with the application of the self weight of the roof plus the pressure produced by a fan speed of 50 %, which is divided into 50 increments. Once all of the 50 % fan speed increments have been applied, pressure at a 60 % fan speed is then applied with the same number of increments and with the initial deformation set at the value produced at the previous fan speed. The final step is the application of the 75 % fan speed in 50 increments following the completion of the assessment of the displacement produced by the pressure from the 60 % fan speed. Figure 5.28 shows a comparison of the solution model prediction with the experimental results of the displacement control test for RTWC1, at the windward edge, and RTWC3, located at the middle of the windward side. As shown in Figure 5.28, both the experimental and numerical results indicate that the RTWCs start to open at an approximate wind speed of 17 m/sec. After the opening has occurred, the experimental

results show a quicker failure than does the numerical prediction. RTWC1 fails at a wind speed of 25 m/sec experimentally and at 28 m/sec according to the solution model, while RTWC3 shows failure at a lower wind speed due to increases in the tributary area. The difference in results is attributable to the exclusion of the effects of internal pressure in the solution model analysis.
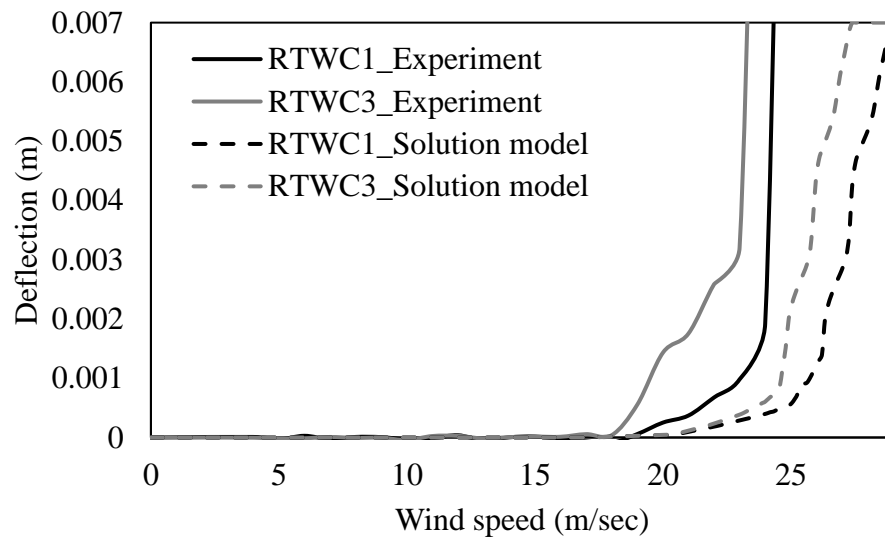
Figure 5.28: Windward RTWC1 and RTWC3 deflection results produced experimentally and by solution model for the displacement control test.

The final step in the validation of the solution model predictions against the WindEEE experimental findings was directed at the third stage of the experiment: the retrofitted control test. In this test, the displacement of the RTWCs and the external cable tension are both measured for fan speeds of 50 %, 60 %, 75 %, and 90 %. The solution model analysis proceeded according to the steps defined in section 5.3.2. The uplift wind pressure obtained from each fan speed is applied incrementally, with 50 increments for each fan speed, until the middle windward connections exhibit failure. Figure 5.29 provides the experimental and solution model deflection results for the middle windward connections.
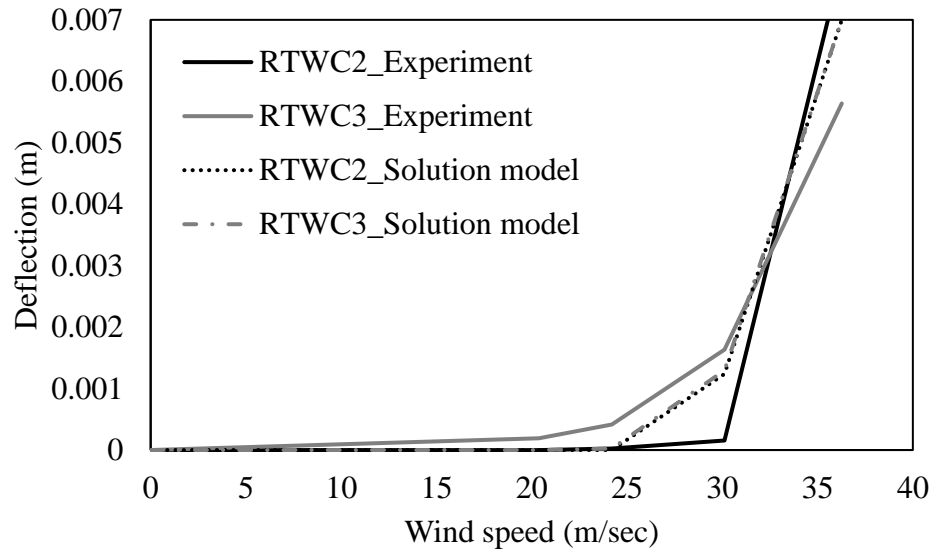
Figure 5.29: Comparison of the experimental and solution model deflection results for the middle windward connections.

As shown in Figure 5.29, and according to the solution model prediction, the middle windward connections exhibit identical deflection, which lies between the experimental results. The identical solution model results are due to the assignment of a similar load-deflection curve for the RTWCs. The experimental windward middle connection demonstrates a different degree of deflection due to the varied stiffness of the toe-nailed connections, especially ones with the small 2D nails. To summarize, the predicted RTWC deflection values match well with the experimental results, an agreement that is superior to that obtained for the displacement control test due to the internal pressure factor. To evaluate the tension forces required at the external cables, the pressure coefficients shown in Figure 5.20 are utilized for assessing the solution model analysis with respect to a range of wind speeds from 1 m/sec to 40 m/sec. Figure 5.30 enables a comparison of the external Cable4 tension measured experimentally against the predictions provided by FEM and the solution model. All of the other cables exhibited behaviour similar to that of Cable4. To conclude, the predicted cable tension is an underestimate of the experimental

results. It seems that the external cables gain tension force after the connections separate from the walls. However, Figure 5.30 also reveals a good match between the solution model and the FEM results, with a mean difference extending only up to 5 %.
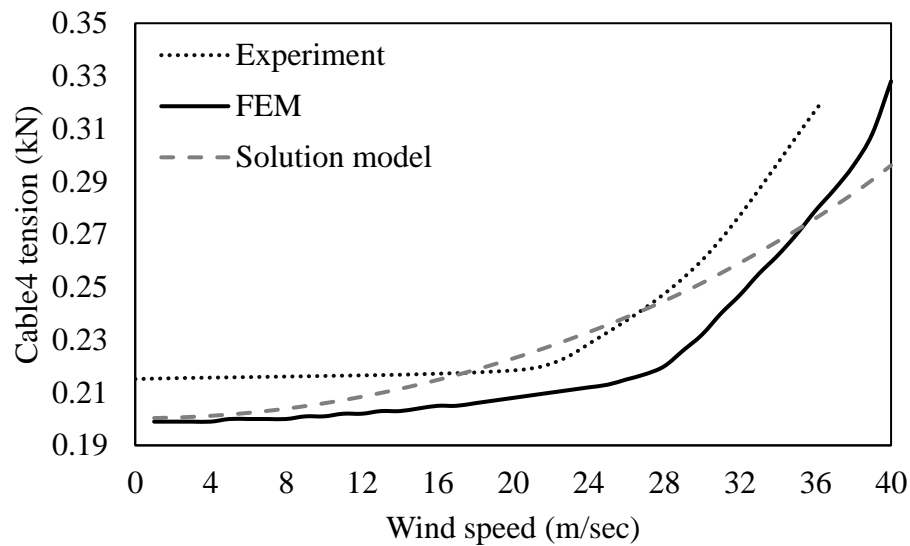
Figure 5.30: Experimental, solution model, and FEM Cable4 tension results.

5.5 Application of the Solution Model

The next important step following the validation of the results produced by the solution model against the experimental findings is to ascertain how well the retrofitted system can resist extreme wind events. This factor can be established numerically through the application of the solution model assumptions to small-scale models. The output of this application proves how the retrofitting system could enhance the capacity of RTWCs to resist uplift wind loads. One method of evaluating the performance of the retrofitting system with respect to absorbing a portion of the uplift wind loads is to calculate the load sharing between the retrofitting system and the RTWCs. As previously mentioned, RTWC load sharing is defined as the ratio between the total RTWC reaction and the uplift loads. In a similar way, the retrofit load sharing was determined as the ratio

between the total retrofit reactions and the applied uplift force. To assess the distribution of the uplift wind load with respect to the supporting systems, the load sharing calculations are performed without the inclusion of the self weight of the roof.

Figures 5.31 and 5.32 illustrate the load sharing calculations with the use of the solution model for the WindEEE and structural laboratory prototypes, respectively. In Figure 5.31, the uplift wind load is calculated from the pressure coefficient shown in Figure 5.20, with incremental wind speeds ranging from 5 m/sec to 60 m/sec, which is greater than the wind speed applied to the experimental model. It is clear from Figure 5.31 that the WindEEE prototype distributed the uplift wind loads according to a load sharing of 80 % and 20 % for the RTWCs and the retrofitting system, respectively. After the failure of the RTWCs at a wind speed of 40 m/sec, the load sharing percentage for the retrofit system increases rapidly with a decreasing RTWC load share. The increase in the retrofitting load share confirms that the retrofitting system can create an alternative load path following RTWC failure. Figure 5.32 illustrates the percentage of the load sharing for the structural laboratory experiment with respect to the total uplift loads. The total uplift load indicated in Figure 5.32 was simulated as a uniform pressure in order to apply it in the solution model, but it was applied experimentally as a concentrated load. In the structural laboratory experimental stage, the prototype was tested up to a total uplift force of 36 kN (Jacklin 2013). Figure 5.32 includes the findings with the total uplift force extended up to 50 kN in order to demonstrate the load sharing beyond the experimental results. A comparison of Figures 5.31 and 5.32 reveals that both figures convey the same conclusion; however, in Figure 5.32 the load shared during the initial stage is 90 % for the RTWCs and 10 % for the retrofitting system. According to Figure 5.32, the connections start to detach from the walls at a total uplift force of 22 kN, following which, the connections lose stiffness quickly.
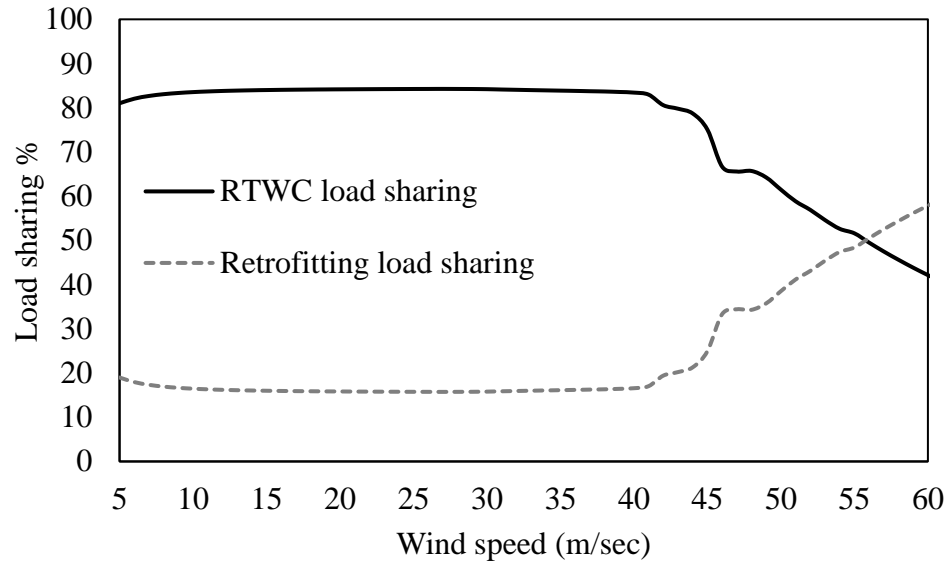
Figure 5.31: RTWC and retrofitting load sharing for the WindEEE experiment.
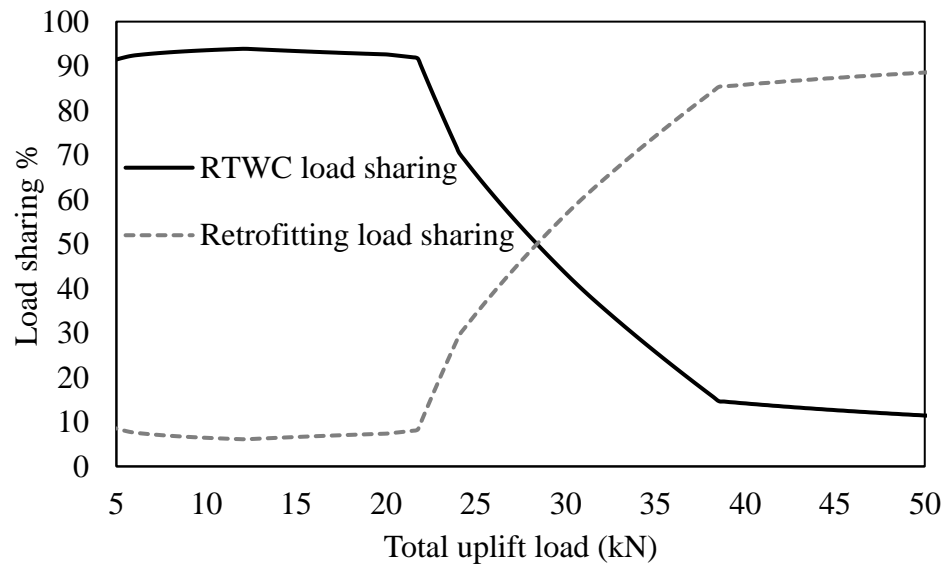
Figure 5.32: RTWC and retrofitting load sharing for the structural laboratory experiment.

On the other hand, it could be useful to evaluate the performance of the retrofitting system with respect to reducing the effects of uplift wind loads on the roofs of houses based on an analysis of the solution model with and without the retrofit system in order to

distinguish the difference between these scenarios. Figure 5.33 shows the reaction of RTWC1 in regard to the WindEEE model with respect to the wind speed. The analysis was performed in two stages: with and without the retrofit system. At the initial loading stage, and due to the pretension forces, the RTWCs under the application of the retrofit system exhibited a much more negative load reaction than that of the connections without the application of the retrofit system. In this situation, the failure of the connections is delayed. According to Figure 5.33, the retrofitting system elevates the possible failure wind speed by 36.4 %; however, after the connections have failed, the retrofitting system also creates an additional load path and helps to keep the roof attached to the house after the wind storm ends, as shown in Figures 5.31 and 5.32.
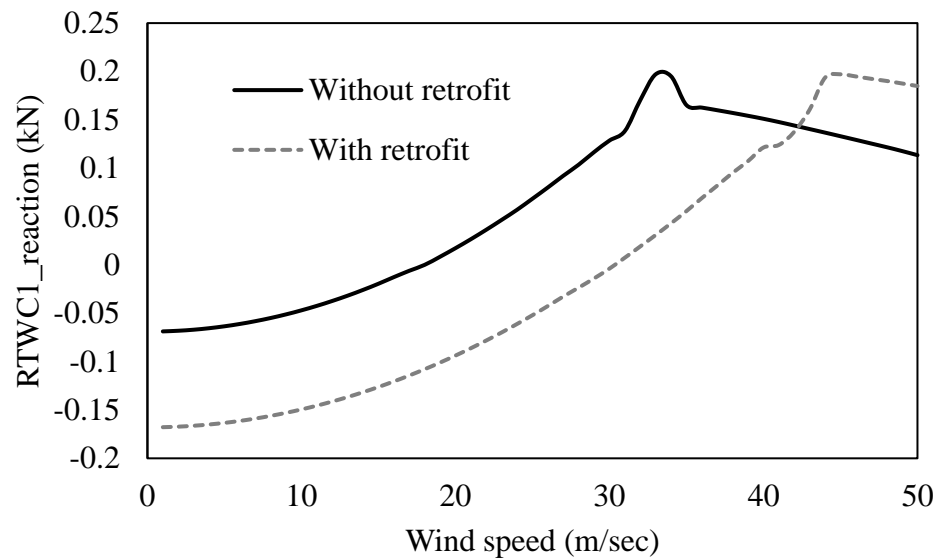
Figure 5.33: RTWC1 reactions for the WindEEE model with and without the retrofitting system.

5.6 Conclusion

This chapter has presented a simplified approach for analyzing externally retrofitted light-frame wood houses. Dring a heavy wind storm, this external retrofitting can serve

the functions of delaying the failure of critical roof connections and creating an alternative load path. The retrofitting system used in the analysis of this chapter consists of three main elements: bearing cables, external cables, and rigid bars. The bearing cables are installed on the top of the roof in such a way that they are distributed over each truss and between the trusses. They are then connected to external cables by means of rigid bars that run along the edges of the roof. The function of the rigid bars is to reduce the number of external cables required and to distribute the pretension forces equally at each bearing cable. The external cables are pretensioned using turnbuckles and are connected to the ground by micropiles that are permanently embedded at the sides of the house.

The retrofitting system was tested experimentally at the structural laboratory and WindEEE Research Institute by Jacklin (2013) and Rosenkrantz (2017) respectively, both located at University of Western Ontario. In the structural laboratory, a segment of a full-scale gable house roof was tested under static load. This segment or prototype consisted of three simply supported Howe trusses. Each truss had one RTWC at the east and west sides. The prototype was tested with and without the application of the retrofitting system. The WindEEE experiment involved the destructive testing of a small-scale light-frame wood house, which was tested under a real wind flow generated from the WindEEE dome. The experiment was conducted in three separate stages: a load control test, a displacement control test, and a retrofitted control test. For each stage, the same small-scale prototype consisted of four trusses 3.0 m long, spaced 1.0 m apart.

The solution model and the finite element model results were first compared with respect to their analysis of the retrofitting prototype used in the WindEEE experiment. A good match can be observed, especially for RTWC deflection; however, in terms of evaluating the external cable tension, the solution model underestimates the tension determined using FEM. The mean difference in the cable tension results produced by the two analysis methods is 4.7 % with respect to the finite element modelling.

The simplified approach presented in this chapter was then validated against both the structural laboratory experiment and the WindEEE experiment. This simplified approach was directed at determining the load sharing between the trusses and the retrofitted

system based on the behaviour of a beam on an elastic foundation under flexural and shear deformation. This load sharing was used in conjunction with FEM for analyzing the retrofitted roof system. FEM requires the inclusion of an analysis of the cable elements connected to the frame elements. The analysis of the structural laboratory experiment using the simplified approach showed good agreement with the experimental responses, especially with respect to RTWC deflection. However, the predicted external cable tension results failed to mirror the experimentally established values due to the approximation of the analysis. The bare and the retrofitted model was validated against the WindEEE experiment. The RTWC deflection predicted by the retrofitted model was in good agreement with the experimental results and was superior to the results for the bare model due to the exclusion of consideration of the internal pressure. The cable tension predicted for the WindEEE experiment was an underestimate of the experimental results because, with the simplified approach, the external cables gain tension force after the connections separate from the walls. To summarize, the use of the retrofitting system increases by 36.4 % the possible wind speed that the RTWCs can withstand prior to failure. The retrofitting system also performs the function of keeping the roof attached to the house. It was found that the WindEEE prototype distributes the uplift wind loads according to a load sharing of 80 % and 20 % for the RTWCs and the retrofitting system, respectively. Following RTWC failure at a wind speed of 40 m/sec, the load sharing percentage for the retrofit system increases rapidly as the RTWC load share decreases.

5.7 References

Alldredge, D. J., Gilbert, J. A., Toutanji, H. A., Lavin, T., and Balasubramanyam, M. S. (2012), "Uplift capacity of polyurea-coated light-frame rafter to top plate connections", *Journal of Materials in Civil Engineering*, **24**(9), 1201-1210.

Anderson F. S., Davis W. L., Loye W. G. (1973), "Mooring apparatus", U.S. Patent No.3,726,054.

ASCE (2005), Minimum design loads for buildings and other structures, American Society of Civil Engineers; Reston, Va.

ASTM, D. (2006). "Standard test methods for mechanical fasteners in wood".

Bimberg, U.H., and Bimberg, O.U. (1997), "Roof anchoring apparatus", U.S. Patent No.5,623,788.

Blessing, C., Chowdhury, A. G., Lin, J., and Huang, P. (2009), "Full-scale validation of vortex suppression techniques for mitigation of roof uplift", *Engineering Structures*, **31**(12), 2936-2946.

Canbek, C., Mirmiran, A., Chowdhury, A. G., and Suksawang, N. (2011), "Development of fiber-reinforced polymer roof-to-wall connection", *Journal of Composites for Construction*, **15**(4), 644-652.

Canadian Wood Council,and Canadian Standards Association. (2010), "Wood design manual", The complete reference for wood design in Canada Ottawa, *Canadian Wood Council*.

Coarita, E., and Flores, L. (2015), "Nonlinear analysis of structures cable–truss", *International Journal of Engineering and Technology*, **7**(3), 160-169.

Cook, R. D. (2002), "Concepts and applications of finite element analysis (4th ed.), Wiley, New York.

Cornett, R.M., Woehlk, A.,and Crumpler, N. (2000), "Structural tie-down apparatus", U.S. Patent No.6,161,339.

Datin, P. L., Hill, K. M., and Scheid, C. (2008), "Hurricane Resistance of Florida Residential Construction: In-Field Evaluation of Practicality, Acceptability and Effectiveness of Hurricane Retrofit Mitigation Measures", UF01-08; University of Florida.

Datin, P. L., Prevatt, D. O., and Pang, W. (2011), "Wind-uplift capacity of residential wood roof-sheathing panels retrofitted with insulating foam adhesive", *Journal of Architectural Engineering*, **17**(4), 144-154.

Dessouki, A. A. (2010), "Analysis and retrofitting of low rise houses under wind loading", Master Thesis, University of Western Ontario, London, ON, Canada.

Enajar, F.E., Jacklin, R.B., El Damatty, A.A. (2019), "Nonlinear Modeling of Roof to Wall Connections in a Gable-Roof Structure under Uplift Wind Loads", *Wind and Structures*, **28**(3),181-190.

Hibbeler, R. C. (2012), "Structural analysis (8th ed.)", Pearson/Prentice Hall, Upper Saddle River, N.J.

Jacklin, R. B. (2013), "Numerical and experimental analysis of retrofit system for light-framed wood structures under wind loading", Master Thesis, University of Western Ontario, London, ON, Canada.

Jacklin, R.B., El Damatty, A.A. and Dessouki, A.A. (2014), "Finite-element modeling of a light-framed wood roof structure", *Wind and Structures*, **19**(6), 603-621.

Kapur, O., Mahadevia, A., Park, J., Passman, S., Perotin, M., Reeder, A., Seitz, L., Sheldon, A., and Tezak, S. (2010), "Wind retrofit guide for residential buildings", Federal Emergency Management Agency, December.

Khan, M. A. A. (2012), "Load-sharing of toe-nailed, roof-to-wall connections under extreme wind loads in wood-frame houses", Master Thesis, University of Western Ontario, London, ON, Canada.

Lindstrom, M. (2008), "Emergency structure restraint", U.S. Patent No.2008/0040981.

Li, Y., and Ellingwood, B. R. (2006), "Hurricane damage to residential construction in the US: importance of uncertainty modeling in risk assessment", *Engineering Structures*, **28**(7), 1009-1018.

Leatherman, S. P., Chowdhury, A. G., and Robertson, C. J. (2007), "Wall of wind full-scale destructive testing of coastal houses and hurricane damage mitigation". *Journal of Coastal Research*, **23**(5), 1211-1217.

Morrison, M. J., Henderson, D. J. and Kopp, G. A. (2012), "The response of a wood-frame, gable roof to fluctuating wind loads", *Engineering Structures*, **41**, 498-509.

Papadopoulos, P. G., Arethas, J., Lazaridis, P., Mitsopoulou, E., and Tegos, J. (2008), "A simple method using a truss model for in-plane nonlinear static analysis of a cable-stayed bridge with a plate deck section", *Engineering Structures*, **30**(1), 42-53.

Phillips, B.R. (1995), "Tie down for building structures", U.S. Patent No.5,384,993.

Pierce, R.G. (2005), "Wind cap for building", U.S. Patent No.2005/0166468.

Pittman, C.L. (2004), "Mobile home tie-down apparatus", U.S. Patent No.6,722,085.

Prevatt, D. O., McBride, K. E., Roueche, D. B., and Masters, F. J. (2014), "Wind uplift capacity of foam-retrofitted roof sheathing panels subjected to rainwater intrusion", *Journal of Architectural Engineering*, **20**(4), B4014001- B4014009.

Prevatt, D. O. (2003), "Constructing Scale Model Roof-to-Wall Connections in Residential Construction for Dissemination of Hurricane", Report No. WLTF 02-07, Clemson University.

Reed, T. D., Rosowsky, D. V. and Schiff, S. D. (1997), "Uplift capacity of light-frame rafter to top plate connections", *Journal of Architectural Engineering*, **3**(4), 156-163.

Reinhold, T. A. (2003), "Field Tests of Orage Corporation Hurricane Harness Tie-Down System", Clemson University.

Rojas, A. L. (2012), "Method of structural analysis for statically indeterminate beams", *International Journal of Innovative Computing Information and Control*, **8**(8), 5473-5486.

Rosenkrantz, J. D., Enajar, A., Jacklin, R., and El Damatty, A. (2016), "Structural modelling and verification methods to develop a cable roof harness retrofit", RESILIENT INFRASTRUCTURE, London, ON, June.

Rosenkrantz, J. D. (2017), "Numerical and Experimental Analysis of a Retrofit System for Light-Framed Wood Structures Under Wind Loading", Master Thesis, University of Western Ontario, London, ON, Canada.

Small, W. (1904), "Roof anchoring device", U.S. Patent No. 777,441. Washington, DC: U.S. Patent and Trademark Office.

Torkamani, M. A. M., and Shieh, J. (2011), "Higher-order stiffness matrices in nonlinear finite element analysis of plane truss structures", *Engineering Structures*, **33**(12), 3516-3526.

Wilson, E. L. (2002), "Three-dimensional static and dynamic analysis of structures", Computers and Structures, Inc. Berkeley, California, USA.

Yazdani, N., Townsend, T., and Kilcollins, D. (2005), "Hurricane wind shelter retrofit room guidelines for existing houses", *Practice Periodical on Structural Design and Construction*, **10**(4), 246-252.

Chapter 6

6 Conclusions and Future Work

6.1 Summary

This thesis presents an investigation of the behaviour of light-frame wood houses with respect to the nonlinear stiffness of toe-nailed RTWCs. The body of the research is presented in four chapters. In Chapter 2, a full-scale experiment conducted at the Insurance Research Lab for Better Homes (IRLBH) is described with the goal of validating the nonlinear finite element modelling of a residential gable roof. The results were validated for uplift wind pressure that causes permanent RTWC withdrawal. The next chapter introduces a new solution model that simulates the whole gable roof as a beam on an elastic foundation. This solution model can perform the analysis either linearly or nonlinearly with respect to RTWC stiffness. To assess the performance of the solution model, the finite element modelling and the experimental results were compared. Chapter 4 provides an analysis of the gable roof with respect to the random stiffness of each RTWC through the use of Monte Carlo simulations for evaluating the probability of roof failure. Chapter 5 employs the previously proposed external retrofitting system designed to mitigate the failure of house roofs in which toe-nails have been employed as RTWCs. Chapter 5 also describes the extension of the solution model discussed in Chapter 3 so that it incorporates analysis involving the retrofitting system.

6.2 Conclusions

Analysis of the gable roof using nonlinear finite element modelling revealed the ability of the numerical model to predict the experimental RTWC deflection. Based on the comparison between the numerical prediction and the experimental results, the following conclusions can be drawn:

- Good agreement is achieved between the numerical model and the experimental results in terms of evaluating permanent RTWC withdrawal deflection under the pressure associated with wind speeds of 30 m/sec to 40 m/sec. With reference to the

mean numerical values, the mean percentage difference reaches 20.7 % at 40 m/sec. The numerical model, however, tends to overestimate the experimental results at the failure wind speed of 45 m/sec, especially for the south side of the roof. This discrepancy occurs due to the variations in both the stiffness and capacity of actual toe-nail connections, while in contrast, the analysis is performed with identical load-deflection relations for all RTWCs.

- Analysis performed using the tributary area method under the code pressure produces underestimates of the load shares of the end gable trusses. The load sharing of both end gable trusses calculated using the tributary area method under the code pressure is 14 %, while finite element modelling produces a 29 % load share under code pressure. The tributary area method does not include consideration of either the stiffness of the trusses or the effects of pressures away from the trusses, while finite element modelling does.

- A zero slope of the curve representing the load sharing between adjacent trusses is an indication that all RTWCs that support these trusses have reached their ultimate capacity. At the failure speed of 45 m/sec, for example, trusses T2 to T8 reach their maximum RTWC capacity at zero slopes on the load sharing curve.

The semi-analytical solution model was used for determining the distribution of the uplift wind loads on the supporting trusses. This new model simulates an entire roof truss as a beam on an elastic foundation through the use of statically indeterminate slope deflection equations that include shear deformation. Analysis using this approach offers the advantage of shorter run times than 3D finite element modelling. The following conclusions can be drawn:

- In regard to evaluating the reaction of RTWC S3 through the time history, good agreement is indicated between the two analysis tools, resulting in a mean percentage difference of 9 % at wind speeds of 35 m/sec. RTWC S3 is selected because it exhibited the greatest deflection measurements. The percentage difference for the RTWC S3 reaction increases to 31 % at wind speeds of 45 m/sec. The difference increases with greater wind speed, due to the approximation of solution model analysis.

- A comparison of the experimental results and the solution model predictions with respect to the deflection of all RTWCs at wind speeds ranging from 30 m/sec to 45 m/sec shows good agreement except at the south side of the roof for wind speeds of 40 m/sec and 45 m/sec due to the use of a similar load-deflection curve for all RTWCs, which in reality vary, especially for toe-nailed connections. With respect to the north side connections at higher speeds, the average percentages of differences are 17 % and 14 % for wind speeds of 40 m/sec and 45 m/sec, respectively.

- A comparison of the load sharing computed using the finite element model and the solution model at the maximum realistic uplift load from a 35 m/sec wind speed reveals a good match, with a difference of only 0.43 %.

The probability of roof failure based on the randomness of RTWC behaviour was studied through a reliability assessment. Monte Carlo simulations were employed for estimating the reliability of the roof truss system through the use of appropriate probabilistic models for the RTWCs and the uplift wind loads. The solution model used for these simulations was the simplified solution discussed in Chapter 3. Based on a series of simulations, the following conclusions can be drawn:

- The first set of Monte Carlo simulations uses the deterministic uplift pressure coefficients and random RTWC. The results indicate that the mean failure wind speed ranges from 26 m/sec to 38 m/sec. The histogram plotted for this range and fitted to a normal distribution has a mean of 31 m/sec and a coefficient of variation of 0.063. A number of the speeds in this range were reanalyzed in order to establish the fragility curve.

- In the second set of Monte Carlo simulations, two random variables are considered: the randomness of the RTWC load-deflection curves and the uplift wind pressure. Failure speeds are evaluated, with the mean wind speed ranging from 26 m/sec up to 46 m/sec. The histogram plotted for this range and fitted to a normal distribution has a mean of 35 m/sec and a coefficient of variation of 0.082. For each of the speeds in this range, an estimate of the probability of failure is obtained from the analysis of 10,000 scenarios. The findings reveal that the probability of roof failure evaluated according to deterministic pressure coefficients is greater than that produced using the random

pressure coefficients. Above a mean wind speed of 30 m/sec, the probability of roof failure increases rapidly.

Based on these conclusions, the wind speed at which a roof fails is random, and the probability of roof failure is amplified above a wind speed of 30 m/sec. This thesis analyzes the proposed external retrofitting system designed to address this challenge. The external retrofitting consists of bearing cables, external cables, and rigid bars. The bearing cables are installed on the roof and attached to rigid bars at the roof edge. The rigid bars are connected to external cables that are supported by micropiles permanently embedded in the ground. The external cables are pretensioned using turnbuckles. The simplified solution model was extended to include analysis of the retrofitting system, and its results were validated against the structural laboratory and WindEEE experimental findings.

- The solution model and the finite element model results were compared with respect to their analysis of the retrofitting prototype used in the WindEEE experiment. A good match can be observed, especially for RTWC deflection; however, in terms of evaluating the external cable tension, the solution model underestimates the tension determined using FEM. The mean difference in the cable tension results produced by the two analysis methods is 4.7 % with respect to the finite element modelling.

- The solution model results have been validated against the structural laboratory and the WindEEE experimental findings. In general, the predicted RTWC deflection represents a good match with the experimental results in terms of values and trends. On the other hand, the tension predicted in the external cables does not agree with the experimental values due to the approximation in the analysis. In the numerical model prediction, when the connections have separated from the walls, the tension in the external cables initially remains at the level of the pretension forces, following which, the tension in the cables increases rapidly with increases in the total uplift load.

- The WindEEE prototype distributes the uplift wind loads according to a load sharing of 80 % and 20 % for the RTWCs and the retrofitting system, respectively. Following RTWC failure at a wind speed of 40 m/sec, the load sharing percentage for the retrofit system increases rapidly as the RTWC load share decreases.

- The retrofitting system elevates by 36.4 % the wind speed at which possible failure occurs; however, after the connections have failed, the retrofitting system also creates an additional load path and helps keep the roof attached to the house after the end of the wind storm.

6.3 Recommendations for Future Work

The following investigations are recommended for future work, which will extend the results of the work reported in this thesis:

- Perform a parametric study of the retrofitting system, including the use of the solution model.
- Investigate wall stability following RTWC failure.
- Improve the capacity of the fascia and overhang members by applying brackets in order to prevent failure of these members as a result of the pretension forces at the external cables.
- Investigate the use of a wire net or bearing cables for extending the retrofitting system to include a variety of types of roof systems such as hip roofs, shed roofs, or a mixture of roofs.
- Extend the simplified solution model to incorporate analysis of these additional types of roofs, such as hip roofs.
- Perform a reliability assessment of retrofitted light-frame wood houses.

A. APPENDIX A: Cable Element Example

For this example, as shown in Figure A.1(a), a simply supported cable is pretensioned with $P_0 = 2$ kN to provide initial tightening of the system. The tension and deformation must be calculated for the cable shown, under a distributed load of 1 kN/m running perpendicular to the cable. The axial rigidity of this cable was selected to be 8500 kN.
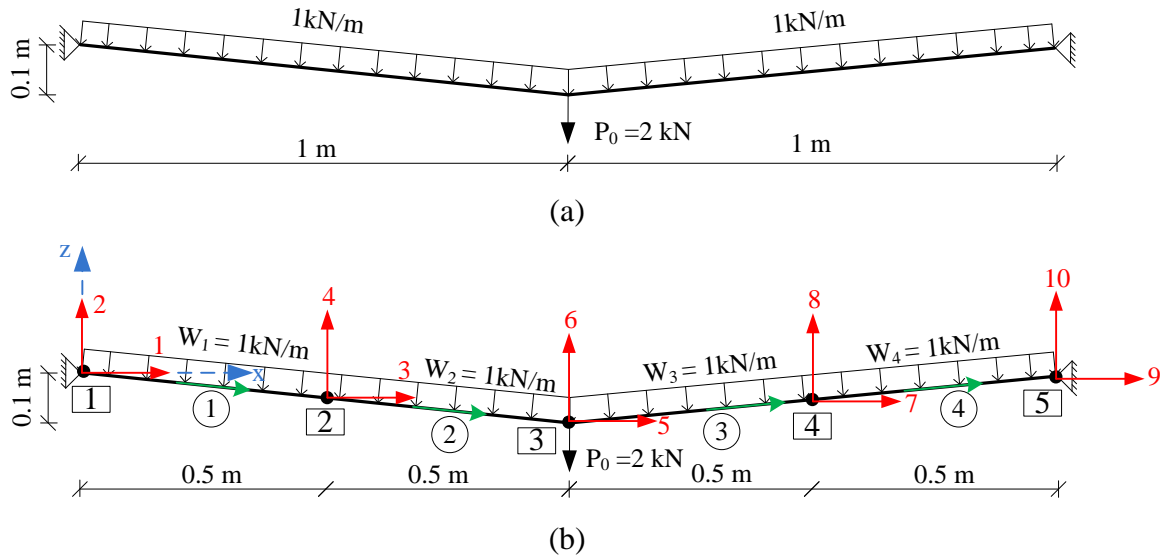
Figure A.1: Numerical example of a cable element: (a) simply supported cable under distributed load; (b) discretization of the numerical example.

The first step in analyzing this cable is to divide it into a number of elements. Four elements are thus chosen for this cable, as shown in Figure A.1 (b). With these four elements, the degrees of freedom are ten with eight active degrees of freedom (3 to 8). The vertical force P_0 is resolved within the direction of the cable elements in order to assess the pretension force due to the initial cable tightening, which is found to be $F_i = 10.05$ kN. The coordinates of the cable nodes for the initial condition are evaluated as $x_1 = 0$, $x_2 = 0.5$, $x_3 = 1$, $x_4 = 1.5$, $x_5 = 2$, $z_1 = 0$, $z_2 = -0.05$, $z_3 = -0.1$, $z_4 = -0.05$, $z_5 = 0$. With these coordinates and with $F = F_i$, the global stiffness matrices of the four cables can be calculated by substituting their values into Equation (5.8). After the boundary conditions have been applied, the assembled global stiffness matrix can then be evaluated as follows:

$$
K = \begin{matrix}
3 & 4 & 5 & 6 & 7 & 8 \\
\begin{bmatrix}
33496.7 & -3345.7 & -16748.3 & 1672.8 & 0 & 0 \\
-3345.7 & 374.6 & 1672.8 & -187.3 & 0 & 0 \\
-16748.3 & 1672.8 & 33496.7 & 0 & -16748.3 & -1672.8 \\
1672.8 & -187.3 & 0 & 374.6 & -1672.8 & -187.3 \\
0 & 0 & -16748.3 & -1672.8 & 33496.7 & 3345.7 \\
0 & 0 & -1672.8 & -187.3 & 3345.7 & 374.6
\end{bmatrix}
& \begin{matrix} 3 \\ 4 \\ 5 \\ 6 \\ 7 \\ 8_{kN/m} \end{matrix}
\end{matrix}
\tag{A.1}
$$

After the boundary conditions have been applied, the load vector can be written as:

$$
P = \begin{bmatrix}
W_1 \times L_{01}/2 \times \lambda_{z1} + W_2 \times L_{02}/2 \times \lambda_{z2} \\
-W_1 \times L_{01}/2 \times \lambda_{x1} - W_2 \times L_{02}/2 \times \lambda_{x2} \\
W_2 \times L_{02}/2 \times \lambda_{z2} + W_3 \times L_{03}/2 \times \lambda_{z3} \\
-W_2 \times L_{02}/2 \times \lambda_{x2} - W_3 \times L_{03}/2 \times \lambda_{x3} \\
W_3 \times L_{03}/2 \times \lambda_{z3} + W_4 \times L_{04}/2 \times \lambda_{z4} \\
-W_3 \times L_{03}/2 \times \lambda_{x3} - W_4 \times L_{04}/2 \times \lambda_{x4}
\end{bmatrix}
\begin{matrix} 3 \\ 4 \\ 5 \\ 6 \\ 7 \\ 8 \end{matrix}
=
\begin{bmatrix}
-0.05 \\
-0.5 \\
0 \\
-0.5 \\
0.05 \\
-0.5
\end{bmatrix}
\begin{matrix} 3 \\ 4 \\ 5 \\ 6 \\ 7 \\ 8_{kN} \end{matrix}
\tag{A.2}
$$

By substitution in Equation (5.9), the nodal displacements at the initial analysis can be obtained as follows:

$$
d = \begin{bmatrix}
-0.00125 \\
-0.01517 \\
-4.30\text{E}-20 \\
-0.00534 \\
-0.00125 \\
-0.01517
\end{bmatrix}
\begin{matrix} 3 \\ 4 \\ 5 \\ 6 \\ 7 \\ 8_m \end{matrix}
\tag{A.3}
$$

During the first iteration, new cable coordinates and new tension forces are calculated for each cable element in order to recalculate a new stiffness matrix K_n:

$$
\begin{aligned}
x_{n2} &= x_2 + d(1) = 0.5 - 0.00125 = 0.49875\,\text{m} \\
z_{n2} &= z_2 + d(2) = -0.05 - 0.01517 = -0.06517\,\text{m} \\
x_{n3} &= x_3 + d(3) = 1.0 + 0 = 1.0\,\text{m} \\
z_{n3} &= z_3 + d(4) = -0.1 - 0.00534 = -0.10534\,\text{m} \\
x_{n4} &= x_4 + d(5) = 1.5 + 0.00125 = 1.50125\,\text{m} \\
z_{n4} &= z_4 + d(6) = -0.05 - 0.01517 = -0.06517\,\text{m}
\end{aligned}
\tag{A.4}
$$

$$L_1 = \sqrt{(x_{n2} - x_1)^2 + (z_{n2} - z_1)^2} = 0.50299\,\text{m}$$

$$L_2 = \sqrt{(x_{n3} - x_{n2})^2 + (z_{n3} - z_{n2})^2} = 0.50286\,\text{m}$$

$$L_3 = \sqrt{(x_{n4} - x_{n3})^2 + (z_{n4} - z_{n3})^2} = 0.50286\,\text{m}$$

$$L_4 = \sqrt{(x_5 - x_{n4})^2 + (z_5 - z_{n4})^2} = 0.50299\,\text{m}$$

(A.5)

$$F_1 = F_{i1} + EA\frac{L_1 - L_{01}}{L_{01}} = 10.05 + 8500\frac{0.50299 - 0.5025}{0.5025} = 18.33\,\text{kN}$$

$$F_2 = F_{i2} + EA\frac{L_2 - L_{02}}{L_{02}} = 10.05 + 8500\frac{0.50286 - 0.5025}{0.5025} = 16.13\,\text{kN}$$

$$F_3 = F_{i3} + EA\frac{L_3 - L_{03}}{L_{03}} = 10.05 + 8500\frac{0.50286 - 0.5025}{0.5025} = 16.13\,\text{kN}$$

$$F_4 = F_{i4} + EA\frac{L_4 - L_{04}}{L_{04}} = 10.05 + 8500\frac{0.50299 - 0.5025}{0.5025} = 18.33\,\text{kN}$$

(A.6)

After the direction cosines λ_x and λ_z have been determined based on the new node coordinates, the new assembled global stiffness matrix can then be evaluated following the application of the boundary conditions, as follows:

$$K_n = \begin{array}{c} \\ \\ \\ \\ \\ \\ \end{array}\begin{array}{cccccc} {\scriptstyle 3} & {\scriptstyle 4} & {\scriptstyle 5} & {\scriptstyle 6} & {\scriptstyle 7} & {\scriptstyle 8} \end{array}$$

$$K_n = \begin{bmatrix} 33440.2 & -3512.9 & -16807.9 & 1344.4 & 0 & 0 \\ -3512.9 & 459.9 & 1344.4 & -139.9 & 0 & 0 \\ -16807.9 & 1344.4 & 33615.8 & 0 & -16807.9 & -1344.4 \\ 1344.4 & -139.9 & 0 & 279.9 & -1344.4 & -139.9 \\ 0 & 0 & -16807.9 & -1344.4 & 33440.2 & 3512.9 \\ 0 & 0 & -1344.4 & -139.9 & 3512.9 & 459.9 \end{bmatrix}\begin{array}{c} 3 \\ 4 \\ 5 \\ 6 \\ 7 \\ 8 \end{array}_{kN/m}$$

(A.7)

Once the boundary conditions have been applied, the out-of-equilibrium forces in two directions ΔP can be estimated, as shown in Figure A.2, which can be expressed as follows:
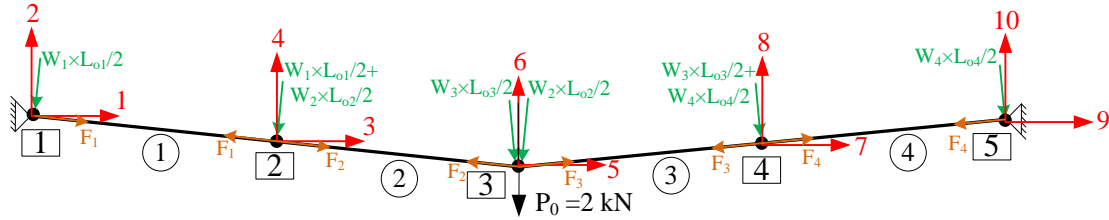
Figure A.2: Out-of-equilibrium forces at each node of the numerical example of a cable element.

$$\Delta P = \begin{bmatrix} -F_1 \times \lambda_{x1} + F_2 \times \lambda_{x2} \\ -F_1 \times \lambda_{z1} + F_2 \times \lambda_{z2} \\ -F_2 \times \lambda_{x2} + F_3 \times \lambda_{x3} \\ -F_2 \times \lambda_{z2} + F_3 \times \lambda_{z3} - 2 \\ -F_3 \times \lambda_{x3} + F_4 \times \lambda_{x4} \\ -F_3 \times \lambda_{z3} + F_4 \times \lambda_{z4} \end{bmatrix}\begin{matrix}3\\4\\5\\6\\7\\8\end{matrix} + \begin{bmatrix} W_1 \times L_{01}/2 \times \lambda_{z1} + W_2 \times L_{02}/2 \times \lambda_{z2} \\ -W_1 \times L_{01}/2 \times \lambda_{x1} - W_2 \times L_{02}/2 \times \lambda_{x2} \\ W_2 \times L_{02}/2 \times \lambda_{z2} + W_3 \times L_{03}/2 \times \lambda_{z3} \\ -W_2 \times L_{02}/2 \times \lambda_{x2} - W_3 \times L_{03}/2 \times \lambda_{x3} \\ W_3 \times L_{03}/2 \times \lambda_{z3} + W_4 \times L_{04}/2 \times \lambda_{z4} \\ -W_3 \times L_{03}/2 \times \lambda_{x3} - W_4 \times L_{04}/2 \times \lambda_{x4} \end{bmatrix}\begin{matrix}3\\4\\5\\6\\7\\8\end{matrix} = \begin{bmatrix} -2.19 \\ 0.6 \\ 0 \\ 0.09 \\ 2.19 \\ 0.6 \end{bmatrix}\begin{matrix}3\\4\\5\\6\\7\\8_{kN}\end{matrix} \quad (A.8)$$

$$\Delta d = K_n^{-1} \times \Delta P = \begin{bmatrix} 0.0002950 \\ 0.0039959 \\ 0 \\ 0.0014739 \\ -0.0002950 \\ 0.0039959 \end{bmatrix}\begin{matrix}3\\4\\5\\6\\7\\8_m\end{matrix} \quad (A.9)$$

$$d = \begin{bmatrix} -0.00125 \\ -0.01517 \\ -4.30E-20 \\ -0.00534 \\ -0.00125 \\ -0.01517 \end{bmatrix}\begin{matrix}3\\4\\5\\6\\7\\8_m\end{matrix} + \begin{bmatrix} 0.0002950 \\ 0.0039959 \\ 0 \\ 0.0014739 \\ -0.0002950 \\ 0.0039959 \end{bmatrix}\begin{matrix}3\\4\\5\\6\\7\\8_m\end{matrix} = \begin{bmatrix} -0.00095 \\ -0.01117 \\ -1.98E-18 \\ -0.00387 \\ 0.000955 \\ -0.01117 \end{bmatrix}\begin{matrix}3\\4\\5\\6\\7\\8_m\end{matrix} \quad (A.10)$$

Tables A.1 and A.2 summarize the output from the remaining iterations in terms of cable tension and node deflection, respectively. It is clear from these tables that the cable tension reaches convergence at the fifth iteration since no change occurs in the cable tension between the fourth and fifth iterations.

Table A.1: Cable element tension forces at each iteration

Tension force	Iteration 2	Iteration 3	Iteration 4	Iteration 5
F1 (kN)	14.89	14.54	14.53	14.53
F2 (kN)	14.73	14.54	14.53	14.53
F3 (kN)	14.73	14.54	14.53	14.53
F4 (kN)	14.89	14.54	14.53	14.53

Table A.2: Cable element nodal deflection at each iteration

Node deflection	Iteration 2	Iteration 3	Iteration 4	Iteration 5
d3 (mm)	-0.90	-0.90	-0.90	-0.90
d4 (mm)	-10.53	-10.52	-10.52	-10.52
d5 (mm)	0.00	0.00	0.00	0.00
d6 (mm)	-3.76	-3.75	-3.75	-3.75
d7 (mm)	0.90	0.90	0.90	0.90
d8 (mm)	-10.53	-10.52	-10.52	-10.52

B. APPENDIX B: A Segment Example

For this example, a simply supported truss is retrofitted with a bearing cable. The initial pretension force at the bearing cable is 0.2 kN. The axial rigidity of the cable element is chosen to be 5654 kN. The axial rigidity and flexural rigidity of the frame element are selected as 64,000 kN and 8.533 kN.m^2, respectively. The tension in the cable and the deformation of the segment shown in the figure must be calculated for a distributed load of 0.5 kN/m running perpendicular to the segment.
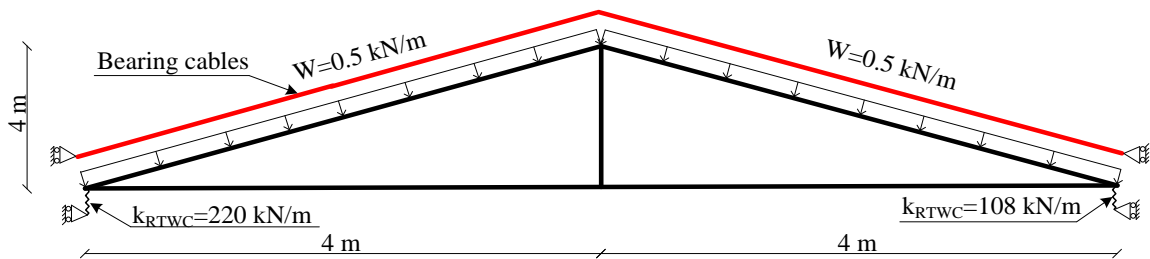
Figure B.1: Numerical example of an A segment.

Figure B.2 illustrates the degrees of freedom assigned to each frame and cable element. There are total of 23 degrees of freedom, with four of them being non-active (1, 13, 19, 23). Each cable element has two degrees of freedom per node, while the frame elements have three degrees of freedom per node. As shown in Figure B.2, and to assign the constraint action between the frame and cable elements, the vertical degrees of freedom at the intersections (2, 5, 8, 11, 14) are set to be similar. The bearing cable is attached to the top truss chord; however, this bearing cable is modelled numerically with an approximately 10 cm offset from the top chord. To simplify the analysis, the bearing cable is divided into four elements; however, to increase accuracy, it should be divided into a greater number of elements. Based on the dimensions shown in Figure B.1, the coordinates are summarized in Table B.1.

Table B.1: Coordinates of a sample A segment

Nodes	1	2	3	4	5	6	7	8	9	10	11
x (m)	0	2	4	6	8	4	-0.0246	1.97575	4	6.0243	8.024
z (m)	0	0.5	1	0.5	0	0	0.09701	0.59701	1.1	0.597	0.097
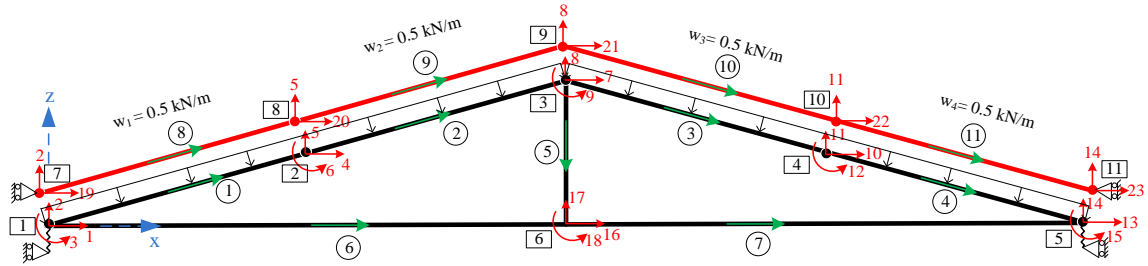
Figure B.2: Discretization of the numerical example.

After defining the A segments coordinates, the global stiffness matrix K is evaluated for all A segments in the order of 19 × 19. After the application of the boundary condition, the load vector is written as in Equation (B.1). This load vector is used with the assembly global stiffness matrix K in order to calculate the initial displacement of the numerical example, as shown in Equation (B.2):

$$
P = \begin{bmatrix}
w_1 \times L_1 / 2 \times \lambda_{x1} \\
w_1 \times L_1^2 / 12 \\
-w_1 \times L_1 / 2 \times \lambda_{y1} - w_2 \times L_2 / 2 \times \lambda_{y2} \\
w_1 \times L_1 / 2 \times \lambda_{x1} + w_2 \times L_2 / 2 \times \lambda_{x2} \\
-w_1 \times L_1^2 / 12 + w_2 \times L_2^2 / 12 \\
-w_2 \times L_2 / 2 \times \lambda_{y2} - w_3 \times L_3 / 2 \times \lambda_{y3} \\
w_2 \times L_2 / 2 \times \lambda_{x2} + w_3 \times L_3 / 2 \times \lambda_{x3} \\
-w_2 \times L_2^2 / 12 + w_3 \times L_3^2 / 12 \\
-w_3 \times L_3 / 2 \times \lambda_{y3} - w_4 \times L_4 / 2 \times \lambda_{y4} \\
w_3 \times L_3 / 2 \times \lambda_{x3} + w_4 \times L_4 / 2 \times \lambda_{x4} \\
-w_3 \times L_3^2 / 12 + w_4 \times L_4^2 / 12 \\
w_4 \times L_4 / 2 \times \lambda_{x4} \\
-w_4 \times L_4^2 / 12 \\
0 \\
0 \\
0 \\
0 \\
0 \\
0
\end{bmatrix}
\begin{matrix}
2 \\ 3 \\ 4 \\ 5 \\ 6 \\ 7 \\ 8 \\ 9 \\ 10 \\ 11 = \\ 12 \\ 14 \\ 15 \\ 16 \\ 17 \\ 18 \\ 20 \\ 21 \\ 22
\end{matrix}
\begin{bmatrix}
0.5 \\
0.17708 \\
-0.25 \\
1 \\
0 \\
0 \\
1 \\
0 \\
0.25 \\
1 \\
0 \\
0.5 \\
-0.17708 \\
0 \\
0 \\
0 \\
0 \\
0 \\
0
\end{bmatrix}
\begin{matrix}
2 \\ 3 \\ 4 \\ 5 \\ 6 \\ 7 \\ 8 \\ 9 \\ 10 \\ 11 \\ 12 \\ 14 \\ 15 \\ 16 \\ 17 \\ 18 \\ 20 \\ 21 \\ 22_{kN}
\end{matrix}
$$

(B.1)

$$
d = K^{-1} \times P = \begin{bmatrix}
0.009092 \\
0.043353 \\
-0.01642 \\
0.07538 \\
-0.00893 \\
-0.00118 \\
0.015037 \\
0.001178 \\
0.01524 \\
0.080093 \\
0.011287 \\
0.018516 \\
-0.041 \\
0 \\
0.015041 \\
0.001178 \\
-0.01637 \\
-0.00117 \\
0.015193
\end{bmatrix}
\begin{matrix}
2 \\
3 \\
4 \\
5 \\
6 \\
7 \\
8 \\
9 \\
10 \\
11 \\
12 \\
14 \\
15 \\
16 \\
17 \\
18 \\
20 \\
21 \\
22_m
\end{matrix}
\tag{B.2}
$$

The Equation (5.16) is used to evaluate the tension force in each cable element as listed in Table B.2. The numerical example depicted in Figure B.2 has seven frame elements, each of which must be evaluated with respect to its global internal forces as follows:

$$
Load_1 = \begin{bmatrix}
0 \\
w_1 \times \dfrac{L_1}{2} \\
w_1 \times \dfrac{L_1^2}{12} \\
0 \\
w_1 \times \dfrac{L_1}{2} \\
-w_1 \times \dfrac{L_1^2}{12}
\end{bmatrix}
\; \& \; Load_2 = \begin{bmatrix}
0 \\
w_2 \times \dfrac{L_2}{2} \\
w_2 \times \dfrac{L_2^2}{12} \\
0 \\
w_2 \times \dfrac{L_2}{2} \\
-w_2 \times \dfrac{L_2^2}{12}
\end{bmatrix}
\; \& \; Load_3 = \begin{bmatrix}
0 \\
w_3 \times \dfrac{L_3}{2} \\
w_3 \times \dfrac{L_3^2}{12} \\
0 \\
w_3 \times \dfrac{L_3}{2} \\
-w_3 \times \dfrac{L_3^2}{12}
\end{bmatrix}
\; \& \; Load_4 = \begin{bmatrix}
0 \\
w_4 \times \dfrac{L_4}{2} \\
w_4 \times \dfrac{L_4^2}{12} \\
0 \\
w_4 \times \dfrac{L_4}{2} \\
-w_4 \times \dfrac{L_4^2}{12}
\end{bmatrix}
\tag{B.3}
$$

$$
Load_5 = Load_6 = Load_7 = \begin{bmatrix}
0 \\
0 \\
0 \\
0 \\
0 \\
0
\end{bmatrix}
\tag{B.4}
$$

dr is the nodal displacement for all A segments in global directions, including non-active degrees of freedom as zeros:

$$
dr = \begin{bmatrix} 0 \\ d(1:11) \\ 0 \\ d(12:16) \\ 0 \\ d(17:19) \\ 0 \end{bmatrix} \& v_1 = \begin{bmatrix} dr(1) \\ dr(2) \\ dr(3) \\ dr(4) \\ dr(5) \\ dr(6) \end{bmatrix} \& v_2 = \begin{bmatrix} dr(4) \\ dr(5) \\ dr(6) \\ dr(7) \\ dr(8) \\ dr(9) \end{bmatrix} \& v_3 = \begin{bmatrix} dr(7) \\ dr(8) \\ dr(9) \\ dr(10) \\ dr(11) \\ dr(12) \end{bmatrix}
\tag{B.5}
$$

$$
v_4 = \begin{bmatrix} dr(10) \\ dr(11) \\ dr(12) \\ dr(13) \\ dr(14) \\ dr(15) \end{bmatrix} \& v_5 = \begin{bmatrix} dr(7) \\ dr(8) \\ dr(9) \\ dr(16) \\ dr(17) \\ dr(18) \end{bmatrix} \& v_6 = \begin{bmatrix} dr(1) \\ dr(2) \\ dr(3) \\ dr(16) \\ dr(17) \\ dr(18) \end{bmatrix} \& v_7 = \begin{bmatrix} dr(16) \\ dr(17) \\ dr(18) \\ dr(13) \\ dr(14) \\ dr(15) \end{bmatrix}
\tag{B.6}
$$

$$
u_i = T_i \times v_i
\tag{B.7}
$$

$$
Q_i = k_i \times u_i - Load_i
\tag{B.8}
$$

$$
Fm_i = T_i^T \times Q_i
\tag{B.9}
$$

where $i = 1, 2, ..., 7$;

The out-of-equilibrium forces vector ΔP (Equation B.14) is evaluated with the use of the tension force in the cable elements F_j and the internal forces acting on the frame elements Fm_i as well as the RTWC reaction, which is calculated by multiplying the deflection by the spring constant, as follows:

$$
RL = K_{RTWC} \times dr(2) = 220 \times dr(2)
\tag{B.10}
$$

$$
RR = K_{RTWC} \times dr(14) = 108 \times dr(14)
\tag{B.11}
$$

The out-of-equilibrium forces vector ΔP is used with the revised stiffness matrix Kn in order to evaluate the incremental displacement Δd. Tables B.2 and B.3 summarize the output of the iterations in terms of cable tension and nodal displacement, respectively. It

is clear from these tables that this example reaches convergence at the fourth iteration because no change occurs in the output between the third and fourth iterations. The RTWC reaction is calculated as follows:

$$RL = K_{RTWC} \times dr(2) = 220 \times 0.008885 = 1.945 \text{ kN} \tag{B.12}$$

$$RR = K_{RTWC} \times dr(14) = 108 \times 0.018041 = 1.948 \text{ kN} \tag{B.13}$$

$$
\Delta P =
\begin{bmatrix}
F_8 \times \lambda_{z9} & 2 \\
0 & 3 \\
0 & 4 \\
F_9 \times \lambda_{z9} - F_8 \times \lambda_{z8} & 5 \\
0 & 6 \\
0 & 7 \\
F_{10} \times \lambda_{z10} - F_9 \times \lambda_{z9} - 0.485 \times F_i & 8 \\
0 & 9 \\
0 & 10 \\
F_{11} \times \lambda_{z11} - F_{10} \times \lambda_{z10} & 11 \\
0 & 12 \\
-F_{11} \times \lambda_{z11} & 14 \\
0 & 15 \\
0 & 16 \\
0 & 17 \\
0 & 18 \\
F_9 \times \lambda_{x9} - F_8 \times \lambda_{x8} & 20 \\
F_{10} \times \lambda_{x10} - F_9 \times \lambda_{xz9} & 21 \\
F_{11} \times \lambda_{x11} - F_{10} \times \lambda_{x10} & 22
\end{bmatrix}
-
\begin{bmatrix}
Fm_1(2) + Fm_6(2) + RL & 2 \\
Fm_1(3) + Fm_6(3) & 3 \\
Fm_1(4) + Fm_2(1) & 4 \\
Fm_1(5) + Fm_2(2) & 5 \\
Fm_1(6) + Fm_2(3) & 6 \\
Fm_3(1) + Fm_2(4) + Fm_5(1) & 7 \\
Fm_3(2) + Fm_2(5) + Fm_5(2) & 8 \\
Fm_3(3) + Fm_2(6) + Fm_5(3) & 9 \\
Fm_3(4) + Fm_4(1) & 10 \\
Fm_3(5) + Fm_4(2) & 11 \\
Fm_3(6) + Fm_4(3) & 12 \\
Fm_4(5) + Fm_7(5) + RR & 14 \\
Fm_4(6) + Fm_7(6) & 15 \\
Fm_6(4) + Fm_5(4) + Fm_7(1) & 16 \\
Fm_6(5) + Fm_5(5) + Fm_7(2) & 17 \\
Fm_6(6) + Fm_5(6) + Fm_7(3) & 18 \\
0 & 20 \\
0 & 21 \\
0 & 22
\end{bmatrix}
\tag{B.14}
$$

Table B.2: Cable element tension forces at each iteration

Tension force	Iteration 1	Iteration 2	Iteration 3	Iteration 4
F8 (kN)	3.83	2.70	2.67	2.67
F9 (kN)	3.24	2.66	2.63	2.63
F10 (kN)	3.65	2.66	2.63	2.63
F11 (kN)	3.41	2.70	2.67	2.67

Table B.3: Nodal displacement at each iteration

Node deflection	Iteration 1	Iteration 2	Iteration 3	Iteration 4
d2(m)	0.0089	0.0089	0.0089	0.0089
d3(rad)	0.0391	0.0389	0.0389	0.0389
d4(m)	-0.0145	-0.0144	-0.0144	-0.0144
d5(m)	0.0673	0.0669	0.0669	0.0669
d6(rad)	-0.0081	-0.0081	-0.0081	-0.0081
d7(m)	-0.0011	-0.0011	-0.0011	-0.0011
d8(m)	0.0141	0.0141	0.0141	0.0141
d9(rad)	0.0011	0.0011	0.0011	0.0011
d10(m)	0.0134	0.0133	0.0133	0.0133
d11(m)	0.0718	0.0715	0.0715	0.0715
d12(rad)	0.0104	0.0104	0.0104	0.0104
d14(m)	0.0180	0.0180	0.0180	0.0180
d15(rad)	-0.0368	-0.0366	-0.0366	-0.0366
d16(m)	0.0000	0.0000	0.0000	0.0000
d17(m)	0.0141	0.0141	0.0141	0.0141
d18(rad)	0.0011	0.0011	0.0011	0.0011
d20(m)	-0.0146	-0.0145	-0.0145	-0.0145
d21(m)	-0.0011	-0.0011	-0.0011	-0.0011
d22(m)	0.0133	0.0132	0.0132	0.0132

Curriculum Vitae

Name:	Adnan Enajar
Post-secondary Education and Degrees:	Bachelor of Civil Engineering, 1998-2003 Department of Civil and Environmental Engineering Faculty of Engineering Tripoli University (Former; Al-Fateh University) Tripoli, Libya
	Master of Science, 2005-2007 Department of Civil and Environmental Engineering Faculty of Engineering Tripoli University (Former; Al-Fateh University) Tripoli, Libya
	Doctor of Philosophy, 2014-2019 Department of Civil and Environmental Engineering Faculty of Engineering University of Western Ontario London, Ontario, Canada
Honours and Awards:	Post Graduate External Scholarship, The Libyan Authority of Higher Education. Libya, 2014-2019
Related Work Experience	Structural engineer 2004 – 2005 Libyan Arab Domestic Investment Company (LADICO) Teaching Assistant, 2004-2007 Department of Civil and Environmental Engineering Faculty of Engineering Tripoli University Tripoli, Libya (Former; Al-Fateh University) Structural engineer 2007 – 2008 Bonyan Consulting Engineers Assistant lecturer, 2008-2013 Department of Civil and Environmental Engineering Faculty of Engineering Tripoli University Tripoli, Libya (Former; Al-Fateh University) Teaching Assistant, 2014-2018 Department of Civil and Environmental Engineering Faculty of Engineering University of Western Ontario London, Ontario, Canada

Publications:

Enajar, A.F., Jacklin, R.B., El Damatty, A.A. (2019), "Nonlinear Modeling of Roof to Wall Connections in a Gable-Roof Structure under Uplift Wind Loads", *Wind and Structures*, **28**(3),181-190.

Rosenkrantz, J. D., Enajar, A., Jacklin, R., and El Damatty, A. (2016), "Structural modelling and verification methods to develop a cable roof harness retrofit", *Resilient Infrastructure*, London, ON, June.

El Damatty, A.A., Shehata, A., Enajar, A., Rosenkrantz, J., and Elezaby, F. (2018), "Research for adaptive and sustainable structures", *8th International Conference on Environmental Effects on Buildings and People*, Cracow, Poland, October.

Enajar, A., El Damatty, A.A., and Nassef, A. (2019), "Closed-Form Solution and Reliability Analysis for Light-Frame Wood-Houses under Uplift Wind Loads", *Submitted to the 15th International Conference on Wind Engineering*, Beijing, China; September 1-6, 2019.